Few-cycle broadband mid-IR pulse generation via optical parametric down-conversion

Liu, Kun

2020

FEW-CYCLE BROADBAND MID-IR PULSE GENERATION VIA OPTICAL PARAMETRIC DOWN-CONVERSION

LIU KUN

SCHOOL OF ELECTRICAL AND ELECTRONIC ENGINEERING

2020

FEW-CYCLE BROADBAND MID-IR PULSE GENERATION VIA OPTICAL PARAMETRIC DOWN-CONVERSION

By

Liu Kun

School of Electrical and Electronics Engineering

A thesis submitted to the Nanyang Technological University in partial fulfilment of the requirement for the degree of Doctor of Philosophy

2020

Statement of Originality

I hereby certify that the work embodied in this thesis is the result of original research, is free of plagiarised materials, and has not been submitted for a higher degree to any other University or Institution.

16/07/2020
· · · · · · · · · · · · · · · · ·
Date

· ·
Liu Kun

Supervisor Declaration Statement

I have reviewed the content and presentation style of this thesis and declare it is free of plagiarism and of sufficient grammatical clarity to be examined. To the best of my knowledge, the research and writing are those of the candidate except as acknowledged in the Author Attribution Statement. I confirm that the investigations were conducted in accord with the ethics policies and integrity standards of Nanyang Technological University and that the research data are presented honestly and without prejudice.

16/07/2020

. . . .

Date   Prof. Wang Qijie

Authorship Attribution Statement

This thesis mainly contains material from 4 papers listing me as an author, published in the following peer-reviewed journals.

1. X. Zou, W. Li, H. Liang, K. Liu, S. Qu, Q. J. Wang and Y. Zhang, "300 μJ, 3 W, few-cycle, 3 μm OPCPA based on periodically poled stoichiometric lithium tantalate crystals," Optics Letter 44(11), 2791-2794 (2019). The content of this paper is presented in Chapter 3.

   Author contributions:
   H. Liang conceived and designed the experiment. K. Liu and S. Qu made contribution to the early-phase experimental design and developed the seed of the OPCPA system. X. Zou did the OPCPA experiment with the help from W. Li, H. Liang, K. Liu and S. Qu in experimental optimizations, pulse characterization, nonlinear pulse compression and high-harmonic generation. W. Li did the CEP stability measurement. Q. J. Wang, H. Liang and Y. Zhang provided the essential infrastructure for the experiment. X. Zou prepared the manuscript. H. Liang and Q. J. Wang reviewed the manuscript. All authors discussed the results and contributed to the manuscript.

2. K. Liu, H. Liang, W. Li, X. Zou, S. Qu, T. Lang, Y. Zhang and Q. J. Wang, "Microjoule Sub-Two-Cycle Mid-Infrared Intrapulse-DFG Driven by 3-μm OPCPA," IEEE Photonics Technology Letters 31(21), 1741-1744 (2019). The content of this paper is presented in Chapter 4.

   Author contributions:
   H. Liang and K. Liu conceived and designed the experiment. K. Liu did the experiment with the help from H. Liang, W. Li, X. Zou and S. Qu in experimental optimizations and pulse characterization. T. Lang provided some experimental suggestions based on the simulation. Q. J. Wang, H. Liang and Y. Zhang provided the essential infrastructure for the experiment. K. Liu prepared the manuscript. H. Liang, and Q. J. Wang reviewed the manuscript. All authors discussed the results and contributed to the manuscript.

3. K. Liu, H. Liang, S. Qu, W. Li, X. Zou, Y. Zhang and Q. J. Wang, "High-energy mid-infrared intrapulse difference-frequency generation with 5.3% conversion efficiency driven at 3 μm," Optics Express 27(26), 37706-37713 (2019). The content of this paper is presented in Chapter 5.

Author contributions:

H. Liang and K. Liu conceived and designed the experiment. K. Liu did the experiment with the help from H. Liang, S. Qu, W. Li, and X. Zou. S. Qu provided help in IPDFG pulse characterization. W. Li and X. Zou provided help in operating the 3 μm OPCPA system. K. Liu did the simulation work. Q. J. Wang, H. Liang and Y. Zhang provided the essential infrastructure for the experiment. K. Liu wrote the manuscript. H. Liang and Q. J. Wang reviewed the manuscript. All authors discussed the results and contributed to the manuscript.

4. K. Liu, H. Liang, L. Wang, S. Qu, T. Lang, H. Li, Q. J. Wang and Y. Zhang, "Multimicrojoule GaSe-based midinfrared optical parametric amplifier with an ultrabroad idler spectrum covering 4.2–16 μm," Optics Letters 44(4), 1003-1006 (2019). The content of this paper is presented in Chapter 6.

Author contributions:

H. Liang conceived and designed the experiment. K. Liu did the experiment with the help from H. Liang, L. Wang, S. Qu, and H. Li. H. Liang and S. Qu provided help in optimizing the experimental results and gave valuable discussion. L. Wang and H. Li provided help in operating the Ti: sapphire CPA system. K. Liu did the simulation work with the help from T. Lang. Q. J. Wang, H. Liang, H. Li and Y. Zhang provided the essential infrastructure for the experiment. K. Liu wrote the manuscript. H. Liang and Q. J. Wang reviewed the manuscript. All authors discussed the results and contributed to the manuscript.

16/07/2020
. . . .
Date

. . . .
Liu Kun

Acknowledgements

It has been four years since I joined Nanyang Technological University (NTU) as a phD student and Singapore Institute of Manufacturing Technology (SIMTech) as a joint PhD student. I am so lucky to have the opportunity to work and study with so many talented people from NTU and SIMTech. They give me lots of support and help in both life and research through my PhD period. Here, I would like to express my gratitude to all of them.

I would like to thank my supervisor Prof. Wang Qijie in NTU for providing the excellent scientific research platform and constructive academic suggestions. His patient guidance and encouragement enable me towards graduation smoothly. It is Prof. Wang who let me understand that I should treat scientific research in a spirit of openness and inclusiveness. A qualified researcher should keep seeking scientific issues and explore unknown fields all the time. These guidelines help me be able to achieve the leap from textbooks to practices.

I would give my sincere gratitude to my supervisor Dr. Liang Houkun in SIMTech. Dr. Liang is friendly in life and logical in scientific research and I am always inspired by his enthusiasm on work and life. Dr. Liang took me into my current research field and gave me constructive guidelines for my overall PhD journey. Dr. Liang always gave effective feedbacks about the scientific questions I felt confused and discussed with me patiently. Whenever something went wrong in my experiments, Dr. Liang always shared his relevant experience and offered the critical solution timely. I feel so lucky to have his guidance for my PhD journey.

I also want to express my thanks to Dr. Zhang Ying and Dr. Li Hao in SIMTech. Dr. Zhang and Dr. Li provided not only the research platform but also some useful guidelines for my PhD research which benefitted me a lot.

I acknowledge the staffs in SIMTech and NTU I met: Dr. Zou Xiao (NTU/SIMTech), Dr. Li Wenkai (NTU/SIMTech), Dr. Liu Cheng (NTU/SIMTech), Dr. Wang Lifeng (SIMTech), Dr. Sun Biao (SIMTech), Dr. Ng Boon Ping (SIMTech), Dr. Seck Hon Luen (SIMTech), Dr. Zeng Yongquan (NTU), Dr. Chen Shaoxiang (NTU) and the students I met: Mr. Qu Shizhen (NTU), Mr. Ran Qiandong (NTU), and Mr. Chen Yuhao (NTU). They tried their best to give me

encouragement and suggestions in both research and life during my PhD period. With their supporting, I feel confident and positive. I thank all of them and hope they can study or work well in the future.

Finally, I want to say thanks to my parents and friends in China for their support and care.

Table of contents

List of Figures

List of Tables

List of abbreviations

AC	Autocorrelator
AOPDF	Acousto-optic programmable dispersive filter
AR	Anti-reflection
BD	Beam dump
CEP	Carrier-envelope phase
CS	Characterization setups
DFG	Difference frequency generation
DL	Delay line
EOS	Electro-optic sampling
FEL	Free electron laser
FROG	Frequency resolved optical gating
FWM	Four-wave mixing
HHG	High-harmonic generation
HWP	Half-wave plate
IPDFG	Intrapulse difference frequency generation
IAC	Interferometric autocorrelator
LPF	Long-pass filter
Mid-IR	Mid-infrared
MCT	HgCdTe
OPO	Optical parametric oscillator
OPA	Optical parametric amplification
OPCPA	Optical parametric chirped-pulse amplification
OP	Orientation pattern
PBS	Polarization beam splitter
PM	Phase-matching
QCL	Quantum cascade laser
PP	Periodically poled
SFG	Sum frequency generation
SHG	Second-harmonic generation

SCG	Supercontinuum generation
SPM	Self-phase modulation
TFP	Thin-film polarizer
TL	Transform-limited
XUV	Extreme ultraviolet

Abstract

Broadband few-cycle mid-infrared (mid-IR) sources in the wavelength range of 2-50 μm are attracting extensive attention from researchers for their various applications. In contrast with traditional incoherent thermal mid-IR sources that can only provide some frequency-resolved applications, broadband few-cycle mid-IR sources enable more advanced applications which require time-resolved characterizations, such as molecular transition tracing, ultrafast phonon coupling and charge interaction studies under ultrafast excitation in semiconductors. In addition, combined with high peak power and high repetition rate, few-cycle mid-IR sources are also promising tools for high-flux coherent soft X-ray generation with 1 keV photon energy, high-flux incoherent femtosecond hard X-ray generation with 100 keV photon energy and attosecond pulse generation. The recent advances of the optical parametric down-conversion techniques such as optical parametric oscillator (OPO) , optical parametric amplification (OPA), optical parametric chirped-pulse amplification (OPCPA) and difference frequency generation (DFG) provide a pathway of generating broadband few-cycle mid-IR radiations. In this thesis, we focus on the generation of few-cycle, broadband, >3 μm mid-IR pulses with a kHz repetition rate and > 1 μJ pulse energy based on OPCPA, intrapulse DFG (IPDFG) and OPA. Moreover, some efforts have also been made in nonlinear pulse compression, high harmonic generation (HHG) and ultrabroadband supercontinuum generation (SCG) using the developed high-energy, few-cycle mid-IR sources. We summarize our contributions as follows.

1. We design and present a carrier-envelope-phase (CEP) stable 3 μm mid-IR OPCPA system based on PPLN and PPSLT crystals, pumped by a 1030 nm, 1 ps, 10 kHz, Yb: YAG Innoslab laser. The OPCPA system can deliver up to 3 W, 300 μJ, 61 fs pulses centered at 3 μm with a CEP fluctuation of 391 mrad for a 100 s duration. A YAG-based nonlinear pulse compression stage further compresses the 3 μm pulses to 21 fs corresponding to two-cycle pulse width, with a 255 μJ pulse energy. Driven by 3 μm, 21 fs pulses after the nonlinear pulse compression, HHG with up to the 15th order is generated in a 0.5 mm thick ZnO crystal. Compared with HHG driven by 3 μm pulses before the nonlinear pulse compression, one order of magnitude enhancement of the harmonic intensity is demonstrated, revealing the significance of the intensity enhancement of the driving source.

2. To further extend the spectrum to the deeper mid-IR region, we utilize the self-phase modulation (SPM) effect in GaSe to produce an internal signal of IPDFG and report a broadband, > 6 μm, SPM-assisted mid-IR IPDFG source directly driven by 3 μm pulses from the OPCPA system we developed, without the use of the extra nonlinear spectral broadening stage. The IPDFG pulses with a 7-15 μm spectral coverage, a 0.91 μJ pulse energy, and a 9.1 mW output power are generated. The contribution of the SPM effect in the process of IPDFG is confirmed experimentally. The generated IPDFG pulse is compressed to 60fs (1.8-cycle) by adding extra bulk materials. The good compressibility directly verifies the good spectral coherence of IPDFG pulses.

3. By nonlinear pulse compression of 3 μm OPCPA pulses in YAG, the spectrum of 3 μm pulses is broadened to 4.5 μm and an external signal of IPDFG is thus produced. Using such pulses, we boost the efficiency of IPDFG to a record value of up to 5.3%. 5 μJ, 50 mW, 68 fs (2.1 cycles centered at 9.7 μm) IPDFG pulses spanning from 6 to 13.2 μm are obtained. With a suitable focal spot, the field strength of the IPDFG pulses can exceed 0.27 V/Å, enabling some applications in nonlinear optics such as HHG and SCG. As a demonstration, pumped by the IPDFG pulses, a 2.4 μJ, 24 mW SC source with a 3-octave bandwidth covering 2 to 16 μm and a 2.7 μJ, 27 mW SC source with a 2.3-octave bandwidth covering 3 to 14.5 μm are generated in a KRS-5 crystal and a ZnSe crystal, respectively. Two SC spectra both support sub-cycle pulse widths.

4. In the abovementioned works, we have obtained two-cycle mid-IR pulses with a broadband spectrum from 6 to 15 μm and a uJ-level pulse energy based on the IPDFG method. Further, we explore the mid-infrared pulse generation with a broader spectrum supporting sub-cycle pulse width using an OPA method. We present a multi-microjoule, ultra-broadband mid-IR OPA source based on a GaSe nonlinear crystal and a driving source at ~2 μm, which can deliver idler pulses with a spectrum covering 4.5 to 13.3 μm at -3 dB and 4.2 to 16 μm in the full spectral range and a pulse energy of ~3.4 μJ, centered at 8.8 μm. The spectrum supports a sub-cycle transform-limited pulse width of ~19 fs. To our best knowledge, this is the broadest spectrum ever obtained by OPA systems in this spectral region.

Chapter 1 Introduction

1.1 Why mid-IR pulses

In 1800, W. Herschel discovered some invisible spectral components from the sunlight and those components are nowadays recognized as the "infrared" lights with a wavelength range from 0.7 μm to 1 mm [1]. After the discovery, some applications based on the infrared radiations are developed such as analyzing the compositions of celestial bodies and discovering new planets and stars in astronomy [2,3]. In recent decades, such infrared radiations are being available by laser technologies and the laser sources radiating the mid-infrared (mid-IR) part (3-50 μm) within the infrared spectrum are becoming of particular interest to researchers for their applications in science and technology fields. We summarize some applications for the mid-IR sources as follows.
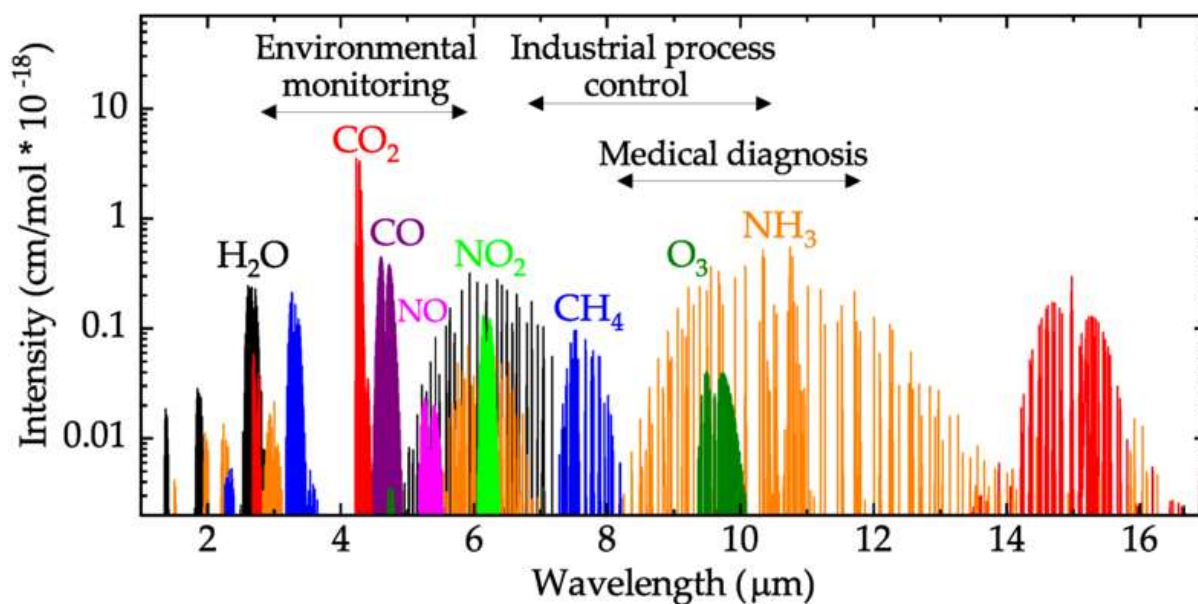
Figure 1.1 The absorption peaks of some molecules in the wavelength range of 2-20 μm. The picture is from the paper [4].

The fundamental vibration-rotational frequencies of most molecules lie in the "molecular fingerprint region" of 2 to 20 μm, the corresponding absorption lines for every molecule in this region are distinguished and specific, refer to Figure 1.1 from the paper [4]. This allows researchers to identify different molecules with the mid-IR spectroscopy. This kind of mid-IR spectroscopy could be applied in industrial process control [5-7], medical diagnosis [8] and environment

monitoring [9, 10]. Currently, thermal sources radiating the mid-IR are extensively used in frequency-resolved mid-IR spectroscopy [11], but the sources exhibit poor spatial coherence and relatively low brightness, which largely limit the sensitivity and spectral resolution of the mid-IR spectroscopy. With the rapid development of ultrafast laser techniques, the ultrafast table-top mid-IR sources with a broadband spectrum and a few-cycle pulse width are pushing the mid-IR spectroscopy into high sensitivity, high spectral resolution and even high temporal resolution for their excellent temporal and spatial coherence nature. For example, using the frequency comb technique based on mid-IR ultrafast lasers, the spectral resolution can even reach the precision of single comb linewidth [12-14]. Excited by few-cycle mid-IR pulses, a coherent electric field with the information of molecular compositions is emitted by the molecules. This electric field can be detected using an electro-optic sampling (EOS) technique, enabling the ultra-sensitive time-resolved mid-IR spectroscopy [15]. Apart from applications in the mid-IR spectroscopy, mid-IR ultrafast sources with high peak power are becoming promising tools in strong-field physics.

The typical example is to drive high harmonic generation (HHG). HHG up-converts the driving photon energy to the higher photon energy and the emitted highest photon energy scales as λ^2 in gases [16] and scales as λ in solids [17] (λ is the wavelength of the driving pulses). Driven by the mid-IR pulses, the high harmonics can reach soft X-ray spectral region (up to 1 keV) in gases [16] and extreme ultraviolet (XUV) region in solids [18]. Soft X-ray pulses are a good tool for probing the structure and tracking the electron dynamics in atomics, molecules and materials at nanoscale [19-21]. In the past, the coherent soft X-ray pulses were usually produced using synchrotrons and free-electron lasers (FELs). However, these facilities have a very large scale and need a very high cost. Therefore, a table-top mid-IR-driven HHG source is a good alternative of these sources. In addition, HHG driven by mid-IR pulses can access a very short wavelength with a very broad spectrum, thus providing an effective solution for the generation of attosecond pulses [22, 23] and the relevant research on the attosecond science [24]. Moreover, the XUV (10-100 eV) pulses produced by the mid-IR-driven HHG also pave a way to manufacture semiconductor items with a smaller size by photolithography.

Another application example of high-energy few-cycle mid-IR pulses in strong-field physics is to drive incoherent femtosecond hard X-ray generation via plasma in metal targets. As the maximum kinetic energy of energic electrons accelerated by the laser field is proportional to λ^2, the energic

electrons accelerated by mid-IR pulses have higher kinetic energy than that by near-IR pluses. The electrons with higher energy add the probability to ionize the inner-shell electrons and thus increase the flux of hard X-ray generation via the electron transition from outer-shell to inner-shell. An experimental evidence was given in paper [25], in which the hard X-ray flux driven at 3.9 μm is 25 times higher than that drive at 0.8 μm with the same driving intensity. Although the hard X-ray pulses have a worse spectral coherence, the spatial coherence is related to the spot dimensions of hard X-ray. A manipulated μm-scale spot size makes the hard X-ray suitable for diffraction imaging with a spatial resolution at an atomic size [26, 27]. Besides, such table-top hard X-ray femtosecond pulses are excellent structure probes in time-resolved X-ray absorption and diffraction [28, 29].

High-energy few-cycle mid-IR pulses can also find their applications in manipulating electrons, such as electron acceleration for the study of fundamental physics [30, 31], laser-induced electron diffraction for imaging of ultrafast molecular dynamics [32] and wave-controlled ultrafast electronics in dielectrics and semiconductors [33,34] and isolated attosecond electron pulse generation [35-37]. There are also many other application examples of mid-IR ultrafast pulses. For instance, mid-IR pulses have a deeper penetration depth in semiconductors and insulators, making them a useful tool for micro-fabrication processes [38]. Mid-IR pulses are also making contributions on the high-resolution imaging and optical coherence tomography without invasion for living tissues [39-41].

Inspired by aforementioned applications, the scope of this thesis is to generate high-energy broadband few-cycle mid-IR pulses. In the next section, we will detail how to produce such pulses.

1.2 How to generate ultrafast mid-IR pulses

Ultrafast laser sources have gain enormous progress since the demonstration of the first ultrafast laser based on a liquid-dye gain medium [42]. Nowadays, the femtosecond solid-state lasers based on Ti: sapphire gain media have been a very mature technology and a dominant driving source for strong-field physical experiments in the laboratories worldwide due to their large gain bandwidth supporting few-cycle duration and good mechanical properties [43, 44]. Ultrafast solid-state lasers based on Yb-doped gain media emitting at 1 μm are well-developed as well. Currently, they can deliver high-power (up to kW-level), high-energy (up to hundred-mJ-level), ps or sub-ps pulses

[45-48]. With a nonlinear spectral broadening and a post compression, the ps or sub-ps pulse width from those lasers can be compressed to few cycles with a good beam quality and a high throughput [49, 50], enabling the Yb: YAG solid-state lasers to challenge the dominant position of Ti: sapphire lasers in strong-field physics. However, ultrafast solid-state lasers emitting the mid-IR are not as mature as that at 0.8 and 1 μm.
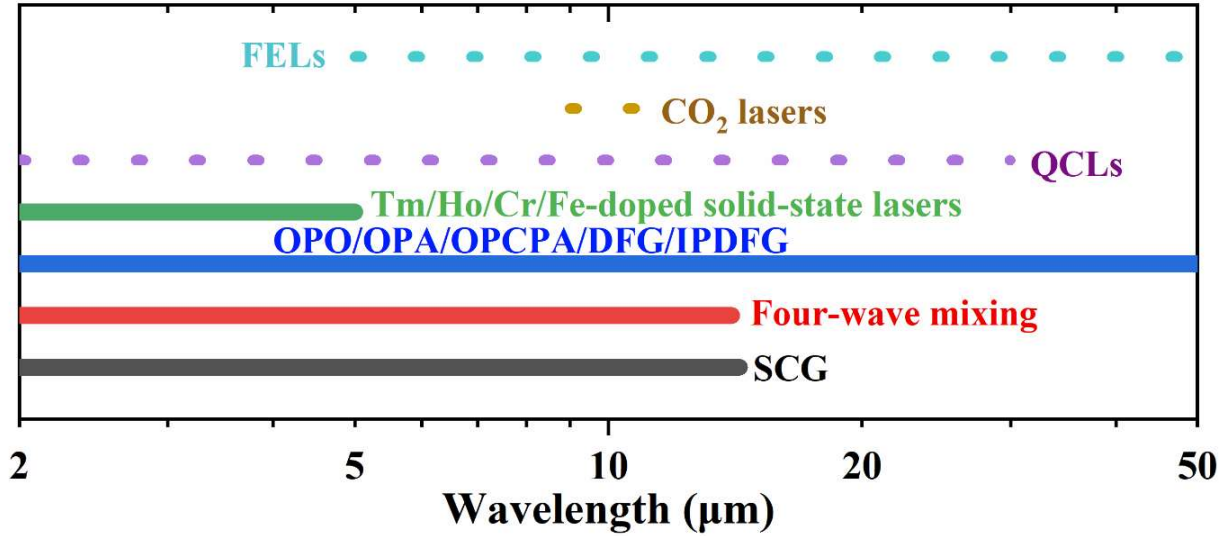
Figure 1.2 The spectral coverage of representative ultrafast mid-IR sources. Narrow-band tunable sources and broadband sources are represented by dotted lines and solid lines, respectively.

Figure 1.2 shows that there are only a few gain media which are suitable for the generation of mid-IR pulses. They only cover the short-wavelength mid-IR region from 2 to 5 μm, such as Tm- or Ho-doped crystals for 1.9-2.1 μm [51-54], Cr or Fe-doped crystals for 2-5μm [55-58]. Although advances have been made in developing these gain media based solid-state lasers, for instance, Ho: YLF solid-state laser was reported for the generation of 260 mJ, 16 ps pulses centered at 2052 nm [54] and Cr: ZnSe solid-state laser was reported to deliver 4 mJ, 44 fs (< 6 cycles), 2.5 μm pulses [56], they only satisfy the several of the above-mentioned applications.

In the methods directly producing mid-IR pulses, beside solid-state lasers, CO_2 lasers, Quantum cascade lasers (QCLs), and FELs are also feasible solutions, see the Figure 1.2. CO_2 lasers can radiate the longer wavelength around 10 μm, but spectral bandwidths are rather narrow and pulse widths are in the order of ps [59, 60]. QCLs can offer a broadly tunable mid-IR radiation from 2 to 30 μm [61, 62], but with a low output power. In addition, QCLs usually need to work at a high

threshold current and a low temperature. FELs radiate high-power, wavelength-tunable mid-IR pulses from 5 to 50 μm by adjusting the undulator period [63, 64]. However, they are building-size facilities and only deliver ns or longer pulses which limit their usability.

Thanks to the invention of optical parametric down-conversion techniques such as optical parametric oscillators (OPOs), optical parametric amplification (OPA), optical parametric chirped-pulse amplification (OPCPA), difference frequency generation (DFG) and intrapulse DFG (IPDFG). The bottlenecks faced by abovementioned mid-IR ultrafast sources can be overcome to some extent. Different from solid-state lasers which are based on the population inversion, optical parametric down-conversion techniques transfer energy from pump to signal by a parametric process occurring at a second-order nonlinear medium (see Chapter 2). During this process, no energy is stored directly in the medium due to the instantaneous nature which largely mitigates the thermal effects. Since the emitted center wavelength and bandwidth by these techniques are determined by phase-matching conditions, we can design mid-IR sources with different center wavelengths and bandwidths by selecting suitable pump sources and nonlinear media. The ability of producing high-power, high-energy, broadband, few-cycle pulses at different mid-IR wavelengths by the optical parametric down-conversion techniques has been demonstrated extensively [65-79]. The pulses provided by those techniques could cover the overall mid-IR region (3-50 μm, see Figure 1.2), with an average power from < 1 mW to >20 W and a pulse energy from < 1 μJ to >30 mJ. For example, mid-IR pulses with a broad spectrum covering from 3 to 8 μm and an average power of 400 mW were obtained in an OPO [65]. Using OPA configuration and a 2 μm driving source, sub-cycle pulses with a 2.5 to 10 μm spectral coverage and a >30 μJ pulse energy were produced [66]. A system, based on the DFG between 1.18 μm and 1.28 μm pulses, covering the frequency components of 1-60 THz (5-300 μm) with a single-cycle pulse width was reported [67]. The near-single-cycle IPDFG source with a 6-18 μm spectral coverage and a 500 mW average power [68] and the ultrabroadband IPDFG source with a spectral coverage of 5-20 μm and a 24 mW average power [69] were reported as well. In terms of energy, OPCPA systems boost few-cycle mid-IR pulse energy up to 2.6 mJ at 2 μm [70], 39 mJ at 3.9 μm [71]，1.0 mJ at 5 μm [72], 0.75 mJ at 7 μm [73]. The ability of OPCPA systems for > 10 W, few-cycle pulse generation has also been verified [74-79]. Therefore, those techniques based on the

optical parametric down-conversion are a versatile method to pursue high-power high-energy broadband few-cycle mid-IR pulses.

In addition, there are other methods to generate broadband ultrafast mid-IR pulses, such as four-wave mixing (FWM) and supercontinuum generation (SCG). FWM and SCG can be used to produce sub-cycle mid-IR pulses [80] and ultrabroad mid-IR spectral coverage [81, 82]. However, the pulse energy obtained by these two methods is usually in the scale of pJ or nJ. It is worth mentioning that SCG is a commonly used method to extend the narrow-band mid-IR spectrum to a multi-octave spectrum covering the molecular fingerprint region. In this thesis, we used SCG to extend the spectral coverage of our mid-IR sources, see the Chapter 5 for details.

1.3 Objectives and challenges

This thesis targets at developing table-top mid-IR sources delivering few-cycle, broadband, >3 μm mid-IR pulses with a kHz repetition rate and > 1 μJ pulse energy based on optical parametric down-conversion techniques which satisfy the requirements of applications such as HHG in gases or in solids, laser-induced electron diffraction imaging, wave-controlled ultrafast electronics in dielectrics and semiconductors and the mid-IR spectroscopy. We adopt OPCPA, IPDFG and OPA techniques for high-power, high-energy, broadband, few-cycle mid-IR pulse generation at 3 μm and 10 μm, respectively. The challenges for such mid-IR sources are listed as follows.

i. To develop the high-power, high-energy, few-cycle 3 μm OPCPA system, we use the 1 μm solid-state laser with a high power, a high energy and a moderate pulse width as the pump source. Based on the pump source, we need to select the nonlinear crystals with the properties of the high damage threshold and the broad phase-matching bandwidth. After the nonlinear crystals are selected, a solution of the seed generation for the 3 μm OPCPA needs to be proposed, which must provide enough broad bandwidth and moderate energy in order to be amplified efficiently. The dispersion management of the OPCPA system is another challenge. Suitable materials providing positive and negative dispersions need to be selected. We also should find a solution to measure the CEP stability of 3 μm pulses. To pursue the two-cycle or even single-cycle pulses at 3 μm, a relevant nonlinear pulse compression technique needs to be exploited.

ii.   To obtain longer-wavelength broadband few-cycle pulses using IPDFG, we propose to use 3 μm pulses as the driver for the benefits of reducing the nonlinear absorption of narrow bandgap nonlinear crystals and the quantum defect between the driving wavelength and IPDFG wavelength. For this IPDFG design, we need to select a nonlinear crystal with the broad transmission, the good phase-matching bandwidth and the high damage threshold. To obtain optimized IPDFG output, the phase-matching type, the phase-matching angle and the pump intensity on the nonlinear crystal need to be determined. Once obtaining the optimized IPDFG output, we need to verify whether there are residual dispersions included in the pulses and investigate how to dechirp the pulses. In addition, some effects contributing to the IPDFG process, such as the SPM effect and the cascade effect, need to be distinguished and analyzed systematically.

iii.   To achieve broadband, few-cycle, long-wavelength mid-IR pulses using OPA, we need to select the pump wavelength and the nonlinear crystal with the good phase-matching bandwidth, the broadband transmission and the high damage threshold. Other challenges are how to generate the broadband seed for the OPA system, how to combine and split the pump and signal in the case of the lack of dichroic mirrors for broadband mid-IR pulses.

iv.   Verify the applicability of these mid-IR sources, such as in HHG and SCG.

1.4 Major contributions

The major contributions of this thesis are as follows:

1.   We design and present the first 3 μm OPCPA system based on the PPSLT crystals. Benefiting from the high damage threshold and the broad phase-matching bandwidth of PPSLT crystals, 3 μm pulses with a 3 W average power, a 300 μJ pulse energy and a 61 fs pulse width are delivered. In addition, using a bulk YAG as the extra nonlinear-compression stage, the pulse width is further compressed to two cycles (21 fs) with a 255 μJ pulse energy. The high pulse energy and short pulse duration enable the HHG investigations in gases or solids. As a demonstration, a 15th -order harmonic of 6.5 eV is generated via HHG in ZnO using nonlinearly compressed 3 μm pulses.

2. We demonstrate the first mid-IR IPDFG source driven at 3 μm. We also investigate the contribution of SPM effect to the IPDFG process experimentally and find that the SPM broadens the spectrum of the driving pulses and produces the signal components of IPDFG. The IPDFG source delivers 10.3 μm mid-IR pulses with a spectral span from 7 to 15 μm, a ~1 μJ pulse energy and a ~10 mW average power. The pulse compressibility from 80 fs to 60 fs (sub-two-cycle) confirms that the mid-IR pulses exhibit a good coherence.

3. We demonstrate an IPDFG source with a record-high conversion efficiency up to 5.3%. The IPDFG sources are based on the nonlinearly compressed pulses from the 3 μm OPCPA system and a GaSe crystal. We produce 5 μJ, 50 mW, 60 fs mid-IR pulses covering 6-13.2 μm. The pulse energy, to the best of our knowledge, is highest in reported mid-IR IPDFG sources. Using the IPDFG pulses as a driver, 3-octave and 2.3-octave SC spectra spanning from 2 to 16 μm and 3 to 14.5 μm are produced in KRS-5 and ZnSe, respectively. Both spectra both support sub-cycle pulse widths.

4. We report a GaSe-based OPA system driven at 2 μm and seeded by SC pulses. Benefitting from the good phase-matching bandwidth of GaSe at 2 μm, the idler spectrum covers 4.2-16 μm with a 3 dB bandwidth from 4.5 to 13.3 μm, which, to the best of our knowledge, is broadest in reported OPA sources. Combined with ~3.4 μJ pulse energy, the OPA source has a potential in molecular spectroscopy and some strong-field experiments in solids.

1.5 Thesis organization

In Chapter 1, the application fields and generation techniques for mid-IR pulses are presented. Subsequently, we provide the details of some optical parametric down-conversion techniques we used in this thesis, i.e. OPA, OPCPA and IPDFG in Chapter 2. Particularly, we also introduce the principle of OPA, the parametric gain, the phase-matching bandwidth and how to satisfy the phase matching in this chapter.

In Chapter 3, the design, experimental setups and experimental results for the 3 μm OPCPA system are introduced in detail, including the crystal selection, the dispersion management, the

characterizations for pulse shape and pulse energy and the CEP measurement. In addition, nonlinear pulse compression in a nonlinear crystal and HHG in a solid are studied as well.

To further generate mid-IR pulses with a longer wavelength, we design and develop an IPDFG source driven by the 3 μm pulses directly from the above developed OPCPA system. The contribution of SPM effect on IPDFG is investigated systematically. All other details are also provided in Chapter 4.

In Chapter 5, we explore and verify the possibility to improve the conversion efficiency of IPDFG, i.e. output energy, with nonlinearly compressed pulses at 3 μm. A comparative analysis with the IPDFG results in Chapter 4 is given. In this chapter, we also study the SCG in nonlinear crystals, multi-octave SC spectra generated in KRS-5 and ZnSe are presented.

The high-energy, ultrabroadband OPA system driven at 2 μm are presented in Chapter 6. The nonlinear crystal, the selected crystal angle, experimental setups, experimental results and the numerical simulation are discussed in detail.

Chapter 7 summarizes about the preceding chapters and gives a conclusion of this thesis. A brief introduction about future work is discussed.

Chapter 2 The optical parametric down-conversion processes in nonlinear media

In this chapter, the details of a few optical parametric down-conversion processes involved in this thesis are introduced. The theoretical part of this chapter can refer to the literatures [83-85].

The light-matter interaction occurs when the light is shined into transparent materials. In the case of weak light intensity, the polarization describing the interaction is linear, with a form:

$$\vec{P} = \varepsilon_0 \chi^{(1)} \vec{E} \tag{2.1}$$

In which, ε_0 is the vacuum permittivity, $\chi^{(1)}$ represents linear susceptibility. From the equation, we can see the optical properties of materials are independent on the electrical field, no wave interaction occurs. However, in the case of intense light, second-, third- and higher-order susceptibilities, i.e. $\chi^{(2)}, \chi^{(3)} \cdots$, become important. The relation between the polarization and the electrical field assuming no losses and no dispersion are nonlinear, with a form:

$$P = \vec{P}_L + \vec{P}_{NL} = \varepsilon_0 (\chi^{(1)}\vec{E} + \chi^{(2)}\vec{E}\vec{E} + \chi^{(3)}\vec{E}\vec{E}\vec{E} + \cdots) \tag{2.2}$$

The relation shows the optical properties strongly depend on the electrical field and nonlinear interactions between waves occur (please also refer to Section 2.1 for a better understanding). The nonlinear interactions generate new frequency components. Therefore, high-order nonlinear process can be used to extend the wavelength range of lasers.

2.1 Optical parametric amplification

For second-order nonlinear materials, we can assume the second-order susceptibility is non-zero and other higher-order susceptibilities are zero. The nonlinear polarization in scalar is expressed as

$$P_{NL} = \varepsilon_0 \chi^{(2)} E^2 = 2\varepsilon_0 d_{eff} E^2 \tag{2.3}$$

Where, d_{eff} is the effective nonlinear coefficient. We also assume three monochromatic waves with frequencies of ω_1, ω_2 and ω_3 ($\omega_3 > \omega_2 > \omega_1$) propagating along z-direction interact, the resulting electric field is

$$E = A_1(z) \exp[-j(\omega_1 t - k_1 z)]$$
$$+ A_2(z) \exp[-j(\omega_2 t - k_2 z)] + A_3(z) \exp[-j(\omega_3 t - k_3 z)] + \text{c. c.} \qquad (2.4)$$

Substituting electrical field E into the equation (2.3), we can find many new frequency components are in the equation (2.3), including frequencies at second harmonic generation (SHG): $2\omega_1$, $2\omega_2$, $2\omega_3$, frequencies at sum frequency generation (SFG): $\omega_1 + \omega_2$, $\omega_2 + \omega_3$, $\omega_1 + \omega_3$ and frequencies at DFG: $\omega_2 - \omega_1$, $\omega_3 - \omega_2$, $\omega_3 - \omega_1$. As for which frequencies are emitted, it depends on the phase-matching condition. We only consider those interactions involving $\omega_1 + \omega_2(= \omega_3)$, $\omega_3 - \omega_1(= \omega_2)$, $\omega_3 - \omega_2(= \omega_1)$ efficiently take place. The nonlinear polarization can be written as

$$P_{NL}(z, t) = 4\varepsilon_0 d_{eff} A_2^*(z) A_3(z) \exp\{-j[\omega_1 t - (k_3 - k_2)z]\}$$
$$+ 4\varepsilon_0 d_{eff} A_1^*(z) A_3(z) \exp\{-j[\omega_2 t - (k_3 - k_1)z]\}$$
$$+ 4\varepsilon_0 d_{eff} A_1(z) A_2(z) \exp\{-j[\omega_3 t - (k_1 + k_2)z]\} + \text{c. c.} \qquad (2.5)$$

and the forcing source term $\partial^2 P_{LN}/\partial t^2$ is

$$\frac{\partial^2 P_{NL}(z, t)}{\partial t^2} = -4\omega_1^2 \varepsilon_0 d_{eff} A_2^*(z) A_3(z) \exp\{-j[\omega_1 t - (k_3 - k_2)z]\}$$
$$- 4\omega_2^2 \varepsilon_0 d_{eff} A_1^*(z) A_3(z) \exp\{-j[\omega_2 t - (k_3 - k_1)z]\}$$
$$- 4\omega_3^2 \varepsilon_0 d_{eff} A_1(z) A_2(z) \exp\{-j[\omega_3 t - (k_1 + k_2)z]\} + \text{c. c.} \qquad (2.6)$$

The scalar nonlinear propagation equation in the z-direction derived from the Maxwell's equations is:

$$\frac{\partial^2 E}{\partial z^2} - \mu_0 \frac{\partial^2 D}{\partial t^2} = \mu_0 \frac{\partial^2 P_{NL}}{\partial t^2} \qquad (2.7)$$

Where, D represents the linear part of electrical displacement field. μ_0 in this equation is the permeability in vacuum. By substituting the forcing term into nonlinear propagation equation and splitting the frequency components in three equations, and applying the slowly varying envelope approximation $|\frac{\partial^2 A_i(z)}{\partial z^2}| \ll 2k_i |\frac{\partial A_i(z)}{\partial z}|$ (i = 1,2,3) [83], we can get coupled-wave equations describing SFG and DFG[84] :

$$\frac{dA_1(z)}{dz} = j\frac{\omega_1 d_{eff}}{n_1 c} A_2^*(z)A_3(z)\exp(j\Delta kz) \tag{2.8}$$

$$\frac{dA_2(z)}{dz} = j\frac{\omega_2 d_{eff}}{n_2 c} A_1^*(z)A_3(z)\exp(j\Delta kz) \tag{2.9}$$

$$\frac{dA_3(z)}{dz} = j\frac{\omega_3 d_{eff}}{n_3 c} A_1(z)A_2\exp(-j\Delta kz) \tag{2.10}$$

Where, $\Delta k = k_3 - k_2 - k_1$ is called the phase-mismatching term. The difference between SFG and DFG lies at the initial input conditions. For SFG, the two low-frequency input waves at ω_1 and ω_2 interact and generate the high-frequency wave at $\omega_3 = \omega_1 + \omega_2$, as shown in Figure 2.1 (upper). For DFG, one high-frequency input wave at ω_3 interacts with one low-frequency input wave at ω_1, another low-frequency wave at $\omega_2 = \omega_3 - \omega_1$ is produced, as shown in Figure 2.1 (lower).
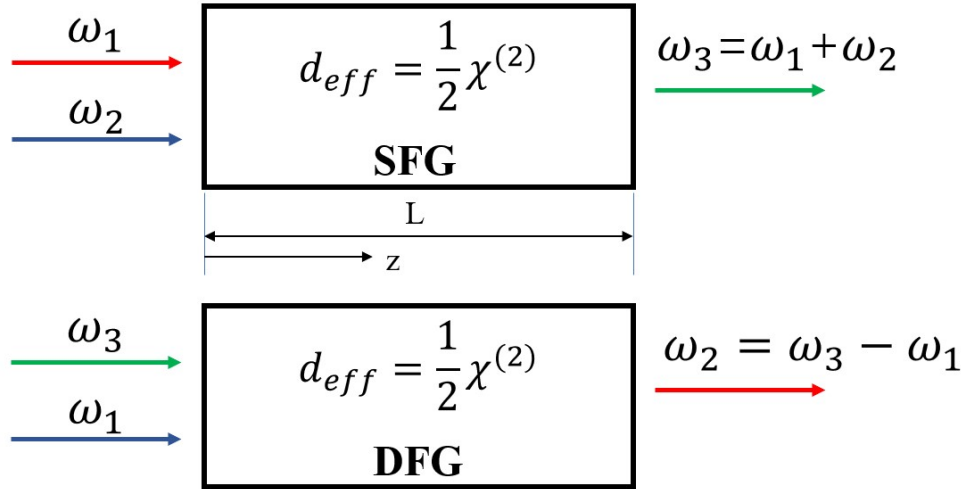
Figure 2.1 Upper: Sum-frequency generation (SFG). Lower: Difference frequency generation (DFG).

A special case for DFG is that when the input waves at ω_1 and ω_3 have very weak and strong intensities, respectively, the wave at ω_1 (signal) absorbs the energy from the wave at ω_3 (pump) and is amplified, simultaneously with the generation of the wave at ω_2 (idler). This special case of DFG is called OPA. The physical process of OPA is shown in Figure 2.2.
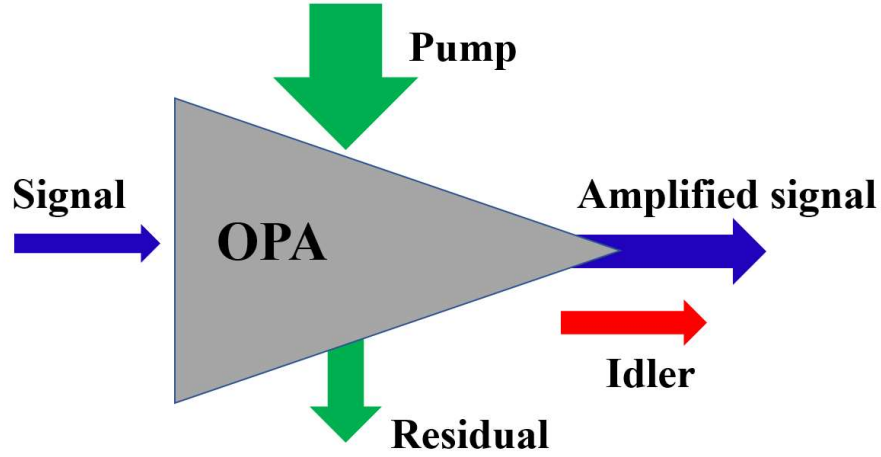
Figure 2. 2 The physical process of OPA.

In the other hand, the Manley–Rowe relation can be derived from the coupled-wave equations (2.8)-(2.10) and is presented as

$$\frac{1}{\omega_1}\frac{dI_1}{dz} = \frac{1}{\omega_2}\frac{dI_2}{dz} = -\frac{1}{\omega_3}\frac{dI_3}{dz} \tag{2.11}$$

Here, $I_i = \frac{1}{2}\varepsilon_0 c n_i |A_i|^2$ ($i = 1,2,3$) is the corresponding frequency intensity. From the equation (2.11), it is found that the photons are conserved in the second-order parametric interaction. Therefore, the OPA process can be understood as the absorption and emission of photons between virtual energy levels. As shown in Figure 2.3, a pump photon at frequency ω_3 is absorbed and excites the material to the highest virtual energy level. Then a signal photon at frequency ω_1 stimulate the emission of a new photon at the same frequency and phase as the signal. This is the principle of amplification. After that, a photon at frequency ω_3 is emitted and decays the material to the ground state. We should also know that due to the instantaneous property of the material response, the photons at frequency ω_1 and ω_3 must go through the same volume of the material simultaneously. Then the two photons collide to produce new frequency. The probability of

collision depends on the number of photons. Thus, to achieve a high conversion efficiency, a high pump intensity and moderate signal intensity are required.
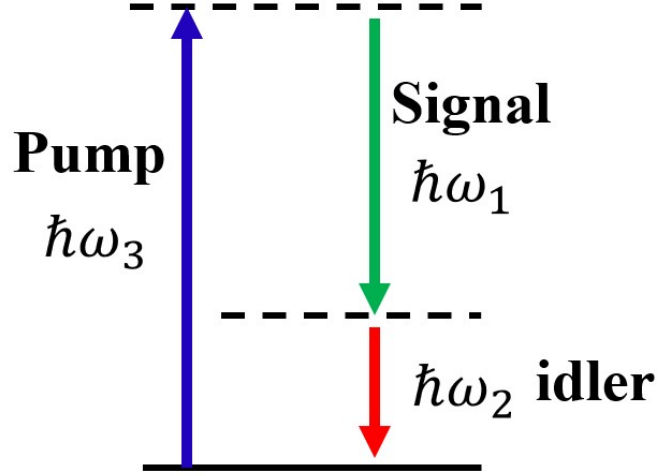
Figure 2.3 The photon explanation of OPA.

2.1.1 Small-signal parametric gain

The small-signal parametric gain expression can be derived from the coupled-wave equations by considering a case of no depleted pump. Assuming the initial signal intensity $I_1 = I_1(0)$, the intensity expressions with the crystal length L for signal and idler are:

$$I_1(L) = I_1(0)\left[1 + \frac{\Gamma^2}{g^2}\sinh^2(gL)\right] \tag{2.12}$$

$$I_2(L) = I_1(0)\frac{\omega_2}{\omega_1}\frac{\Gamma^2}{g^2}\sinh^2(gL) \tag{2.13}$$

Here, $g = \sqrt{\Gamma^2 - (\frac{\Delta k}{2})^2}$, $\Gamma^2 = \frac{2\omega_1\omega_2 d_{eff}^2}{c^3\varepsilon_0 n_1 n_2 n_3}I_3$. The small-signal parametric gain is defined as

$$G(L) = \frac{I_1(L)}{I_1(0)} = 1 + \frac{\Gamma^2}{g^2} \sinh^2(gL) \tag{2.14}$$

When the phase-matching condition is satisfied ($\Delta k = 0$), $g = \Gamma$. Therefore,

$$G(L) = 1 + \sinh^2(gL) \tag{2.15}$$

In the large gain limit of $\Gamma L \gg 1$:

$$G(L) = \frac{1}{4} \exp(2\Gamma L) \tag{2.16}$$

This expression (2.16) shows that under the conditions of the non-depletion approximation and phase-matching, the parametric gain depends on the pump intensity I_3, the effective nonlinear coefficient d_{eff}, and the crystal length L. The gain increases with the crystal length L exponentially. With reasonable selections of those parameters, the resulted gain may be $> 10^6$ [85]. It should be noted that the gain exponential growth as crystal length in OPA is very different from the quadratic growth in other parametric processes like SFG, SHG. The reason for the difference can be understood from photon perspective [85]. In OPA process, under the intense pump, an incident signal photon produces an additional signal photon and a new idler photon. The new produced idler photon further excites an additional idler photon and a signal photon. In other words, the signal photon and idler photon mutually provide the positive feedback, thus the signal and idler can be amplified simultaneously very quickly. This explains why the signal gain grows exponentially as the crystal length L. In addition, in the conditions of $\Delta k = 0$ and $gL \gg 1$, the idler grows exponentially with respect to crystal length as the following expression:

$$I_2(L) = \frac{1}{4} I_1(0) \frac{\omega_2}{\omega_1} \exp(2\Gamma L) \tag{2.17}$$

2.1.2 Gain bandwidth

In the broadband OPA, the phase-mismatching term Δk can be expanded as a Taylor series with respect to signal frequency ω_1. Considering the first-order approximation:

$$\Delta k(\omega_1) = \frac{\partial \Delta k(\omega_1)}{\partial \omega_1}|_{\omega_{10}}(\omega_1 - \omega_{10}) = \left(\frac{\partial k_2}{\partial \omega_2}|_{\omega_{20}} - \frac{\partial k_1}{\partial \omega_1}|_{\omega_{10}}\right) \cdot \Delta\omega = \left(\frac{1}{v_{20}} - \frac{1}{v_{10}}\right) \cdot \Delta\omega \quad (2.18)$$

Where, ω_{10} and ω_{20} are the central frequencies of signal and idler. v_{10} and v_{20} are group velocities of signal and idler. Combined with the equation (2.14), the gain bandwidth of OPA is approximated as

$$\Delta v = \frac{2\sqrt{\ln 2}}{\pi} \sqrt{\frac{\Gamma}{L} \frac{1}{\left|\frac{1}{v_{20}} - \frac{1}{v_{10}}\right|}} \quad (2.19)$$

From this equation, we can find that the gain bandwidth is affected by the group velocities of signal and idler. An extremely large amplification bandwidth could be achieved by matching the group velocities of signal and idler. This matching can be fulfilled at the degeneracy point where the signal and idler wavelength are equal to twice the pump wavelength [86]. Some nonlinear crystals can also find this matching at two sides of its zero-dispersion point. For example, the zero-dispersion point of GaSe is ~5.2 um, and the dependence of group velocity on wavelength around the zero-dispersion point is illustrated in Figure 2.4. It is noted that lots of combinations of signal and idler satisfying group velocity matching can be found. An example is that when the group velocity matching of signal and idler is at 2.73 μm and 9.67 μm, the pump wavelength is 2.13 μm. It is worth mentioning that GaSe always can find such combinations with the ~2 μm pump wavelength. In fact, the real OPA must consider the pump availability, because not every pump wavelength is available due to the limit of laser technology. ~ 2μm wavelength can be accessed by some laser techniques. Therefore, GaSe is a very potential crystal for broadband OPA. This inspires our research on ultrabroadband GaSe OPA driven at ~2 μm, as presented in Chapter 6.

In the case of that the group velocity of signal equals that of idler, the equation (2.19) loses the validity. Second-order approximation of Δk must be considered and the gain bandwidth has the following form:

$$\Delta v = \frac{2(\ln 2)^{\frac{1}{4}}}{\pi} \left(\frac{\Gamma}{L}\right)^{\frac{1}{4}} \frac{1}{\sqrt{\left|\frac{\partial^2 k_1}{\partial \omega_1^2}|_{\omega_{10}} + \frac{\partial^2 k_2}{\partial \omega_2^2}|_{\omega_{20}}\right|}} \quad (2.20)$$
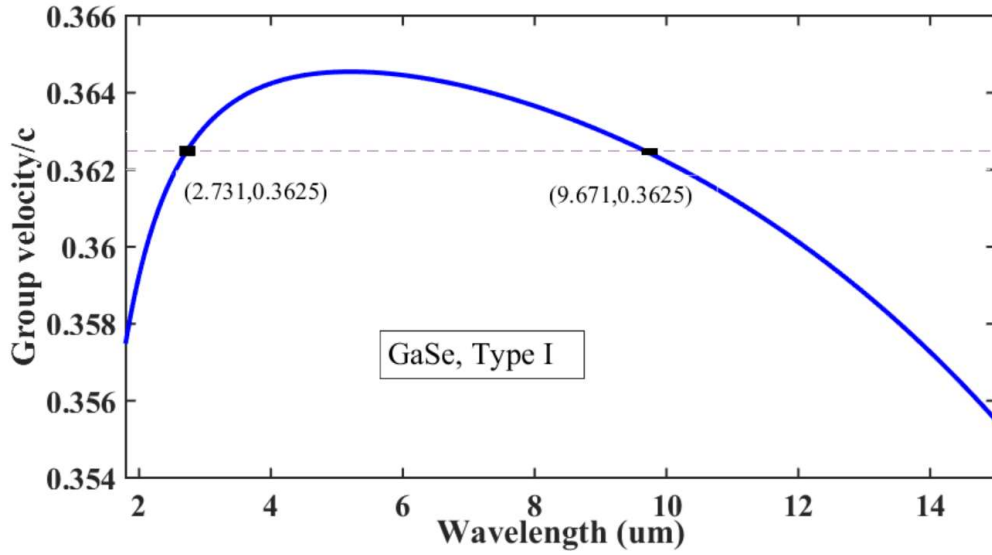
Figure 2.4 The dependence of group velocity of GaSe on wavelength.

2.1.3 Birefringent phase-matching

To obtain the large gain, the phase-matching condition ($\Delta k = 0$) must be fulfilled, namely,

$$n_3\omega_3 = n_1\omega_1 + n_2\omega_2 \tag{2.21}$$

In general case, it is very difficult to fulfill the phase-matching condition in isotropic media. We assume the isotropic media have a positive dispersion ($n_1 < n_2 < n_3$). Therefore, $n_3 - n_2 > 0, n_1 - n_2 < 0$ and the equation (2.21) has no solution. Similarly, when the media have a negative dispersion, this conclusion still holds. However, for birefringent crystals, the case becomes different. In birefringent crystals, the beam propagating along it could have two different refractive indexes depending on the polarization states (ordinary polarization and extraordinary polarization). The beam with an ordinary polarization propagates with the refractive index n_0. However, the beam with an extraordinary polarization propagates with a refractive index changeable from n_0 to n_e dependent on the propagation direction θ. The propagation direction θ is the crossing angle between the beam wavevector $\vec{k}$ and optical axis (z) of the nonlinear crystal, see the Figure 2.5. The dependence of $n_e(\theta)$ on the propagation direction θ in negative uniaxial crystals is given by

17

$$\frac{1}{n_e^2(\theta)} = \frac{\cos^2(\theta)}{n_o^2} + \frac{\sin^2(\theta)}{n_e^2} \tag{2.22}$$
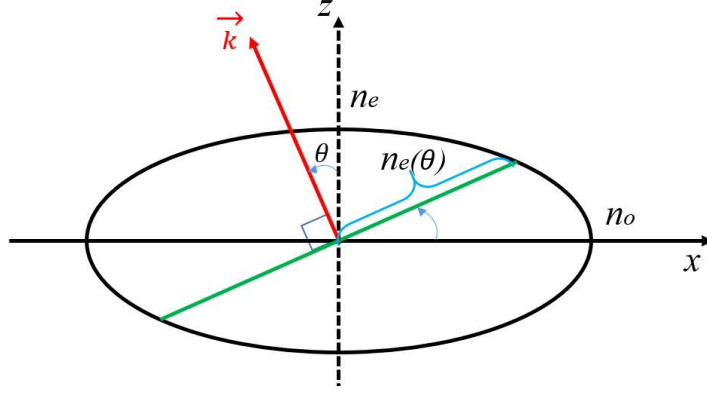
Figure 2. 5 The index ellipsoid of a negative uniaxial crystal, viewed from the negative y direction. $n_e(\theta)$ varies with the propagation direction θ. n_e and n_0 are the semi-minor axis and semi-major axis, respectively.

It is often possible to find a value of θ_m to fulfill the phase-matching condition described by equation (2.21). The type of method to satisfy the phase-matching condition is called birefringent phase-matching and the corresponding θ_m is called phase-matching angle. According to the polarization states of three interacting beams, the phase matching satisfied by birefringence can be classified into two types. If signal and idler have the same polarization states, either ordinary or extraordinary, we call it Type-I phase-matching, the resulting configurations are ooe and eeo. If the signal and idler propagate with different polarizations, that is, they are cross polarized, we call it Type-II phase-matching, which can lead to oeo, eoo,oee and eoe configurations.

Here, we give an example of Type-I phase matching in negative uniaxial crystals to show how to calculate the phase-matching angle θ_m. In negative uniaxial crystal, $n_e < n_0$, in order to achieve phase-matching, the pump must be of extraordinary polarization, so the phase-matching condition is written as

$$n_{3e}(\theta_m)\omega_3 = n_{1o}\omega_1 + n_{2o}\omega_2 \tag{2.23}$$

Here, $n_{3e}(\theta_m)$ is the refractive index of pump, the relationship between $n_{3e}(\theta_m)$ and the refractive indexes n_{3e}, n_{3o} of principal axes is

18

$$\frac{1}{n_{3e}^2(\theta_m)} = \frac{\sin^2(\theta_m)}{n_{3e}^2} + \frac{\cos^2(\theta_m)}{n_{3o}^2} \qquad (2.24)$$

Therefore, the Type-I phase-matching angle in negative uniaxial crystals is calculated as

$$\theta_m = \arcsin\left[\frac{n_{3e}}{n_{3e}(\theta_m)}\sqrt{\frac{n_{3o}^2 - n_{3e}^2(\theta_m)}{n_{3o}^2 - n_{3e}^2}}\right] \qquad (2.25)$$

2.1.4 Quasi phase-matching
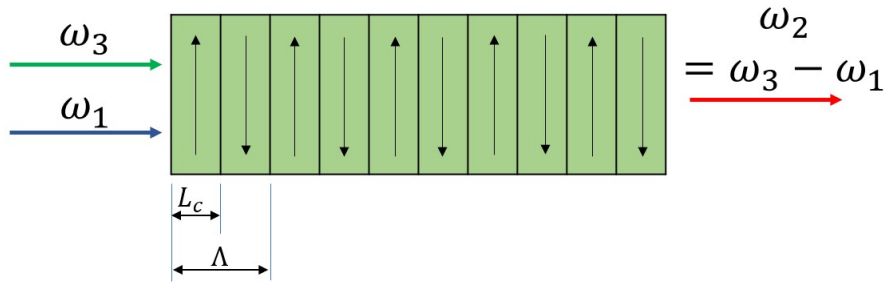
Figure 2.6 The sketch of a periodically poled crystal. The arrows denote the direction of $\chi^{(2)}$. L_c and Λ are the coherent length and poling period.

Quasi phase-matching is another approach to satisfy phase-matching condition, which is achieved by periodically changing the $\chi^{(2)}$ sign of nonlinear crystals, as shown in Figure 2.6. In Quasi phase-matching, the phase-mismatching (Δk) is always non-zero and the phase difference of three waves $0 < \Delta\varphi = \Delta kz < \pi$ when the propagation length z is between 0 and the coherent length L_c $(0 < z < L_c)$. At the position of $z = L_c$, due to the sign change of $\chi^{(2)}$, an extra π phase change is added into the phase difference. This leads to the phase difference $2\pi < \Delta\varphi = \Delta kz + \pi < 3\pi$ for $L_c < z < 2L_c$, so the frequency conversion always occurs within the poling period $\Lambda = 2L_c$. The phase-matching condition of quasi phase-matching can be written as

$$\Delta k = k_3 - k_2 - k_1 - 2\pi/\Lambda = 0 \qquad (2.26)$$

Unlike birefringent phase-matching, the quasi phase-matching crystals are cut at $\theta = 90°$ and the polarizations of three waves are same (Type-0 configuration). This enables quasi phase-matching to utilize the maximum nonlinearity of the crystals and simultaneously avoid the spatial walk-off of three waves due to the wave vectors and Poynting vectors with the same direction along the principal axis of crystals.

2.2 Optical parametric chirped-pulse amplification
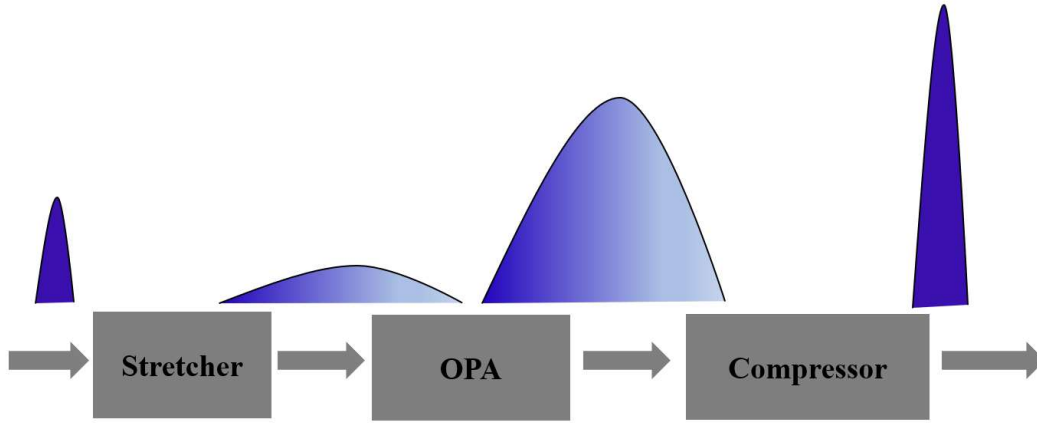
Figure 2.7 The schematic of OPCPA.

The pump and signal pulse widths of OPA are usually in the order of femtosecond. To avoid the crystal damage, the pump energy must be below the crystal damage threshold. This limits the OPA output energy in the uJ level. OPCPA technique is the combination of the OPA and CPA techniques, which is first presented in 1992 [87] and is developed to boost the femtosecond OPA output energy to higher level. In OPCPA, ps or ns narrowband pump is used, therefore a higher pump energy can be used before the crystal damage occurs. The working principle of OPCPA is depicted in Figure 2.7. To extract the pump energy efficiently, the femtosecond seed pulses (signal) is stretched to a wider pulse width matched with that of pump pulses and experience amplification in multi-stage of OPAs. After amplification, the amplified pulses are recompressed to a femtosecond pulse width using compressors. In contrast to CPA based on population inversion, OPCPA can provide shorter femtosecond pulses due to broader gain bandwidth and new wavelength coverage not accessed by the CPA. Moreover, the instantaneous nature of OPA makes

no heat production during amplification, enabling OPCPA to pursue higher average power and higher energy.

2.3 Intrapulse difference frequency generation
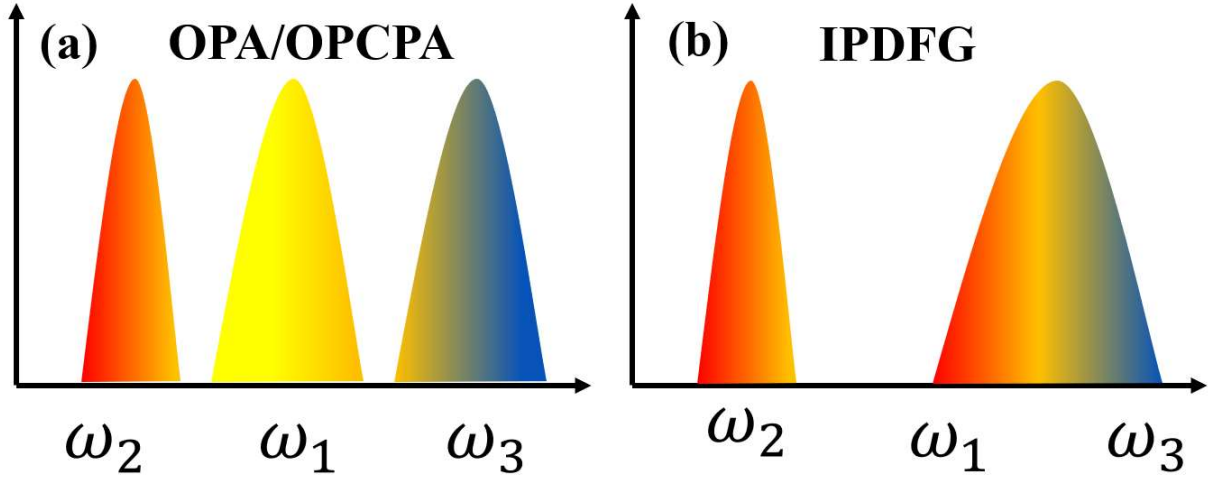
Figure 2.8 The explanations of OPA/OPCPA (a) and IPDFG(b) in frequency domain.

OPA and OPCPA need two separated pulses, the pulse at high frequency ω_3 serves as pump and the pulse at low frequency ω_1 serves as signal. They interact in nonlinear crystals to generate the idler pulse at low frequency ω_2, see Figure 2.8(a). In practical experiments, the pump and signal pulses of OPA and OPCPA are overlapped in time and space by fine beam alignments. Slight beam misalignments caused by beam pointing fluctuations bring some issues to systems, such as low conversion efficiency, idler angular dispersion. In addition, any instability from the system would cause timing jitter between pump and signal pulses, further having impact on the CEP stability. The pump and signal of IPDFG are from the same pulse, see the Figure 2.8(b). The pulse overlaps with itself completely in time and space, so IPDFG neglects some temporal and spatial alignments and overcomes the issues brought by those alignments in OPA and OPCPA. Passive CEP stability is another advantage of IPDFG. The pump and signal within one pulse share the same CEP, so the generated idler is passively CEP-stable due to DFG nature [88, 89]. However, IPDFG has also some disadvantages with respect to OPA and OPCPA. One is that IPDFG needs driving pulses with a broadband spectrum covering the pump and signal frequencies simultaneously. Such broadband pulses are usually obtained from narrow-band pulses via the nonlinear spectral

broadening. This may take some complexities into the system. Another is that IPDFG only utilizes a fractional spectrum at high frequency of driving pulses as pump unlike OPA and OPCPA in which the full spectrum of the pump is used. Thus, the conversion efficiency of IPDFG is lower than that of OPA and OPCPA. However, those disadvantages can be mitigated by selecting a moderately broadband driving source and suitable nonlinear crystals. For example, in Chapter 4, we use a slight narrowband driving spectrum which do not cover the signal components of IPDFG, a broadband idler is still observed. This benefits from the SPM effect of the nonlinear crystal which broadens the spectrum of driving pulses and produces the necessary signal components during IPDFG process. In Chapter 5, we observe an up-to-5.3% IPDFG conversion efficiency by using 3 μm driving pulses with a spectrum covering the pump and signal components of IPDFG. The high conversion efficiency shows that the decrease of quantum defect between the driving wavelength and expected IPDFG wavelength benefits the IPDFG conversion efficiency.

Chapter 3 High-power, high-energy, few-cycle, 3 μm OPCPA

Among the methods of producing mid-IR pulses introduced in Section 1.2 of Chapter 1, OPCPA is a promising method to generate high-power, high-energy, broadband, few-cycle mid-IR pulses satisfying some applications in strong-field physics. The development of such powerful OPCPA systems is highly dependent on the progress of the pump sources. The required pump sources need to provide not only high power and high pulse energy, but also a moderate pulse width. The optimized pumping pulse width of OPCPA systems is in the order of 1 ps, which is a trade-off value by considering the optical damage and the temporal walk-off between pump and signal pulses [90]. As introduced in Section 1.2 in Chapter 1, ultrafast solid-state lasers based on Yb-doped gain media emitting at 1 μm are becoming more and more mature. Currently, they can deliver high-power (up to kW-level), high-energy (up to hundred-mJ-level), ~ 1ps pulses [45-48]. It is obvious that Yb-doped solid-state lasers fulfill all these requirements. OPCPA systems using the compact, cost-effective, powerful, 1-ps-scale, 1 μm pumping offer intense, broad, few-cycle pulse amplification with a high conversion efficiency at some wavelengths not accessed by other techniques. Therefore, we choose a high-power, high-energy, 1-ps-scale Yb-doped solid-state laser as the pump of our OPCPA system. The pump source we used is a commercial Yb: YAG solid-state laser based on CPA and Innoslab amplification technologies. It can deliver 120 W, 12 mJ, 1 ps, 10 kHz pulses centered at 1030 nm (AMPHOS 100) with a possibility to upgrade to a 30 mJ pulse energy (AMPHOS 300). Based on such a pump source, we design and present a CEP-stable 3 μm OPCPA system with a 300 μJ pulse energy, a 3 W average power, and a 61fs pulse width at a repetition rate of 10 kHz.

In this chapter, we introduce the overall OPCPA system in detail including the seed generation, the selection of the nonlinear crystal, the dispersion management and the CEP stability measurement. In addition, to pursue a shorter pulse width, the nonlinear pulse compression in YAG is also investigated. Two-cycle (21fs) pulses are obtained with a 255 μJ pulse energy after YAG. Using such pulses, we also generate a broadband HHG spectrum with up to the 15th order in a 0.5 mm thick ZnO crystal. Compared with HHG driven by 3 μm pulses before the nonlinear pulse compression, one order of magnitude enhancement of the harmonic intensity is demonstrated,

revealing the significance of the intensity enhancement of the driving source. The results shown in this chapter were published in [91].

3.1 Seed generation
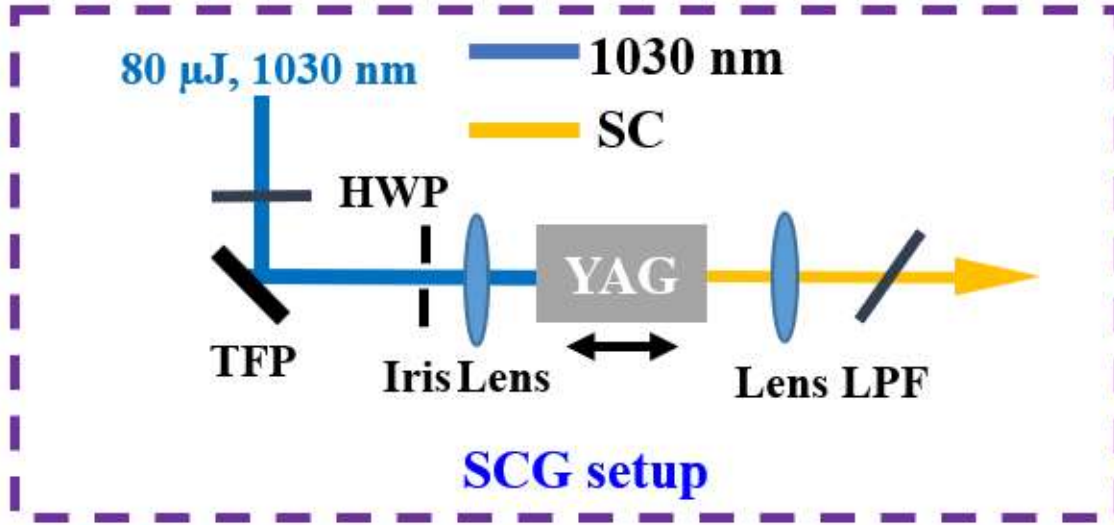
Figure 3.1 The optical schematic of supercontinuum generation (SCG). HWP: half-wave plate. TFP: thin film polarizer. LPF: long-pass filter.

The 3 μm OPCPA systems pumped by 1-100 ps Yb: YAG or Nd: YVO$_4$ solid-state lasers have been demonstrated to seed with a 1.5 μm Er-doped femtosecond fiber laser [92, 93], a DFG source [77, 78, 94] or an OPO source [95]. Those seed sources provide the suitable broadband spectrum at 1.5 μm or 3 μm, but these independent seed setups are usually complicated, which add the complexity and the cost of the overall OPCPA system. Moreover, if the front end used to generate the seed is independent on the amplification chain, an extra electronic locking is even needed to synchronize the seed and the pump pulses. This, to some extent, decreases the long-term stability of the system. Luckily, the broadband SC is becoming a good alternative for the above-mentioned seeds due to its simplified setup. Provided that SC can be directly generated using a fractional energy of the ps OPCPA pump, passively optical synchronization between seed and pump is also simultaneously achieved [96], neglecting the need of electronic synchronization systems. More importantly, in this case, the ps pulses for SCG and OPCPA are both from the same pump and therefore share the same CEP. This also makes it possible to build up a passive CEP-stable OPCPA

system. Based on these reasons, we developed an ultrabroadband ps-pulses-pumped SCG in a bulk-shape YAG crystal, pumped by a small fraction of energy from a 120 W, 12 mJ, 1 ps, 1030 nm Yb:YAG Innoslab laser at a 10 kHz repetition rate. The generated 1.5 μm frequency components from the SC source is especially suitable for seeding the 3 μm OPCPA system.

Table 3.1 The specifications for some common crystals. The nonlinear refractive indices (n_2) are from [97] and the damage thresholds are from [98]. λ_0 and n_2 represent the zero dispersion point and the nonlinear refractive index, respectively.

Crystals	λ_0	n_2 at 1 μm	Damage threshold (J/cm^2)
	(μm)	(10^{-16}cm^2/W)	@ 1.03 μm, 500 fs
YAG	1.6	7.3	7.5
Quartz	1.27	3	5.36
Sapphire	1.3	2.9	5.36
CaF$_2$	1.67	1.24	5.17
BaF$_2$	1.92	-	2.91

When the peak power of pulses is higher than the critical peak power P_{cr} for self-focusing and the media thickness is longer than the self-focusing length, the filament is generated due to self-focusing and plasma formation [99]. Here, $P_{cr} = 3.77\lambda^2/(8\pi n_0 n_2)$ where λ is the laser wavelength, n_0 is the linear refractive index and n_2 is the nonlinear refractive index. In the filamentation, SPM broadens the spectrum of pulses [100]. A simplest model for SPM is shown in the equation (3.1) in which ω(t), ω_0 and I(t) are the instantaneous frequency and central frequency field-intensity of driving pulses.

$$\omega(t) \sim \omega_0 - \frac{n_2 \omega_0}{c} z \frac{\partial I(t)}{\partial t}$$ (3.1)

It can be noted from the equation (3.1) that SPM gets stronger in the filamentation as the beam shrinks and the intensity I(t) gets higher. Therefore, the filamentation in crystals is adopted to produce the broadband SCG. The experimental setup for SCG is shown in Figure 3.1. ~ 80 μJ energy is split from the Yb:YAG Innoslab laser for SCG. The nonlinear crystal for SCG is a YAG crystal with a 16-mm thickness which is fixed on a one-dimension linear stage. YAG is chosen due to its high nonlinear refractive index and high damage threshold compared with other crystals such as Quartz, Sapphire, CaF_2 and BaF_2, see the Table 3.1. The pump pulses are coupled into the YAG crystal by an anti-reflection (AR)-coated convex lens at 1030 nm with a focal length of 100 mm. To avoid the optical damage, the YAG is always placed after the focal spot of the lens. For the stable SCG assisted by filamentation, the intensity and the divergence of pump in YAG are carefully adjusted by the variable attenuator which is a combination of a half-wave plate (HWP) and a thin film polarizer (TFP), the iris aperture and the crystal position from the focal spot. The generated SC is then collimated and filtered out by a coated lens with 50 mm focal length and a long-pass filter (LPF) with a cut-off wavelength of 1180 nm. When the pump energy after iris is ~10 μJ and the crystal is ~3 mm away from the focal spot. The optimized SC output is achieved with the longest wavelength edge up to 2000 nm in the spectrum, see the Figure 3.2(a). The big notch at~1350 nm in the spectrum is due to water absorption in air. The measured SC energy at >1180 nm is 9.3 nJ, with an energy fluctuation of 1.9% for two-hour operation duration, as shown in Figure 3.2 (b). With the nJ pulse energy and broad bandwidth at 1.5 μm, this SC is suitable for seeding the 3 μm OPCPA system.
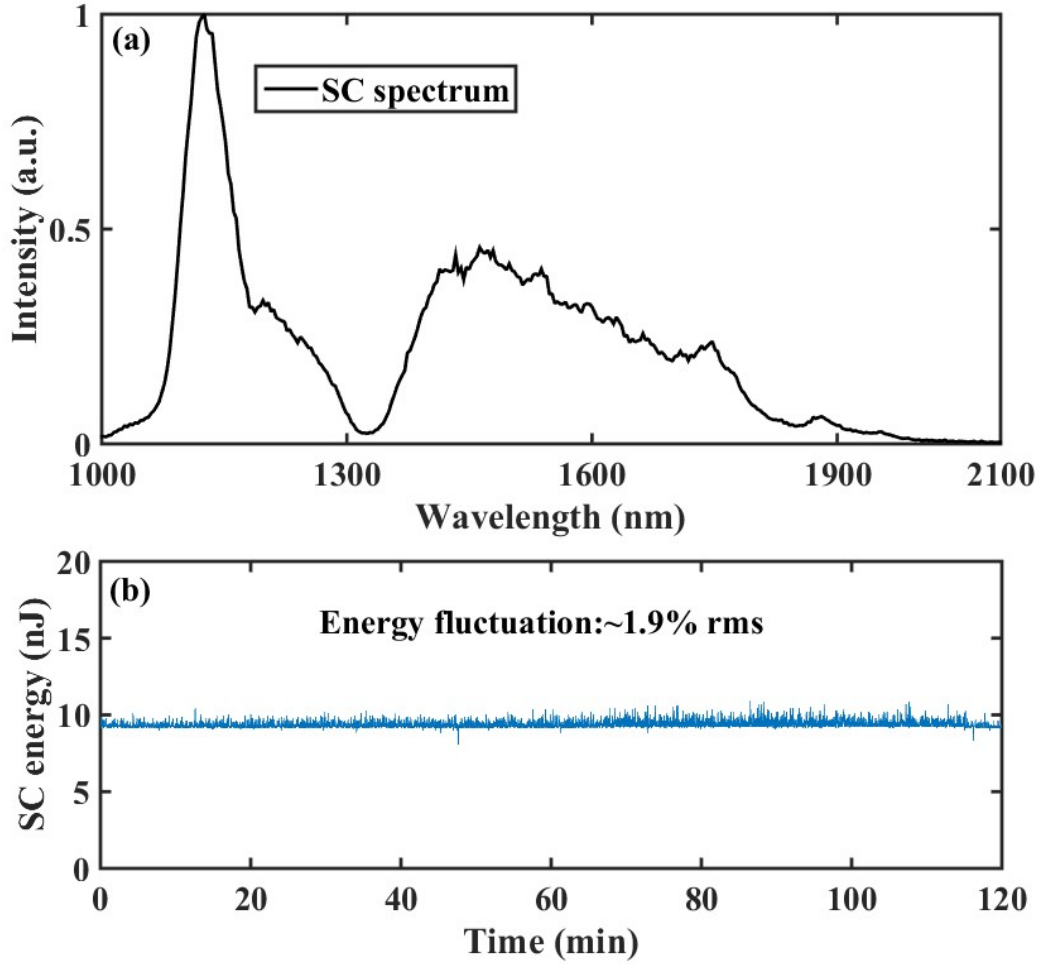
Figure 3.2 SC spectrum (a) and energy stability (b) from YAG after the LPF.

3.2 Nonlinear crystals and dispersion management

To obtain high-energy, few-cycle, mid-IR pulses at 3 μm, the selected crystals for the OPCPA system must have a good phase-matching, a broad transmission window and a high damage threshold. Table 3.2 lists the specifications of a few nonlinear oxide crystals suitable for broadband few-cycle pulse generation at 3 μm, in which the noncollinear angles for the broad amplification, the signal wavelength for seeding and the effective nonlinear coefficients (d_{eff}) are obtained from SNLO [101]. The transmission ranges and damage thresholds are from [102]. For those crystals, while KTP has a moderate nonlinear coefficient and provides broadband phase-matching bandwidth, it is not commonly used due to its large transmission loss at >3 μm. Other crystals have been extensively used for different mid-IR OPCPA systems. Bulk KTA and MgO: LN crystals

with large apertures were used for high-energy, Hz-rate, mid-IR OPCPA systems [71, 103, 104]. 3.9 μm, 35 mJ, 100 fs pulses at a 20 Hz repetition rate [71] and 3.3 μm, 31 mJ, 70 fs pulses at a repetition rate of 10 Hz [104] were delivered. $KNbO_3$- and KTA-based mid-IR OPCPA systems were reported for the generation of 21 W, 131 μJ, 97 fs, 160 kHz-rate pulses centered at 3.25 μm [77] and the generation of 12.5 W, 125 μJ, 73 fs, 100 kHz-rate pulses centered at 3.1 μm [78]. Based on these results, we can find that KTA, MgO: LN and $KNbO_3$ are suitable for > 70 fs few-cycle pulse generation. It is worth mention that the good phase-matching bandwidth supporting ~70 fs pulse width in KTA must be achieved in a noncollinear geometry with a 1.5 μm seed, see Table 3.2. This means that there exists a large angular dispersion in the generated idler pulses at 3 μm. Some extra components such as gratings must be used to compensate the angular dispersion of 3 μm pulses and this takes some complexities into the system [78]. PPLN or apodized PPLN with quasi phase-matching has been used to pursue shorter pulse width in the mid-IR OPCPA systems [92, 105, 106]. 3.1 μm pulses as short as 38 fs were generated [106]. However, the pulse energy is only 40 μJ, which is hindered by the low damage threshold of PPLN (~10 GW/cm^2 at 6 ps [102]). The PPSLT has a larger damage threshold of 80-180 GW/cm^2 [102, 107-109] which is one order of magnitude higher than that of PPLN. While the PPST has not demonstrated for OPCPA systems at 3 μm, the ~2 μm PPSLT-based OPCPA systems working at the degenerated wavelength can deliver pulses with hundreds of uJ pulse energy and few-cycle pulse width [107,108]. This shows its potential in boosting the pulse energy of mid-IR few-cycle pulses. Compared with PPLN, the phase-matching bandwidth of PPSLT at ~3 μm is slightly smaller (233 nm and195 nm in 2 mm thick PPLN and PPSLT, respectively [102]). This issue can be mitigated by using thinner PPSLT and applying higher pump intensity in the OPCPA, because the gain bandwidth of OPA is proportional to the pump intensity and inversely proportional to the crystal length, as predicted by the equation (2.19). It is also worth mentioning that compared to the birefringent phase-matching nonlinear crystals such as KTA, MgO: LN, and $KNbO_3$, PPSLT has a larger effective nonlinear coefficient (7.7 pm/V). Therefore, PPSLT is a good candidate for high energy, few-cycle OPCPA systems at ~3 μm. Considering that the PPLN and PPSLT both support the wide amplification bandwidth and PPSLT has a higher damage threshold, we use PPLN as nonlinear crystals for the first two stages of our OPCPA system due to the relatively low pump intensity and PPSLT as nonlinear crystals of the last two stages in which a higher pump intensity is used.

Table 3.2 Nonlinear crystals for the broadband parametric amplification at 3 μm. The optimized noncollinear angles for the broadband amplification, the signal wavelength for seeding and the effective nonlinear coefficients (d_{eff}) are obtained from SNLO [101]. The transmission range and damage threshold are from [102].

Oxide Crystals	Noncollinear angle for broadband amplification	Signal	d_{eff} (pm/V)	Transmission range (μm)	Damage threshold at 1 μm (GW/cm^2)
MgO: LN	5 deg for Type-I	3000 nm	-4.0	0.33-5.5	10 (6 ps)
LIO	2.7 deg for Type-I	3000 nm	1.17	0.3-6.0	19 (45 ps)
KNbO$_3$	4 deg for Type-I	3000 nm	6	0.4-4.5	100 (100 ps)
KTA	4 deg for Type-II	1568.5 nm	-2.5	0.35-4.0	>1.2 (8 ns)
KTP	3.5 deg for Type-II	1568.5 nm	-2.7	0.35-4.0	15 (1 ns)
PPSLT	0 deg for Type-0	1568.5 or 3000 nm	7.7	0.38-5.5	>80 (30 ps)
PPLN	0 deg for Type-0	1568.5 or 3000 nm	14.8	0.33-5.5	10 (6 ps)

Another important aspect to consider when we design an OPCPA system is the dispersion management of the system, i.e. how to chirp and dechirp the pulses. From the Figure 3.1(a), we can see that the seed for the OPCPA system is enough wide in spectrum and the estimated pulse width of 1.5 μm pulses is less than 60 fs. However, the pump duration is ~1 ps, ~20 time longer than the seed. For the efficient amplification, the 1.5 μm seed pulse must be chirped to a longer pulse width to extract the energy from the pump pulses more efficiently. A few methods may be used to stretch the pulse duration, such as grating pairs, chirped mirrors and solid materials with a large second-order dispersion at the corresponding working wavelength. Grating pairs can provide a high positive or negative second-order dispersion with an accurate control of the dispersion amount by adjusting the distance between grating pairs, but a complicated alignment is needed. Chirped mirrors to chirp or dechirp pulses usually need multiple mirror reflections for reaching enough high dispersion. This causes large reflection losses. Solid materials are a feasible

alternative for grating pairs and chirped mirrors due to the nature of the easy alignment and low loss. For our OPCPA system, we choose the Si and Sapphire to serve as the stretcher to chirp 1568.5 nm or 3000 nm signal/idler pulses and the compressor to dechirp the 3000 nm pulses, respectively. Since these two types of crystals have highest second-order dispersion at the corresponding wavelength, see Table 3.3. Considering that the crystal thickness is hard to change for an accurate dispersion management, an acousto-optic programmable dispersive filter (AOPDF) (Fastlite, Dazzler) working at 1.5 μm is inserted to serve as a stretcher as well. The AOPDF can not only accurately adjust the second-order dispersion, but also control the third-order dispersion and even forth-order dispersion brought by the optics and the crystals. One issue worth to mention here is that when 1.5 μm pulses are chirped using Si, the pulses are at positive second-order dispersion. Based on the signal/idler dispersion relationship during the OPA process, the 3 μm second-order dispersion is negative. Si should be the most suitable crystal for the compression of 3 μm pulses. However, in our experiment, some unknown loss is found when Si is used as a compressor, possibly from multiphoton absorption. Therefore, Sapphire is chosen as the compressor. In this case, in order to make the second-order dispersion of 3 μm pulses to be positive, a large positive second-order dispersion is added to the 1.5 μm pulses using AOPDF. The experimental details for this are introduced in next section.

Table 3.3 The second- and third-order dispersions for common crystals at 1.5 μm and 3 μm.

Solid materials	β_2 at 1568.5 nm $(\mathbf{fs^2/mm})$	β_2 at 3000 nm $(\mathbf{fs^2/mm})$	β_3 at 1568.5 nm $(\mathbf{fs^3/mm})$	β_3 at 3000 nm $(\mathbf{fs^3/mm})$
Si	4930.6	721	21559	2073
YAG	4.6	-360	165.4	2179
Sapphire	-30	-534	158.7	3620
ZnSe	378.4	161	386.6	440
ZnS	224	61	239	456.4

3.3 OPCPA results
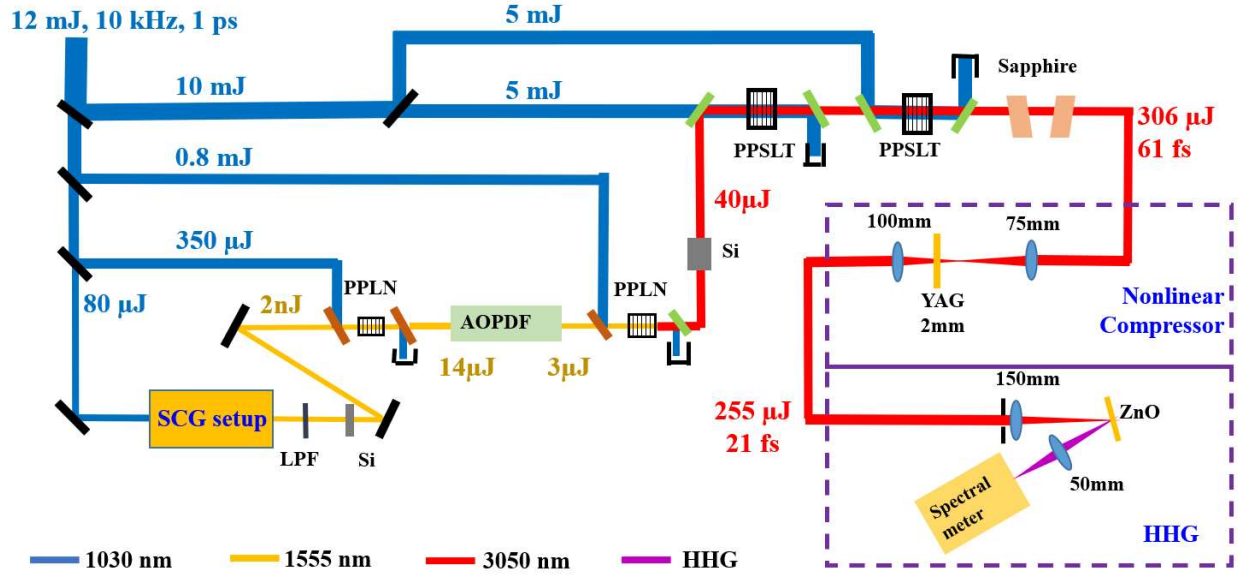
Figure 3.3 The schematic of the 3 μm OPCPA system using PPLN and PPSLT as nonlinear crystals followed by the nonlinear pulse compression and the high-harmonic generation (HHG). AOPDF: Acousto-optic programmable dispersive filter.

The schematic of the 3 μm OPCPA system is shown in Figure 3.3. It starts from a 1030 nm Yb:YAG Innoslab laser. An 80 μJ, 1030 nm pump is split to generate SC in the SCG setup described in Section 3.1. 1.5 μm pulses with 2 nJ pulse energy are obtained after the LPF with a cut-off wavelength of 1300 nm and they are subsequently stretched to ~300 fs pulse width by a 4 mm thick Si block and are injected into the OPCPA system with four-stage amplifiers in a collinear geometry. The first-stage amplifier is based on an uncoated, 3 mm thick 5%-MgO-doped PPLN crystal (HC Photonics). ~ 350 μJ pump energy is distributed to this stage, which amplifies the 1.5 μm seed pulses to a pulse energy of 14 μJ. Figure 3.4 shows the amplified spectrum spans from 1400 nm to 1700 nm, supporting a ~30 fs transform-limited (TL) pulse width. This sufficiently verifies the good phase-matching bandwidth of PPLN. To invert the pulse chirp from positive to negative and stretch the pulse width to a scale matched with the pump pulse width, as analyzed in Section 3.2. An AOPDF is used, which adds -22500 fs^2 second-order dispersion into 1.5 μm pulses. After the AOPDF, the 1.5 μm pulses have an 850 fs pulse width and a 3 μJ pulse energy. ~79% energy loss is found, which is attributed to the diffraction loss of AOPDF.
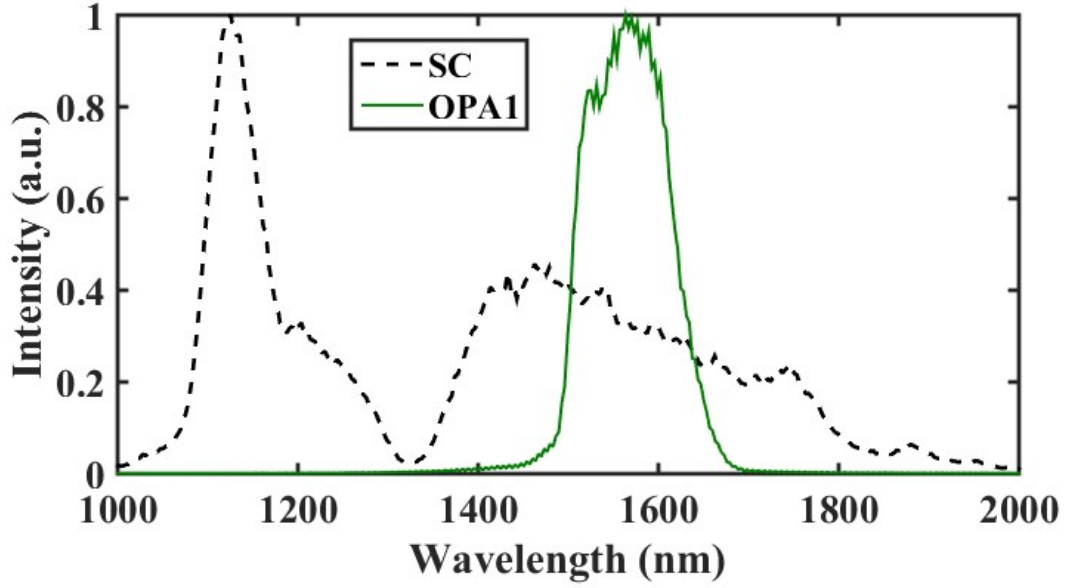
Figure 3.4 The spectrum of 1.5 μm pulses from the first-stage amplifier with a comparison of the SC spectrum.

In the second-stage amplifier, the same thick uncoated PPLN crystal is used. With a pump energy of 800 μJ, 40 μJ, 3 μm idler pulses are obtained with a spectrum covering 2600 nm to 3250 nm (the black curve in Figure 3.5 (a)). The bandwidth matches well with that predicted by the phase-matching function $|sinc(\Delta kL/2)|$ [67], see the black curve of Figure 3.5 (b). Although the 3 μm idler pulses has a positive chirp as expected, the amount is rather small due to the chirp impact from the pump pulses. Thus, a 7 mm thick AR-coated Si block are used to further stretch the pulses to ~700 fs by adding +5047 fs^2 second-order dispersion. After that, the 3 μm idler pulses are used to seed the last two-stage amplifiers based on 1.2 mm and 0.9 mm thick uncoated PPSLT crystals (Deltronic Crystal) with 3 mm×10 mm apertures to boost energy further. The working temperature of the PPSLT crystals are both set at 170°C for mitigating the photorefractive effect. Taking into account the high damage threshold of PPLST, 5 mJ pulse energy is distributed to each stage and the corresponding pump intensity on PPLST is ~140 GW/cm^2. 160 μJ and 306 μJ 3 μm pulses are obtained for the third- and fourth-stage amplifiers, respectively. No crystal damage and beam distortion are observed. The total efficiency of the OPCPA system from pump to idler is 2.6%. The low efficiency may be caused by the large losses from the Fresnel reflection on the uncoated PPSLT crystals. Therefore, the efficiency could be further enhanced by the AR-coated crystals.

32
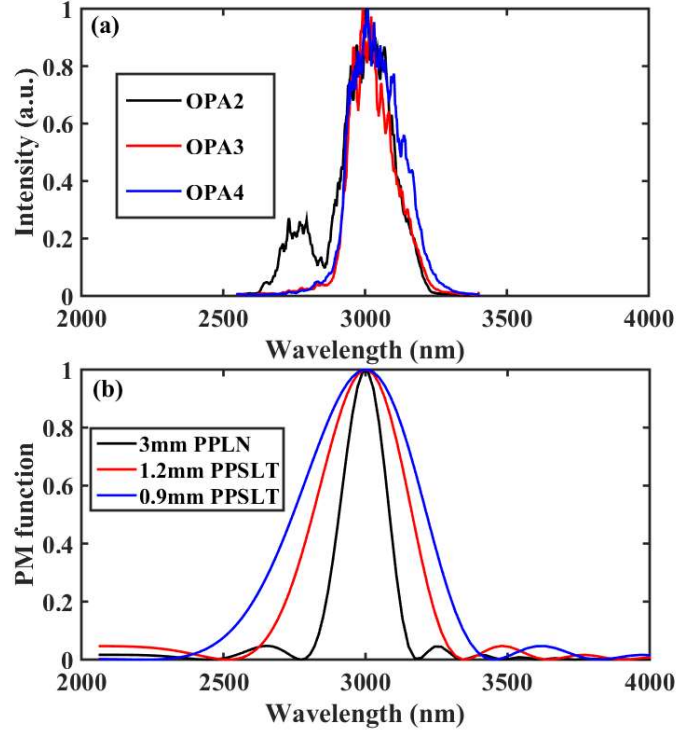
Figure 3.5 (a) The spectra of 3 μm pulses from the second-, third- and fourth-stage amplifiers. (b) The phase-matching (PM) function $|\text{sinc}(\Delta kL/2)|$ [67] for the 3 mm thick PPLN crystal in the second-stage amplifier, 1.2 mm thick PPSLT crystal in the third-stage amplifier and 0.9 mm thick PPSLT crystal in the fourth-state amplifier.

The spectra from the last two-stage amplifiers are characterized and shown as the red and blue curves in Figure 3.5(a). Although PPLST has a slightly narrower phase-matching bandwidth than PPLN when the same thick crystal is used, the PPSLT crystals are >2.5 times thinner than PPLN in our OPCPA system. From the phase-matching curves in Figure 3.5(b), we can find that the phase-matching bandwidths of two PPSLT crystals are broader. Therefore, we did not find the obvious spectral narrowing for the last two-stage amplifiers compared to the second-stage amplifier. In addition, the phase-matching curves also explain why the fourth-stage amplifier has a broader spectrum than the third-stage amplifier. The pulse width of 3 μm pulses from the final-stage amplifier is ~500 fs and the spectrum supports a 60 fs TL pulse width. +10700 fs^2 second-order dispersion is included in the pulses. Therefore, 20 mm thick Sapphire blocks cut at Brewster angles as a compressor are used to compensate the second-order dispersion. It is worth mentioning that beside second-order dispersion, +100000 fs^3 third-order and +650000 fs^4 fourth-order

dispersions from nonlinear crystals, Si blocks, Sapphire blocks and other optics are also included in the pulses. These high-order dispersions are compensated by the AOPDF.
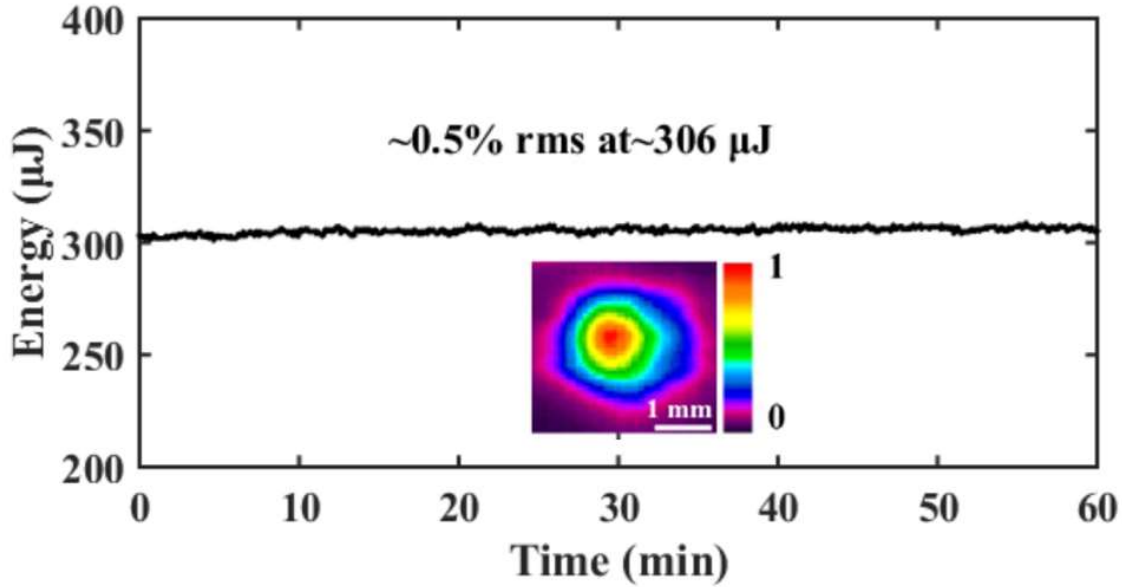
Figure 3.6 Long-term stability of the 3 μm pulses at 300 μJ pulse energy. The inset shows the measured beam profile at 300 μJ pulse energy.

After the compressor, we measured the energy stability for a 1-hour measurement duration and the beam profile of 3 μm pulses at 306 μJ output energy, which is shown in Figure 3.6. The energy fluctuation is ~0.5%. It is much smaller than the energy fluctuation of SC seed, possibly related to the saturation amplification in the last two-stage amplifiers. The inset of Figure 3.6 reveals the beam profile of 3 μm pulses has a Gaussian distribution, indicating the good focus in strong-filed physics. The temporal profiles of the 3 μm pulses are characterized using a commercial SHG frequency-resolved optical gating (SHG-FROG) from FROGscan. A 30 μm thick GaSe is used as the SHG crystal for its broad SHG PM bandwidth and the SHG signal is acquired by the spectrometer from Ocean optics (NIRQuest, 900-2500 nm). The measured and retrieved FROG traces together with the retrieved temporal and spectral profiles are shown in Figure 3.7. 61 fs pulse width is measured, which is almost equal to the TL pulse width of the measured idler spectrum.
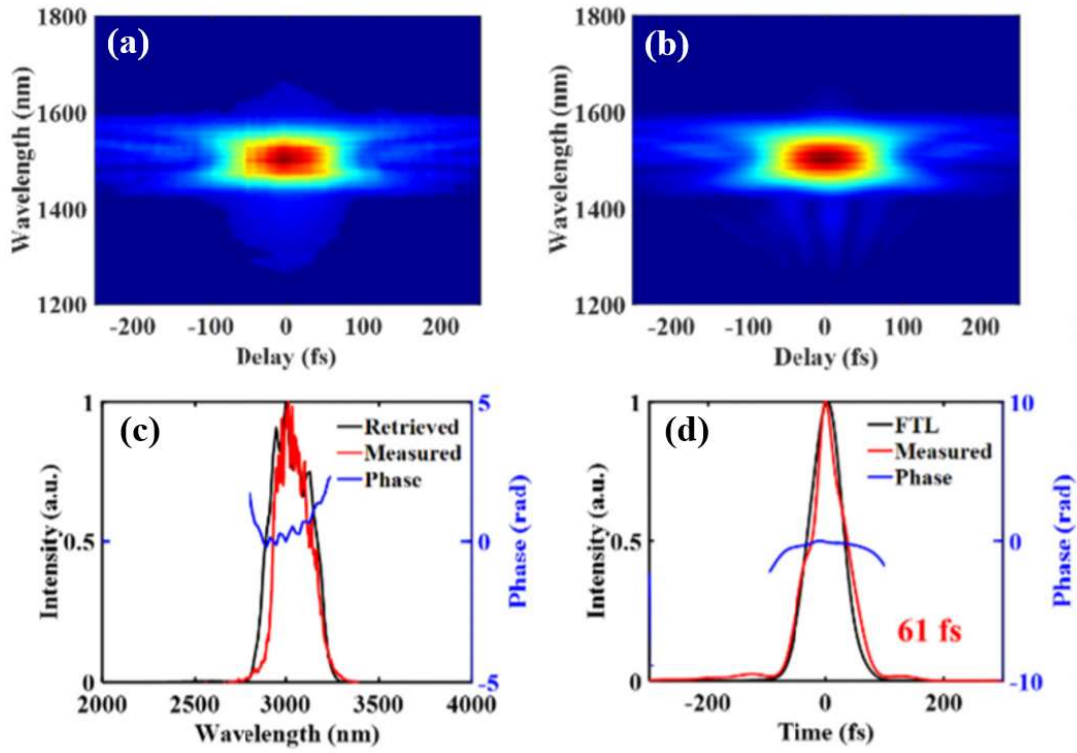
Figure 3.7 The measured FROG results of 3 μm pulses at 306 μJ. Measured (a) and retrieved (b) FROG traces. (c) Measured and retrieved spectra. (d) Retrieved pulse shape and phase. The Frog error is 0.9% with a free frequency marginal.

3.4 CEP stability measurement
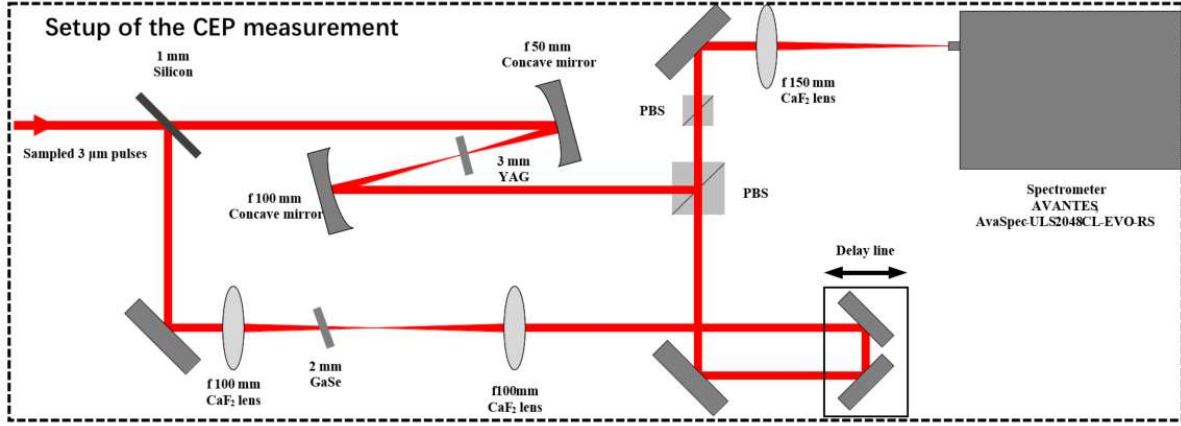
Figure 3.8 The setup for CEP measurement.

As discussed in Section 3.1, a stable CEP is desired for our 3 μm OPCPA system. The CEP stability is measured using an f-3f spectral interferometer. The setup is shown in Figure 3.8. The 3 μm beam is split into two arms (transmitted and reflected) by a 1-mm thick Si wafer serving as a beam splitter. The pulses in the transmitted arm are focused into a 3-mm thick uncoated YAG plate using a concave mirror with an effective focal length of 50 mm to generate SC covering the third-harmonic frequency (~1 μm), through single filamentation. The 3 μm pulses in the reflected arm are focused into a 2-mm thick GaSe crystal placed at Type-I phase-matching angle, which generates the third harmonic pulses at ~1 μm. The SC and the third-harmonic pulses with the orthogonal polarizations are combined using a polarizing beam splitter (PBS), and they interfere with each other at ~1000 nm wavelength. The interference spectrum is recorded using a near-infrared spectrometer equipped with a fast detector (AVANTES, AvaSpec-ULS2048-EVO-RS). The spectrometer is set to an integration time of 10 μs. The visibility of the spectral fringes is optimized with another PBS, and a typical interference spectrum is shown in Figure 3.9(b). An interferogram as plotted in Figure 3.9(a) is acquired over 100 s. The extracted CEP fluctuations as a function of time are shown in Figure 3.9(c), and its RMS value is measured to be 391 mrad over a100 s time period.
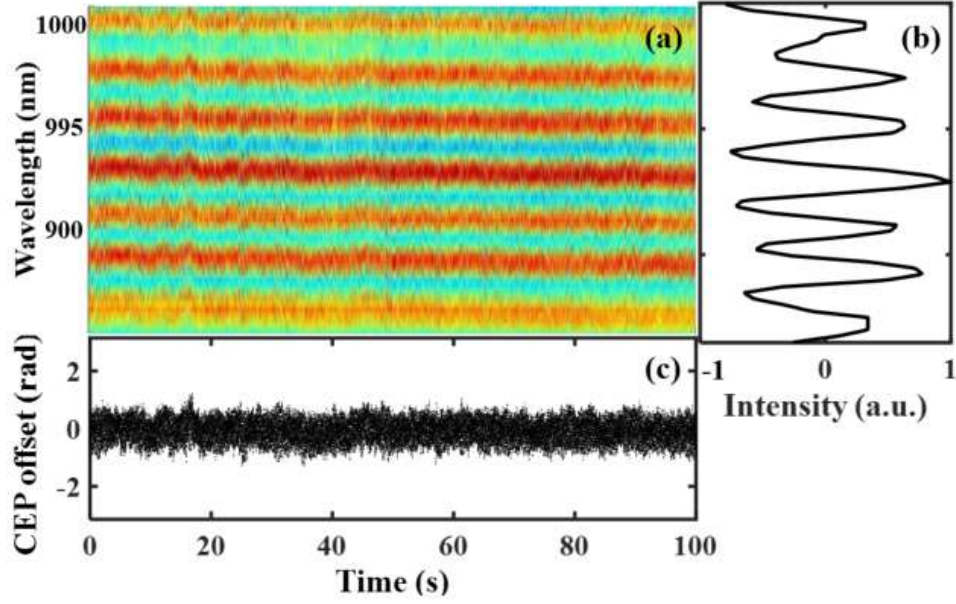
Figure 3.9 (a) Interferogram over 100 s based on the f-3f measurement, (b) typical interference spectrum, and (c) measured CEP fluctuation indicating an RMS value of 391 mrad over 100 s period.

3.5 Nonlinear pulse compression and high harmonic generation

Due to the limited amplification bandwidth of our OPCPA system, it cannot directly output sub-two-cycle or even single-cycle pulses which are required by some strong-field applications such as isolated attosecond pulse generation. However, the nonlinear pulse compression technique based on the nonlinear spectral broadening via SPM [100] and either subsequent [110, 112] or simultaneous dispersion compensation [77, 111, 113] can further shorten the pulse width of such high-energy pulses with a low loss. The nonlinear media for the spectral broadening may be gases or bulk materials. For example, gas-filled waveguides have been used for multi-mJ, sub-two-cycle pulse generation [110, 111] and high-energy single-cycle pulse generation [77]. Direct nonlinear pulse compression in air without the use of waveguides was demonstrated for tens of mJ, 35 fs pulse generation [71]. In recent years, solids as nonlinear media are also thriving for the high-energy nonlinear pulse compression with the low loss. While filamentation in solids can broaden the spectra largely, as discussed in Section 3.1, it causes the large loss due to multiphoton excitation and ionization [99], especially for high-energy femtosecond or picosecond pulses. In order to avoid the large loss, filamentation-free is needed for the high-energy pulses. This can be achieved by using thin solids to minimize the self-focusing-the beams exits solids before

37

filamentation. In the near-infrared region, a single-cycle pulse compression with a pulse energy of up to 0.4 mJ using multiple thin fused silica plates was demonstrated [112]. In the mid-IR region, using a single YAG plate as a nonlinear medium, the 21 mJ, mid-IR pulses are compressed to 30 fs from 94 fs with only slight ionization loss found [113].
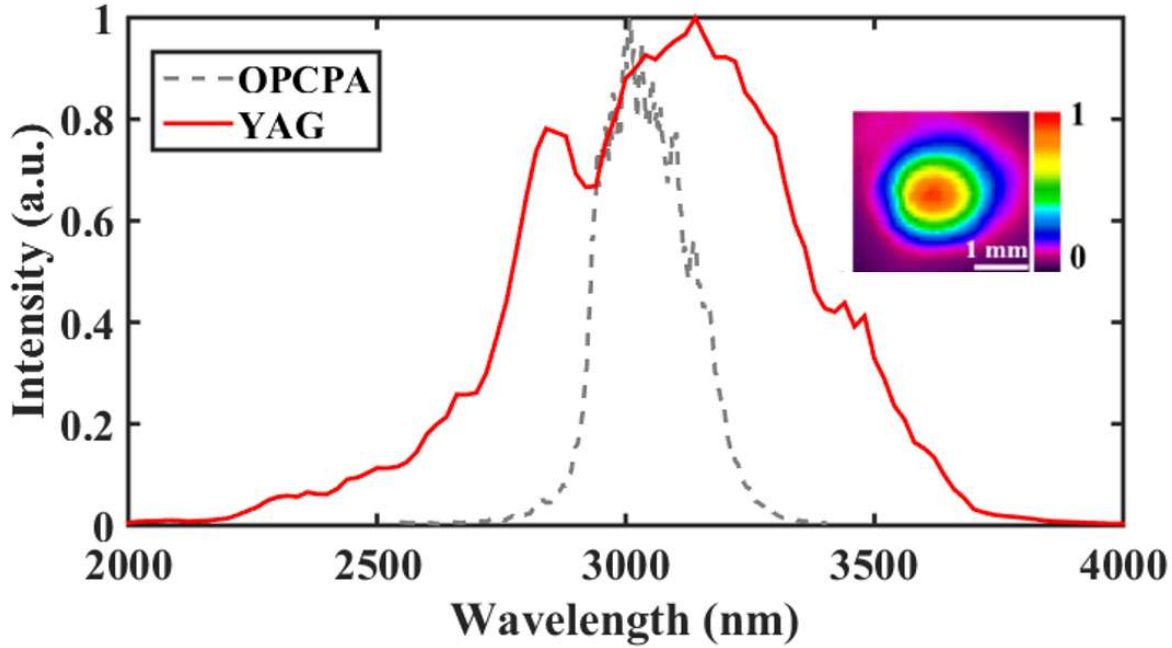
Figure 3.10 The spectrum of nonlinearly compressed pulses from YAG with a comparison of that from OPCPA.

To pursue shorter pulse width, the nonlinear pulse compression of the 3 μm pulses from the OPCPA system is investigated using a 2-mm thick uncoated YAG plate in our experiment. YAG is chosen for its high third-order nonlinearity and good mechanical properties. The setup for nonlinear pulse compression is shown in Figure 3.3, in which an AR-coated CaF_2 lens with a focal length of 75 mm is used to focus the 3 W, 300 μJ, 61fs , 3 μm pulses to the YAG plate which is placed slightly after the focal spot to avoid the crystal damage and the obvious ionization. By optimizing the position of YAG from the focal spot, a symmetrically broadened spectrum spanning from 2160 nm to 3840 nm are obtained due to SPM, as show in Figure 3.10, which supports 18 fs TL pulse width. ~255 μJ pulse energy is measured after the YAG without the degradation of beam profile (the inset of Figure 3.10). It is worth mentioning that ~15% energy loss is mainly from the Fresnel reflection on the uncoated surfaces of YAG. Because the positive second-order dispersion arising from SPM is counteracted by the negative second-order dispersion of YAG, the pulses are

thus self-compressed. The temporal profile of the 3 μm nonlinearly compressed pulses measured using SHG-FROG is shown in Figure 3.11. 21 fs pulse width is obtained, which corresponds to two-cycle pulse width centered at 3 μm.
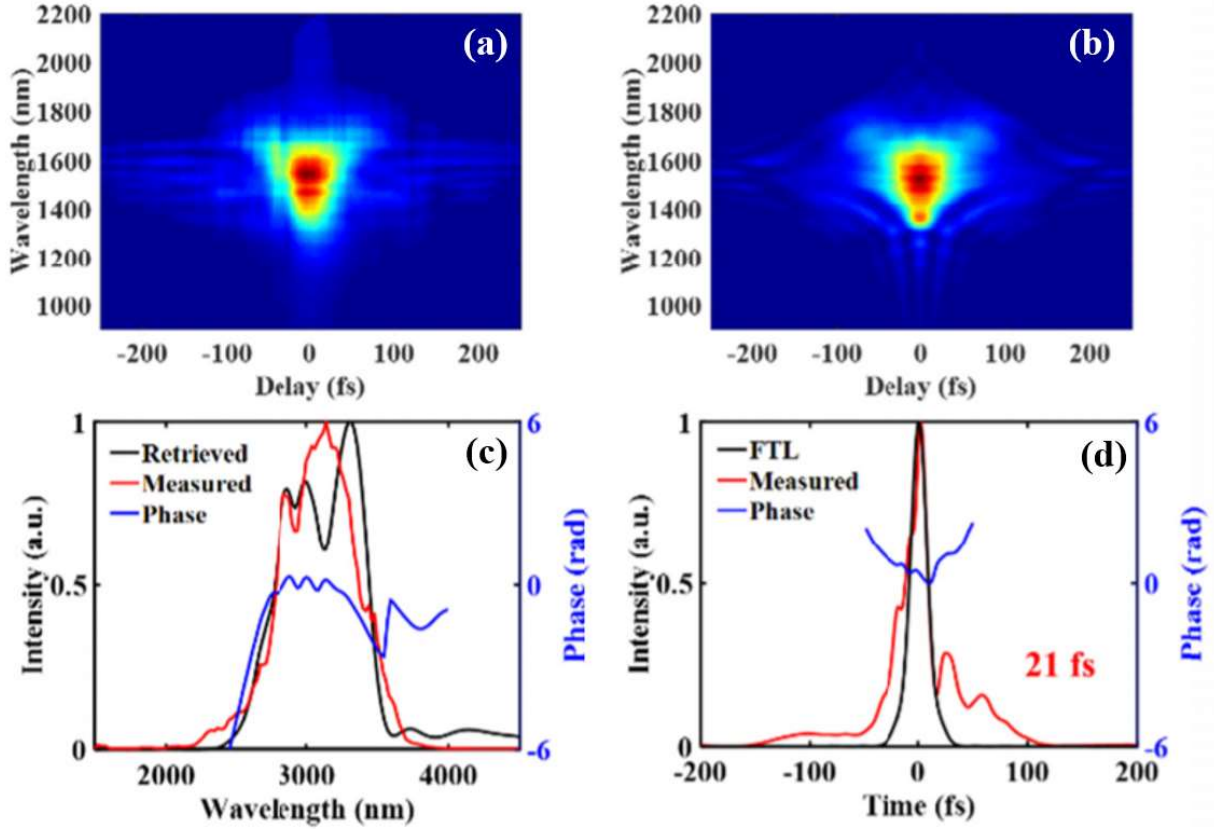
Figure 3.11 FROG measurement at the output of the nonlinear compressor. Measured (a) and retrieved (b) FROG traces. (c) Measured and retrieved spectra. (d) Measured and retrieved temporal profiles of the 3 μm pulses. The Frog error is 0.8% with a free frequency marginal.

Next, we explore the HHG in a ZnO crystal (1120 cut) using high-energy, high-power, few-cycle, 3 μm pulses before and after nonlinear pulse compression, respectively. The HHG mechanism in solid materials can be obtained in [114]. In the process of HHG in solids, electrons from the valence band are first excited to the conduction band through tunneling ionization and then they are accelerated by the laser field and acquire the kinetic energy. The accelerated electrons could return to the valence band and recombine with the parent ions. During the recombination, the high harmonics are emitted. There is also another case which is different from HHG in gases, the accelerated electrons do not return to the valence band but form the intra-band current in the

conduction band. The intra-band current source also makes contribution to high harmonics through Bloch oscillation process [115, 116]. The cut-off energy of HHG in solids linearly scales with the wavelength of the driving pulses [17]. The research on HHG in solids has been demonstrated in different materials, such as GaSe [34], MoS_2 [117], glass [118], Si [119], ZnO [120], MgO [121] and Sapphire [122]. The ZnO crystal is chosen in our experiment for its large bandgap energy of 3.3 eV (376 nm in wavelength) and larger nonlinearity (χ_{1111} =1.32 × 10^{-13} cm^3 erg) compared to the other solid materials. To avoid filamentation generation, the ZnO with a 0.5 mm thickness is used and the setup for HHG is depicted in Figure 3.3.
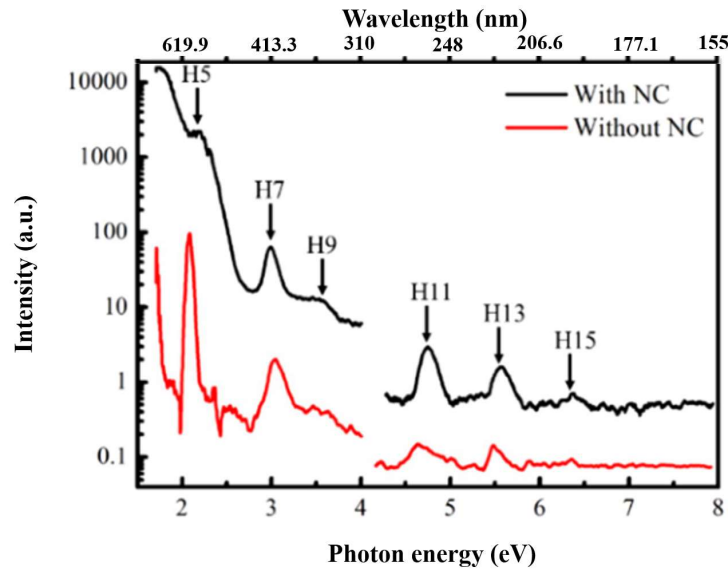
Figure 3. 12 Measured HHG spectra driven by the 3 μm pulses before (red curve) and after (black curve) nonlinear pulse compression. The HHG spectra measured by different spectrometers are calibrated and stitched. The discontinuity at ~4 eV is due to the lack of measured spectra at the edge of the spectrometer.

We use 3 μm pulses before and after nonlinear compression as the drivers and the energies are both attenuated to 120 μJ with an iris. Then they are focused to the ZnO crystal using an AR-coated CaF_2 lens with a focus length of 150 mm. The estimated vacuum intensities on ZnO are 4.4 TW/cm^2 and 1.3 TW/cm^2, corresponding to field intensities of 0.42 V/Å and 0.23 V/Å for the 3 μm pulses before and after nonlinear compression, respectively. Under the pump intensities, stable concentric circles with visible colors are observed after ZnO for both cases. To avoid the disturbance of the strong fundamental 3 μm pulses, the HHG spectra from the backside reflection of ZnO are characterized using two different Ocean Optics spectrometers (HR 2000+ and Maya

2000 Pro). The measured HHG spectra using 3 μm pulses before and after nonlinear pulse compression are plotted in Figure 3.12. It is found that the odd harmonics up to the 15th order, which is well beyond the bandgap energy, are clearly seen in both HHG spectra. The HHG intensity obtained with nonlinearly compressed pulses is one order of magnitude higher than that using pulses before nonlinear pulse compression, which is attributed to the enhancement of pump intensity. The harmonics energy generated by 3 μm, 21 fs pulses is measured as 1.6 μJ after a 1300 nm short-pass filter, which corresponds to 1.3% conversion efficiency for the third-order and above harmonics. It is worth mentioning that the HHG spectra could be used to probe crystal band structures [123] and image the charge dynamics in solids [124].

3.6 Conclusions

A CEP-stable, 3 μm OPCPA system is designed and developed, in which the PPSLT crystals with the good phase-matching bandwidth and the large damage threshold are used as the nonlinear crystals. To the best of our knowledge, this is the first time that PPSLT is used as nonlinear crystals in a ~3 μm OPCPA system. The demonstrated OPCPA delivers pulses with a 3 W average power, a 300 μJ pulse energy and 61 fs pulse width at a10 kHz repetition rate. This verifies the potential of PPLST crystals for high-power, high-energy, few-cycle, 3 μm OPCPA systems. To pursue shorter pulse width, nonlinear pulse compressor based on a 2 mm thick YAG crystal is also developed and the 3 μm pulses are compressed to 21 fs (two cycles) with a 255 μJ pulse energy. The nonlinear compressor cut in Brewster angle would further enhance efficiency. Using those pulses, we also generate a broadband HHG spectrum with up to the 15th order in a 0.5 mm thick ZnO crystal. Compared with HHG driven by 3 μm pulses before the nonlinear pulse compression, one order of magnitude enhancement of the harmonic intensity is demonstrated, revealing the significance of the intensity enhancement of the driving source.

Chapter 4 Mid-IR IPDFG assisted by SPM

The IPDFG as a simpler technique, which does not require the precise control of the cavity length in the OPO or delay stages in the OPA, OPCPA and the DFG, emerges recently for long-wavelength mid-IR pulse generation. Benefitting from the progress of the broadband few-cycle driving lasers centered at 1 μm [125, 126], 1.5 μm [127], 2 μm [68, 69, 128, 129], 2.3 μm [130], and 2.5 μm [131], broadband mid-IR IPDFG sources have been demonstrated with 4-20 μm spectral coverage [69], watt-scale output power [68, 129] and sub-two-cycle pulse width [68, 125]. At present, high-power, high-energy, few-cycle, ~3 μm sources based on OPCPA are becoming available [77, 78]. For example, U. Elu et al. demonstrated the generation of 21 W, 97 fs, 3.25 μm pulses from a $KNbO_3$-based OPCPA system, and the generation of 9.6 W, 14.5 fs self-compressed pulses with a gas-filled hollow-core fiber as the nonlinear pulse compression stage in 2017 [77]. Later, M. Mero et al. reported a KTA-based OPCPA system delivering 3.1 μm, 12.5 W, 73 fs pulses [78]. It is thus worth exploring broadband mid-IR pulse generation via IPDFG pumped by the 3 μm driving sources for several potential benefits, such as the smaller nonlinear absorption for the narrow-bandgap nonlinear crystals and the potential high conversion efficiency due to the reduced quantum defect between the driving wavelength and IPDFG wavelength. The difficulty in the IPDFG driven by 3 μm sources is the generation of the short mid-IR wavelengths which highly depends on the spectral span of the driving sources. Assuming driven by 3 μm, 60 fs Gaussian pulses, the calculated shortest mid-IR wavelength generated in the IPDFG is 12 μm which largely limits the bandwidth of the generated IPDFG pulses. The access to the shorter mid-IR wavelengths via IPDFG directly pumped by the 3 μm, 60 fs OPCPA thus seems impossible, due to the absence of the necessary spectral components in the driving pulses. The extra nonlinear compression to obtain a broader pumping bandwidth could be adopted, as in the IPDFG systems driven at 1 μm [125, 126] and 2 μm [68, 129] wavelengths. On the other hand, some works suggest that the ultra-broadband IPDFG could be achieved by making use of the SPM effect in the IPDFG crystals [126, 128] or via cascade parametric conversions [130].

In this chapter, driven by a 3 μm, 65 fs, 10 kHz pulses from our OPCPA system, we report a broadband, > 6 μm, mid-IR IPDFG assisted by SPM in a GaSe crystal. The IPDFG pulses with a 7-15 μm spectral coverage, a 0.91 μJ pulse energy, and 9.1 mW output power are generated. The

contribution of the driving pulse spectral broadening via SPM in the process of IPDFG is confirmed experimentally. A home-made interferometric autocorrelator (IAC) reveals that the generated IPDFG pulse can be compressed to 60 fs pulse width corresponding to 1.8 cycles by adding extra bulk materials. The good compressibility of the IPDFG pulses verifies the good spectral coherence of the IPDFG pulses. The results of this chapter have been published in [132].

4.1 Nonlinear crystals for long-wavelength mid-IR

Table 4.1 The specifications of non-oxide nonlinear crystals.

Non-oxide crystals	Transmission range (μm) [133, 134]	Bandgap (eV) [133, 134]	n_2 (10^{-16}cm^2/W at λ)	Damage threshold (GW/cm^2 @ λ, τ)
AgGaS$_2$(AGS)	0.5-13	2.70	150 @ 4.6 μm [135]	0.6-0.7@1.06μm, 35 ps [138]
AgGaSe$_2$(AGSe)	0.7-18	1.8	350 @ 1.5 μm[136]	>200 @ 2.1 μm, 26fs [128]
ZnGeP$_2$(ZGP)	2.0-11	2.34	400 @ 2.1 μm [134]	0.086 @ 2.1 μm, 21 ns [139]
GaSe	0.65-18	2.1	450 @ 1.06 μm [134]	1700 @ 1.9 μm, 16fs [129]
GaP	0.54-10.5	2.26	200 @ 0.78 μm [134]	70.5 @ 1.04 μm, 61fs [140]
CdSiP$_2$(CSP)	0.5-9	2.45	-	0.086 @ 2.1 μm, 21 ns [139]
LiGaS$_2$(LGS)	0.3-11	3.76	41 @ 1.03 μm [137]	0.24 @ 1.06 μm, 14 ns [141]
LiGaSe$_2$(LGSe)	0.4-13	3.65	-	<0.24 @ 1.06 μm, 14 ns [141]

Due to the intrinsic absorption of oxide-crystals, they are not suitable for the generation of ultrafast mid-IR pulses at the wavelength of >5 μm. In this case, the extension of operating wavelengths for optical parametric systems is satisfied by the new generation of non-oxide crystals capable of providing the optical transparency of beyond 5 μm, such as AgGaSe$_2$(AGSe) , ZnGeP$_2$(ZGP),GaSe,GaP, CdSiP$_2$ (CSP), LiGaS$_2$(LGS) and LiGaSe$_2$(LGSe).Table 4.1 shows the specifications of corresponding mid-IR crystals, in which the transmission ranges and bandgaps

are from [133,134], the nonlinear refractive indices (n_2) are from [134-137] and the damage thresholds are from [128, 129, 138-141]. Here, we give a simple overview about non-oxide crystals for the long-wavelength mid-infrared pulse generation.

AGS [142, 143], CSP [66], GaP and ZGP [72, 73] have been employed to extend high-energy few-cycle pulses to the wavelength range of 4-12 μm. 8.5 μm, 150 μJ, few-cycle pulses were demonstrated by mixing the 1.8 μm pump and the 2.4 μm signal in an AGS-based DFG system [142]. 33 μJ, 0.88-cycle pulses covering 2.5-10 μm spectral range were generated by coherent synthesis of signal and idler pulses of a CSP OPA, pumped by a 2 μm OPCPA [66]. Using 1.5 μm Er-doped fiber laser as pump, IPDFG based on orientation patterned (OP)-GaP output a 4-12 μm spectrum [127]. The energies of a few-cycle ZGP-based OPCPA system at a central wavelength of 5 and 7 μm were boosted to 1. 0 and 0.7 mJ, respectively, with powerful 2 μm solid-state lasers as pumping [72, 73]. Recently, the wide bandgap nonlinear crystal LGS has emerged. 7-11 μm few-cycle, or even single-cycle pulses with nano-joule-level pulse energy have been demonstrated in OPA and IPDFG configurations based on LGS crystals and pumped at the near-IR wavelength [125, 126, 144, 145]. Subsequently, up to 14 μJ few-cycle pulses centered at 9 μm were obtained in an LGS-based OPCPA system [146]. To pursue longer wavelength up to 20 μm, AGSe [128, 147] and GaSe [67-69] nonlinear crystals have been employed in the DFG or IPDFG configuration, thanks to their longer transparent cutoff wavelength. Especially, GaSe was demonstrated for broadband, single-cycle mid-IR pulse generation with a spectral coverage from 4 to 300 μm [67-69]. In order to avoid parasitic two- or three-photon absorption, AGSe and GaSe should ideally be pumped at > 2 μm wavelength. Without doubt, 3 μm driving sources potentially mitigate the nonlinear absorption.

Figure 4.1 depicts the phase-matching curves ($\Delta k = 0$) of AGSe and GaSe for 3 μm pump [101]. We can see that both crystals have phase-matching for Type-I and Type-II. The phase-matching angle of AGSe changes from 39.8° to 47.8° for 6-16 μm wavelength with an angle change of 8° for Type-I and changes from 51.7° to 67.1° for 6-16 μm wavelength with an angle change of 15.4° for Type-II. GaSe satisfies the phase-matching in the same wavelength ranges with only 2° angle change from 10.6° to 12.6° for Type-I and 1.8° angle change from 13.2° to 15° for Type-II. Whether Type-I phase-matching or Type-II phase-matching for GaSe is better than that of AGSe. Beside the better phase-matching, Gase has also higher nonlinear coefficients (55 pm/V for Type-

I, 53 pm/V for Type-II from SNLO [101]), higher damage threshold ($\sim 1.7\ \text{TW/cm}^2$ [129]) and higher nonlinear refractive index ($450 \times 10^{-16}\ \text{cm}^2/\text{W}$ [134]). Nonlinear refractive index is considered as an important assessment parameter for the crystal selection, because SPM makes contributions for IPDFG in nonlinear crystals with the high nonlinear refractive index. For the aforementioned reasons, GaSe is chosen as the nonlinear crystal for 3 μm-pumped IPDFG.
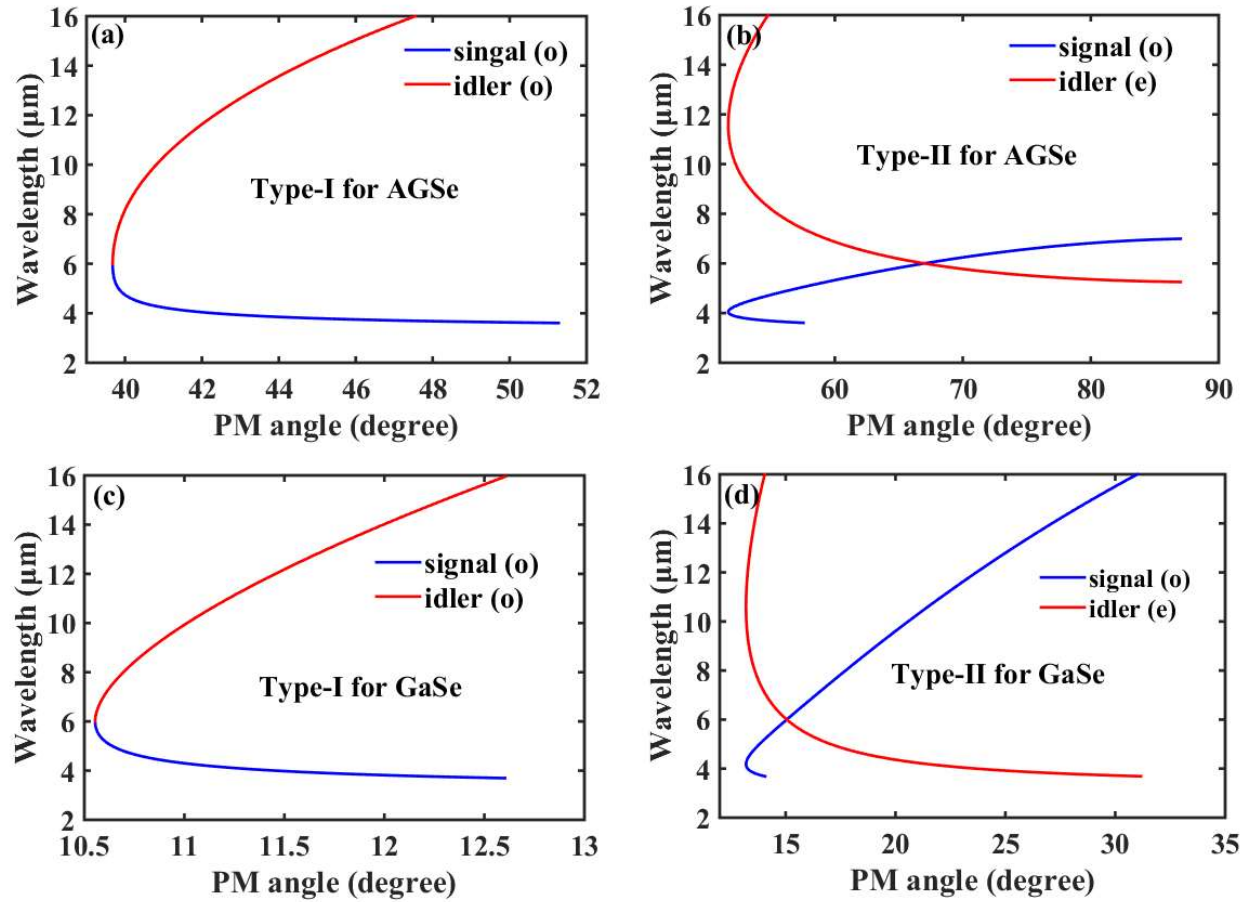
Figure 4.1 The calculated phase-matching curves of AGSe for Type-I (a) and Type-II (b) and the calculated phase-matching curves of GaSe for Type-I (c) and Type-II (d), using SNLO. All calculations use 3000 nm as pump wavelength.

In Chapter 2, we introduce the phase-matching bandwidth is related to the crystal thickness. Here, we plot, in the Figure 4.2, the phase-matching function $|\text{sinc}(\Delta kL/2)|$ with respect to the phase-matching angle and the phase-matching wavelength, in a GaSe crystal (L = 2 mm) and a 3 μm pump wavelength for the Type-I and Type-II. It is found that when the phase-matching function

|sinc(ΔkL/2)| for Type-II is maximized, as indicated by the black dashed curve in Figure 4.2(b), the group velocity of the signal (4204 nm, o-wave) and the idler (10475 nm, e-wave) which are shown as the two stationary points marked by the arrows match at the phase-matching angle of $13.2°$. For better understanding, please also see the Section 2.1.2 in Chapter 2, where the equation (2.19) about bandwidth shows when the group velocity of signal equals that of idler, a maximum bandwidth is given. Thus, Type-II is chosen in our experiment due to the maximized phase-matching bandwidth [67].
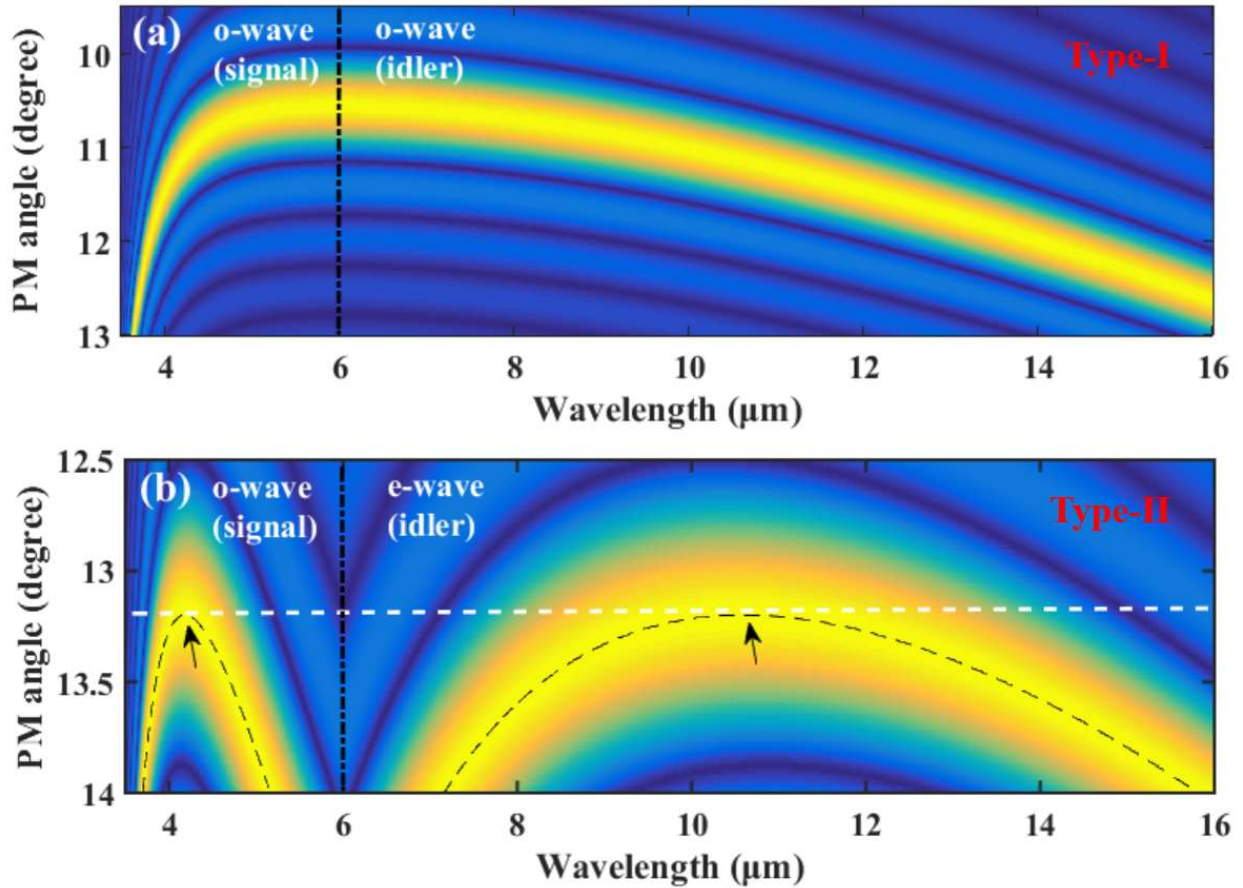
Figure 4.2 (a) The PM function |sinc(ΔkL/2)| with respect to the PM angle and the PM wavelength, in a GaSe crystal (L = 2 mm) for the Type-I (a) Type-II (b) using a 3 μm pump wavelength.

4.2 Experimental setups

The schematic of the 3 μm driving source is shown in Figure 4.3(a), which is a four-stage OPCPA system, including a SCG stage in YAG, two-stage MgO: PPLN-based amplifiers and two-stage

PPSLT-based amplifiers. The OPCPA is driven by a 1030 nm, 1 ps, 10 kHz Innoslab laser with a maximum output energy of 12 mJ. The pump energy is split into 80 μJ for SCG, 350 μJ for the first OPA stage, 0.8 mJ for the second OPA stage, 5 mJ and 5 mJ for the third and the fourth OPA stages. PPSLT crystals with a large damage threshold of > 80 GW/cm^2 and the good phase-matching bandwidth at 3 μm [102] are adopted for the last two stage OPAs, to achieve the high pulse energy and the large amplification bandwidth simultaneously. A maximum pulse energy of ~300 μJ at 3 μm is delivered. The other details about the 3 μm OPCPA could be found in Chapter 3. The temporal profile of the 3 μm pulses after the compressor is characterized using a commercial SHG-FROG, as shown in Figure 4.4. 65 fs pulse width is measured with a FROG error of ~0.7% and a free frequency marginal, which corresponds to 1.08 times TL pulse duration. Note that the spectrum and pulse duration of 3μm pulses are slightly different from that in Chapter 3. That may be caused by the alignment for the last-two stages of our OPCPA system and the settings of AOPDF.
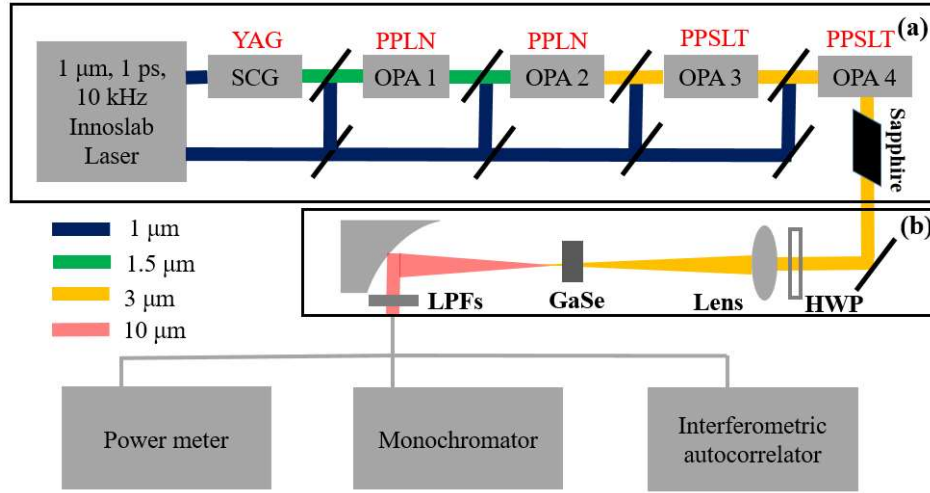
Figure 4.3 The schematic of the experimental setup. (a) The 3 μm OPCPA system based on PPLN and PPSLT crystals. The stretchers consisting of the bulk silicon and an AOPDF are not shown in the schematic. The Sapphire block serves as a compressor. (b) The stage of the mid-IR IPDFG.

The IPDFG stage in Figure 4.3(b) consists of an HWP working at 3 μm, an AR-coated CaF_2 lens with 350-mm focal length and a 2-mm thick uncoated GaSe crystal. The 140 μJ, 3 μm pulses are used to drive the IPDFG stage. As the GaSe is in z-cut orientation ($\theta = 0°$), an external angle of 38.4° corresponding to the internal phase-matching angle of 13.2° is chosen, which results in a

Fresnel reflectance loss of ~14%. Thus, 120 μJ driving pulses enters the crystal. The energy of the 3 μm driving pulses is distributed onto the o-axis and the e-axis of the GaSe crystal by rotating the HWP. The short-wavelength spectral components of the e-wave (p-polarized), and the long-wavelength spectral components of the o-wave (s-polarized) from the same driving pulses are mixed, serving as the pump and signal pulses, respectively. The e-wave IPDFG output as the idler is generated. The generated IPDFG beam is collimated by a gold-coated 90° off-axis parabolic mirror with an effective focal length of 101 mm, and then separated from the residual pump using LPFs with different cut-off wavelengths. A series of characterizations for IPDFG pulses are accomplished by the power meter, the monochromator with a liquid-nitrogen-cooled HgCdTe (MCT) detector, the mid-IR beam profiler and a home-built IAC.
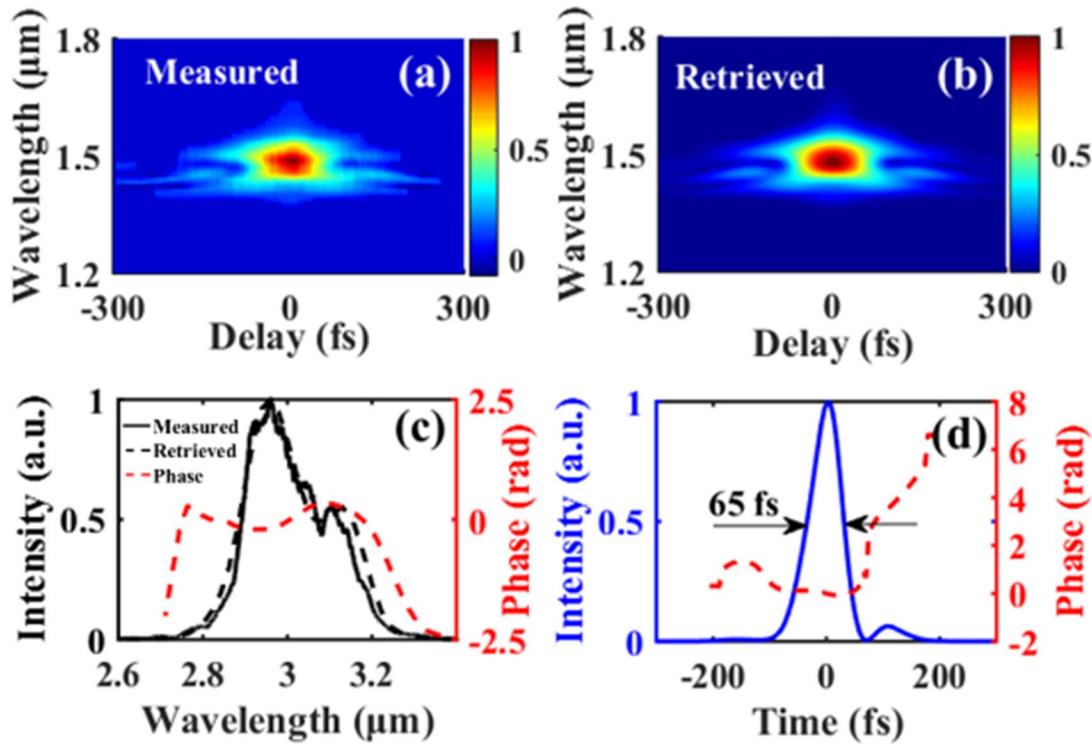
Figure 4.4 Characterization of the 3 μm driving pulses. The measured (a) and retrieved (b) FROG traces. (c) The measured spectrum, the retrieved spectrum and the retrieved phase. (d) The retrieved temporal profile and the spectral phase. The Frog error is 0.7% with a free frequency marginal.

4.3 IPDFG output energy and spectrum

At the beginning, a 1-mm-thick GaSe crystal is firstly used and it is placed at a position where the peak intensity on the GaSe is ~1.5 TW/cm^2. By rotating the HWP and the phase-matching angle, the maximum output energy behind 7.3 μm LPF is only ~100 nJ. The crystal thickness limits the conversion efficiency. Subsequently, a 2-mm-thick GaSe crystal is placed on the same position. The IPDFG output energy is boosted to 1.4 μJ. Taking into account the losses from the LPF (10%) and the parabolic mirror (6%), a 1.63 μJ pulse energy (16.3 mW average power) is obtained after the output surface of the crystal, which corresponds to an internal conversion efficiency of 1.6% (taking into account the surface reflection losses of GaSe). However, slight damage on the crystal surface is observed after half an hour operation. In order to avoid damage, the crystal is placed at a safe position with a peak intensity of ~0.9 TW/cm^2, corresponding to an internal intensity of 0.77 TW/cm^2. At this position, a systematic investigation is executed, which is introduced as follows.
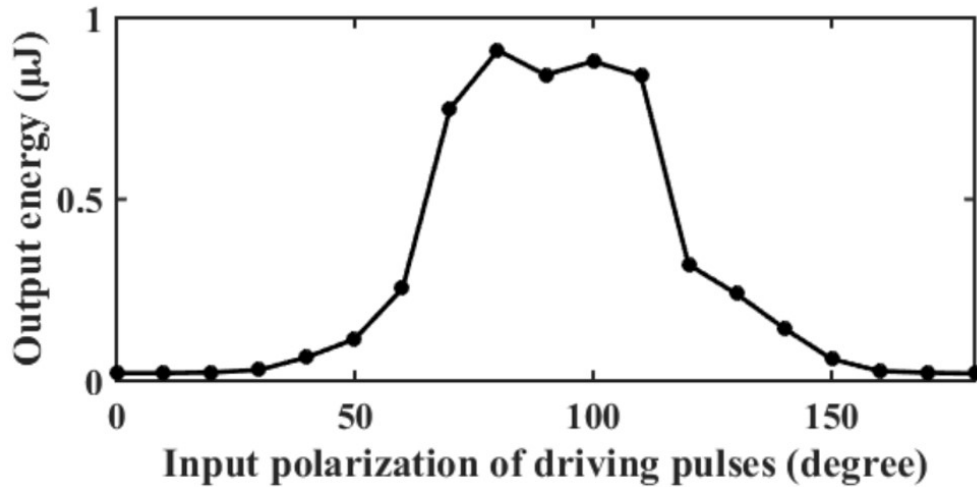
Figure 4.5 The IPDFG output energy after 7.3 μm LPF with the input polarization of driving pulses.
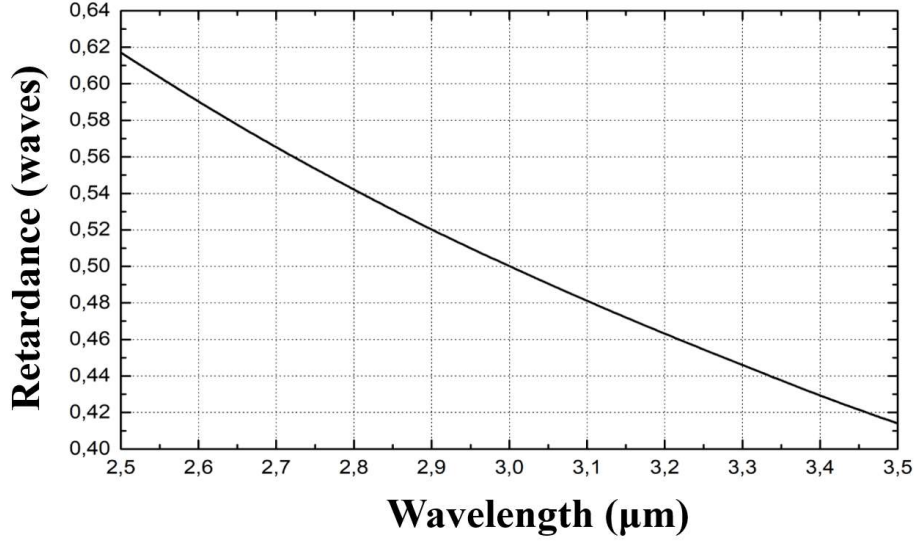
Figure 4.6 The retardance curve of HWP at 3000 nm.

The IPDFG output is optimized through rotating the HWP and the crystal angle ($\varphi = 0^{\circ}, \theta = 13.2^{\circ}$). Figure 4.5 shows the IPDFG output energy after the 7.3 µm LPF as a function of the input polarization of the driving pulses. A maximum output energy of 0.91 µJ is obtained when the input polarization is rotated by $\sim 80^{\circ}$, which indicates the major energy of the driving pulses is used to serve as the pump part in IPDFG similar to the OPA process. Taking into account the losses from the LPF, the parabolic mirror and the surface reflection of GaSe, the internal conversion efficiency is 1.02%. It should be noted in Figure 4.5 that there are still some IPDFG outputs when the polarization is rotated by $\sim 0^{\circ}$ and $\sim 180^{\circ}$. However, when we rotate polarization of driving pulses at o-axis or o-axis using the HWP, theoretically all energy should be along the o-axis or e-axis. A zero IPDFG output should be found. The non-zero IPDFG output can be attributed to the imperfect retardation of HWP outside the wavelength of 3000 nm, as shown in Figure 4.6, it is obvious that the HWP only provide 0.5λ retardance at 3000 nm. Because the driving pulses have a broad spectral coverage, some polarization leakage into another axis always occurs in the spectral range beside 3000 nm. Due to the large gain of OPA (see the Section 2.1.1 in Chapter 2), the small leakage of energy in another axis brings a significant impact on the output energy. The IPDFG output fluctuation for a period of 1 hour at 0.91 µJ is measured as $\sim 1.3\%$ rms as shown in Figure 4.7. The inset of Figure 4.7 shows the IPDFG pulses has also a good beam profile.
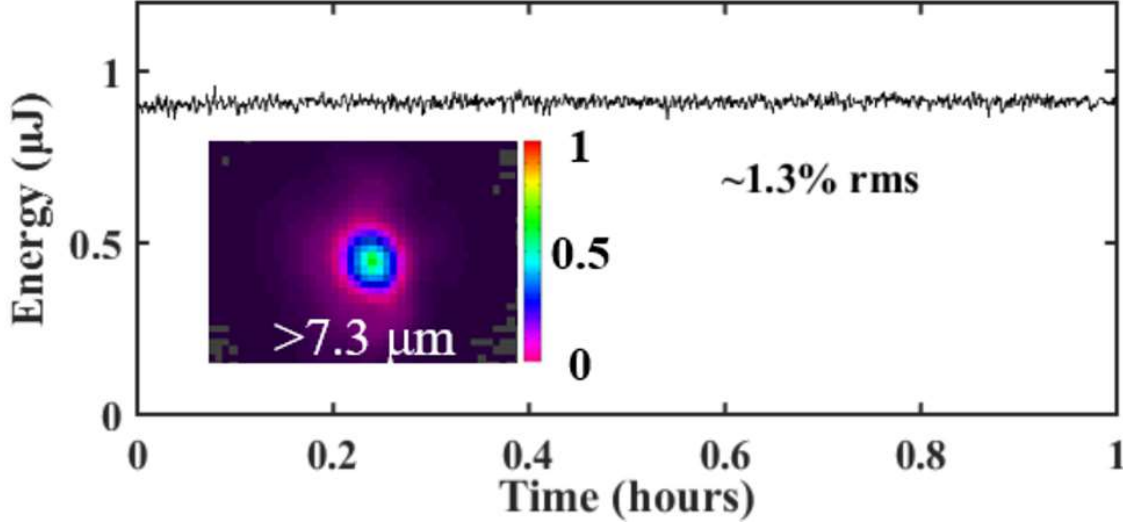
Figure 4.7 The one-hour energy stability of the IPDFG pulses, measured behind the 7.3 µm LPF. The inset shows the measured IPDFG beam profile.

The measured IPDFG spectrum at maximum output energy is depicted in Figure 4.8(b), which spans from 7 to 15 µm and agrees well with the prediction of the PM function in Fig. 4.8(a). Note that the Figure 4.8(a) is same as the Figure 4.2(b). For the clear comparison with the IPDFG spectrum, it is plot again as Figure 4.8(a). Those spectral components of 3.6 - 5.3 µm (measured behind a 3.6 µm LPF), functioning as the signal in the IPDFG process is also identified in Figure 4.8(b), which, however, are obviously missing in the driving pulses, as shown in Figure 4.4(c). Considering the large nonlinear refractive index of the GaSe crystal and the high pump intensity, the SPM caused spectral broadening is considered as the origin of these extra spectral components. The origin of such signal spectral components could be confirmed in future systematic studies.
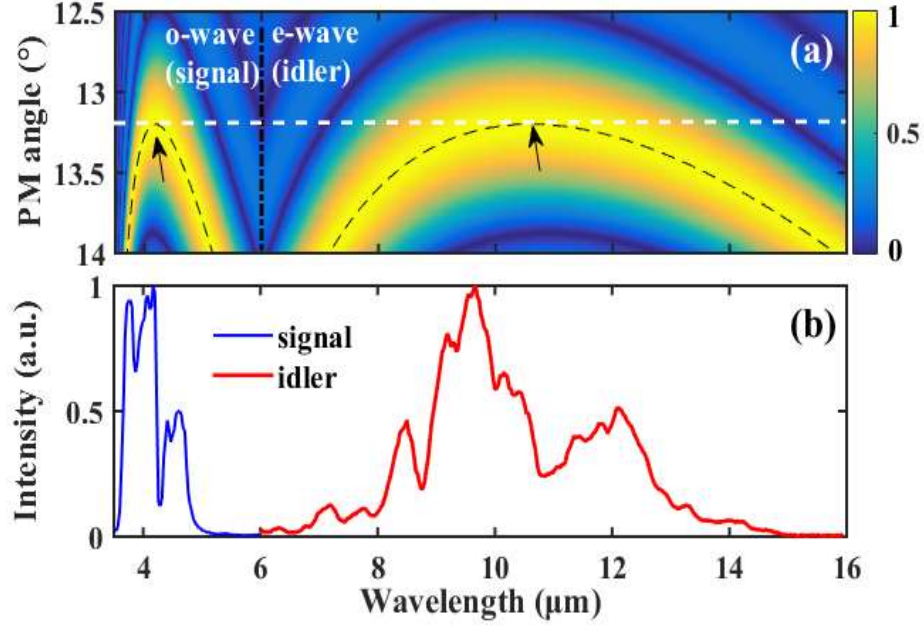
Figure 4.8 (a) The PM function |sinc($\Delta k L/2$)| with respect to the PM angle and the PM wavelength, in a GaSe crystal (L = 2 mm) for the Type-II PM and a 3 μm pump wavelength. The two stationary points marked by the black arrows represent the signal and idler with the matched group velocity, when the PM function is maximized. (b) The measured mid-IR spectrum of > 3.6 μm at the PM angle of ~13.2°. The spectra of signal and idler are normalized, respectively.

4.4 SPM effect in IPDFG

To study the contribution of the SPM effect in GaSe to the 3.6-5.3 μm signal generation, a setup as shown in the inset of Figure 4.9 is developed, which consists of a 300-μm thick Si plate placed at a Brewster angle of 73.8° with respect to the 3 μm wavelength. The reflection coefficients of Si for the s-polarized and the p-polarized light in the wavelength range of 2.5-16 μm are plotted in Figure 4.9. It has a reflection coefficient of $< 10^{-5}$ and ~71% for the p-polarized and s-polarized light, respectively. It is also worth mentioning that the reflection coefficient for the s-polarized mid-IR radiation is quite flat and smooth in the spectral range of 2.5-16 μm with only 0.18% fluctuation between the maximum (2.5 μm, 71.22%) and minimum (16 μm, 71.04%). This enables the s-polarized light to be almost completely separated from the p-polarized light without shaping the spectrum.
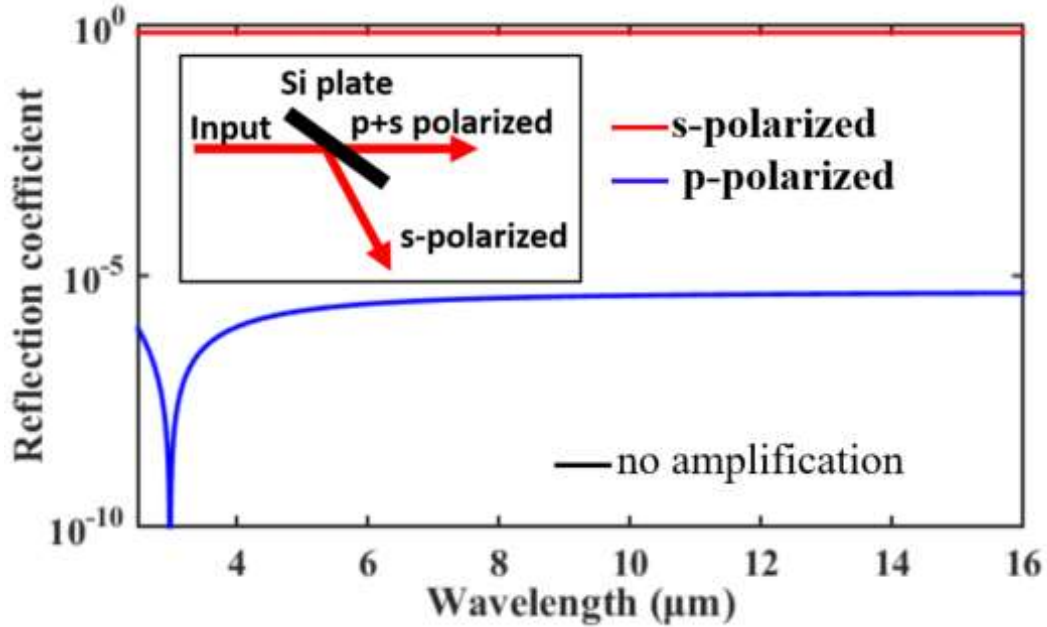
Figure 4.9 The reflection coefficient of the Si plate placed at Brewster angle with respect to the 3 μm wavelength. The inset shows the corresponding setup to separate the s and p polarized pulses.

With the help of this setup, the spectral broadening of the s-polarized signal and the p-polarized pump via SPM is measured independently. In the first step, at the phase-matching condition ($\varphi = 0°, \theta = 13.2°$), the spectrum of the reflected mid-IR output which corresponds to the amplified signal in the s polarization is measured as the blue curve in Fig. 4.10(a). The spectrum spanning in the range of 3.6 - 5.3 μm is manifested. The 7 - 15 μm spectral components are not found in the measured signal spectrum, which confirms the p-polarized spectral components (including pump and idler) are isolated well. The signal without amplification is then measured by rotating the azimuthal angle (φ) of GaSe by 90°, which makes the effective nonlinear coefficient ~0 pm/V, and fully suppresses the amplification in IPDFG. As shown in the measured spectrum (the red curve) in Figure 4.10(a), it is found that the signal without amplification is well extended to cover the wavelength range of 3.6 - 5.3 μm by SPM, and its spectral shape and components are very similar to the one after amplification. Therefore, it is confirmed that the SPM which causes the spectral broadening of the signal plays a crucial role in seeding the IPDFG process. Besides the signal, the spectral broadening of the pump needs to be considered as well. Figure 4.10(b) shows the spectrum of the pump after the GaSe without the amplification. It is clear that there is substantial spectral blue-shift to <2.7 μm wavelength which is uncovered by the spectrum of the

original driving pulses. It is worth mentioning that the contribution of the blue-shifted spectral components to the IPDFG is non-negligible. For example, the new pump spectral component at 2.5 μm have a good phase-matching at the same phase-matching angle of 13.2°, as shown in the inset of Figure 4.10(b), which makes contribution to the generation of 7-9 μm spectral components. Thus, we suggest that the ultra-broadband IPDFG is a combination effect of the spectral red-shift of the signal and the blue-shift of the pump in a nonlinear crystal with the large nonlinear refractive index.
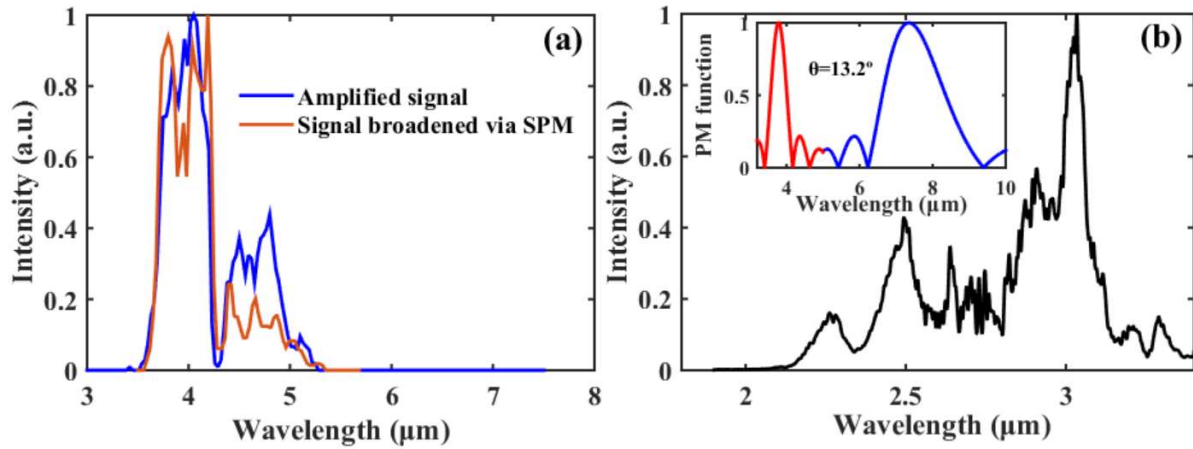
Figure 4.10 The spectra of the signal with and without amplification, measured via the setup in the inset of Figure 4.9. (b) The spectrum of the pump after the GaSe crystal without amplification. Inset: The PM function $|\text{sinc}(\Delta kL/2)|$ with respect to the PM wavelength in GaSe (L = 2 mm), at the PM angle of 13.2°, by using 2.5 μm as the pump wavelength.

4.5 Pulse characterization

The μJ-level output energy enables the temporal profile characterization using our home-built IAC in which a 1-mm thick GaSe is used as the SHG crystal due to the good phase-matching bandwidth and a 2-mm thick uncoated ZnSe placed at 45° is used as the beam splitter. The IPDFG beam after a 7.3 μm LPF with a 2-mm thick Ge substrate enters the IAC and is split into two beams by the ZnSe. The transmitted one goes through a delay line and is focused into the GaSe with the reflected one together using the parabolic mirror with an effective focal length of 150 mm in a collinear geometry. The generated SHG signal is refocused into a photodetector using a CaF_2 lens with a focal length of 100 mm. The SHG signal with the delay time is recorded using an oscilloscope.

The IPDFG pulse width is measured as 85 fs, which corresponds to 1.54 times TL duration (55 fs), as shown in Figure 4.11(a). The calculated residual second-order dispersion is -1540 fs^2 which is mainly from the ZnSe beam splitter in the IAC. Here, the contribution of the higher-order dispersions is not taken into account. The sign of the residual second-order dispersion is judged through inserting the Ge plates with the normal dispersion, or the ZnSe plates with the anomalous dispersion, and monitoring the changes of the pulse width. To compensate the residual dispersion, a 5-mm thick AR-coated Ge plate which gives $+1890 \text{ fs}^2$ dispersion is added. As shown in Figure 4.11(b), the IPDFG pulse is compressed to 60 fs which corresponds to 1.8 optical cycles and 1.09 times TL pulse width. The sub-2-cycle compressibility gives a direct evidence of the good coherence of the IPDFG pulse.
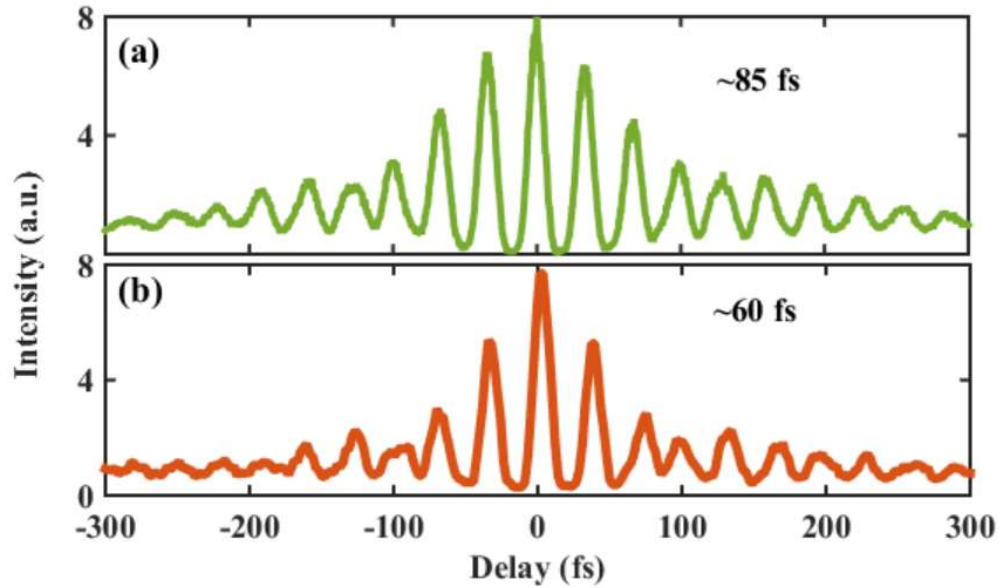
Figure 4.11 (a) The interferometric autocorrelator (IAC) trace of the IPDFG pulses behind the 7.3 μm LPF. (b) The IAC trace of the compressed IPDFG pulses using a 5-mm AR-coated Ge plate.

4.6 Conclusions

In conclusion, utilizing the SPM effect in a nonlinear crystal with a high nonlinear refractive index, we have demonstrated a SPM assisted IPDFG source covering 7-15 μm wavelength range, directly driven by a 3 μm OPCPA, without the use of an extra nonlinear pulse compression stage. The contribution of SPM on the signal generation (3.6 to 5.3 μm) in the IPDFG process is

experimentally confirmed. The generated IPDFG pulse has a pulse energy of 0.91 µJ (9.1 mW) and a 60 fs (1.8-cycle) pulse width, centered at 10.3 µm. To the best of our knowledge, this is the first report of the IPDFG driven at 3 µm wavelength and it shows the potential of the 3 µm OPCPA systems in producing the coherent mid-IR radiation. The few-cycle mid-IR IPDFG pulse could serve as a useful tool for coherent time-resolved applications.

Chapter 5 Highly efficient IPDFG and ultrabroadband SCG driven by IPDFG pulses

In Chapter 4, we know that the IPDFGs have been demonstrated for the broadband, few-cycle mid-IR pulse generation in non-oxide nonlinear crystals by using driving pulses at different wavelengths [68, 69, 125-131]. Here, we introduce a few representative works by considering their conversion efficiencies. T. Morimoto et al. demonstrated an 800 nJ, few-cycle IPDFG source covering 8 to 13 μm, driven by spectrally broadened 0.8 μm, 1 kHz, Ti:sapphire laser pulses [148]. I. Pupeza et al. used nonlinearly compressed, 1 μm, 100 MHz Yb:YAG laser pulses to produce few-cycle IPDFG pulses with the spectrum from 6.8 to 16.4 μm (at –30 dB) and 103 mW average power, in a LGS crystal [125]. However, the IPDFG efficiency driven by 0.8 μm or 1 μm pulses is relatively low (in the order of 0.1%). More efficient down conversion into the wavelengths of >5 μm has been achieved by using the longer-wavelength driving pulses for the lower quantum defect and the reduced nonlinear absorption in the non-oxide crystals. Using the 2 μm self-compressed, MHz laser pulses from the Tm-doped fiber lasers, C. Gaida et al. and T.P. Butler et al. demonstrated the 450 mW (at 1.25 MHz) and 500 mW (at 50 MHz) mid-IR output via IPDFG with the spectral coverage of 6 to18 μm in GaSe crystals, at the conversion efficiencies of 1.8% and 2%, respectively [68, 129]. S. Vasilyev et al. reported the IPDFG source spanning from 5.8 to 12.5 μm with a conversion efficiency of 3.3 %, using few-cycle, 78 MHz, 2.5 μm driving pulses from a Cr: ZnS laser and a ZGP nonlinear crystal [131]. These reports represent the state-of-the-art IPDFG sources for the high conversion efficiency.

In Chapter 4, we used 3 μm pulses directly from OPCPA system to produce mid-IR IPDFG output with 1% -1.6% conversion efficiency. However, such pulses are not optimized for efficient IPDFG conversion due to the necessary 'signal' components above 3.6 μm must be generated via SPM in GaSe. In this chapter, the 'signal' components above 3.6 μm are readily generated using YAG before driving the IPDFG stage and we further boost the IPDFG conversion efficiency to 5.3% which leads to a new record. The driver of IPDFG we use is 3 μm, 10 kHz, 95 μJ, 35 fs pulses from a YAG nonlinear compressor. 5 μJ, 50 mW, 68 fs corresponding to 2.1 cycles centered at 9.7 μm IPDFG pulses with a spectrum spanning from 6 to 13.2 μm are produced from a GaSe crystal. The resulted field strength of the IPDFG pulses can exceed 0.27 V/Å, enabling the study of HHG in solids, laser-induced electron diffraction for the imaging of ultrafast molecular dynamics, wave-

controlled ultrafast electronics in dielectrics and semiconductors, and the study of ultra-broadband SCG. As a demonstration of the application in the nonlinear optics in solid materials, we investigated its use in SCG. Pumped by the IPDFG pulses, a 2.4 μJ, 24 mW SC with a 3-octave spectrum from 2 to 16 μm in KRS-5 and a 2.7 μJ, 27 mW SC with a 2.3-octave spectrum from 3 to 14.5 μm are produced. Two SC spectra both support sub-cycle pulse widths. The results of this chapter have been published in [149].

5.1 Experimental setups

The schematic of the experimental setup is depicted in Figure 5.1, which consists of the 3 μm few-cycle driver and the IPDFG stage. Different from the setup for IPDFG in Chapter 4, a further compression of 3 μm pulses from the OPCPA system down to a shorter pulse duration is implemented in this setup.
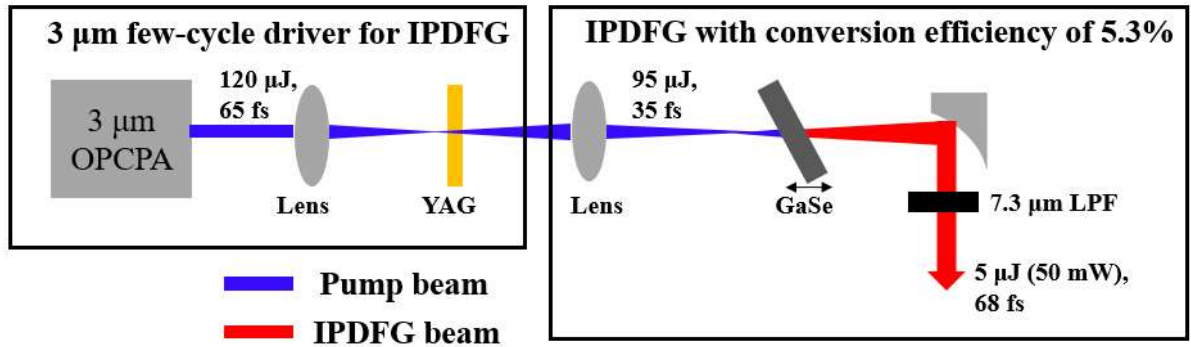
Figure 5.1 The schematic of experimental setups.

The 3 μm few-cycle driving source starts with a home-made multi-stage OPCPA based on PPLN and PPSLT crystals driven by a 10 kHz Yb: YAG Innoslab laser. It can deliver ~300 μJ, few-cycle, 3 μm pulses, see Chapter 3 and 4. The 120 μJ, 3 μm pulses are used and focused into a 2-mm-thick uncoated YAG crystal by an AR coated CaF_2 lens with a 75-mm focal length, for the nonlinear compression. Here, the YAG is chosen for its large nonlinear refractive index and good mechanical properties. It is placed at a position slightly after the focal spot to avoid the damage and the strong ionization. Inside the YAG, 3 μm pulses are spectrally broadened by the SPM, and simultaneously compressed in the temporal domain with the anomalous dispersion in YAG at 3 μm. The measured

pulse energy after the YAG is ~105 µJ, with the loss mainly from the Fresnel reflection and the weak ionization.

In the IPDFG stage, a GaSe with a thickness of 2 mm is chosen as the nonlinear crystal, same as the Chapter 4, for its broad transmission window (0.65-18 µm), large second-order nonlinearity (~50 pm/V from SNLO, good phase-matching bandwidth, and high damage threshold (~1.7 TW/cm^2). An uncoated CaF_2 lens with the focal length of 100 mm is used to focus the self-compressed 3 µm beam from the YAG plate to a beam diameter of ~600 µm at its beam waist. The pulse energy measured behind the uncoated CaF_2 lens is 95 µJ. In our experiment, the GaSe crystal is placed at a type-II phase-matching angle of ~13.2° (azimuthal angle (φ)=0°), and the IPDFG output is optimized for the output energy so as the conversion efficiency after the LPF with a cut-off wavelength of 7.3 µm. The parameters of optimization include: the pump intensity on GaSe by adjusting the position of GaSe from the beam waist and the energy distribution of the 3 µm driving pulses on the o-axis and e-axis by rotating the crystal along the propagation direction of the driving pulses. The long-wavelength and the short-wavelength components on the o-axis and e-axis serve as the signal and pump, respectively, in the DFG process, and the IPDFG output is generated as the idler. The IPDFG pulses are collimated by a gold-coated parabolic mirror (Thorlabs) and separated from the driving pulses by the different long-pass filters (LPFs). The characterizations of IPDFG pulses are accomplished by a series of setups, such as the thermal power meter, the monochromator with a liquid-nitrogen-cooled MCT detector, the mid-IR beam profiler and a home-built IAC.

5.2 Experimental results and discussion

The spectrum of the 3 µm OPCPA is shown as the red dashed curve in Figure 5.2(a), which has a spectral coverage from 2.8 to 3.4 µm. The temporal profile of the 3 µm OPCPA pulses measured by the SHG-FROG is revealed in Figures 5.2(b)-2(d). A 65 fs pulse width is measured as shown in Figure 5.2(d). This information is same as that in the last chapter. The spectrum of self-compressed pulses from YAG is shown as the black solid curve in Figure 5.2(a), with a spectral span from 2.3 to 4.5 µm. Here, the long-wavelength tail is measured with all energy behind 3.6 µm LPF coupled into the monochromator. It is worth mentioning that the new generated spectral components in the range of 3.4-4.5 µm which serves as the signal in the process of IPDFG are

crucial for the efficient conversion of mid-IR pulses via IPDFG. The good Gaussian beam profiles before and after nonlinear compression are compared in the inset of Figure 5.2(a), manifesting no degradation of the beam profile in the nonlinear compression process. The temporal profile of the self-compressed pulse is also characterized by using SHG-FROG, as shown in Figures 5.2(e)-2(g). A 35 fs pulse width is measured with a FROG error of ~0.9% and a free frequency marginal, which corresponds to a 1.08 times TL pulse width. Further pulse compression down to shorter pulse width and broader spectrum by placing the YAG at a position of higher intensity is possible. However, this does not increase the conversion efficiency of IPDFG due to the walk-off length limit between signal and pump.
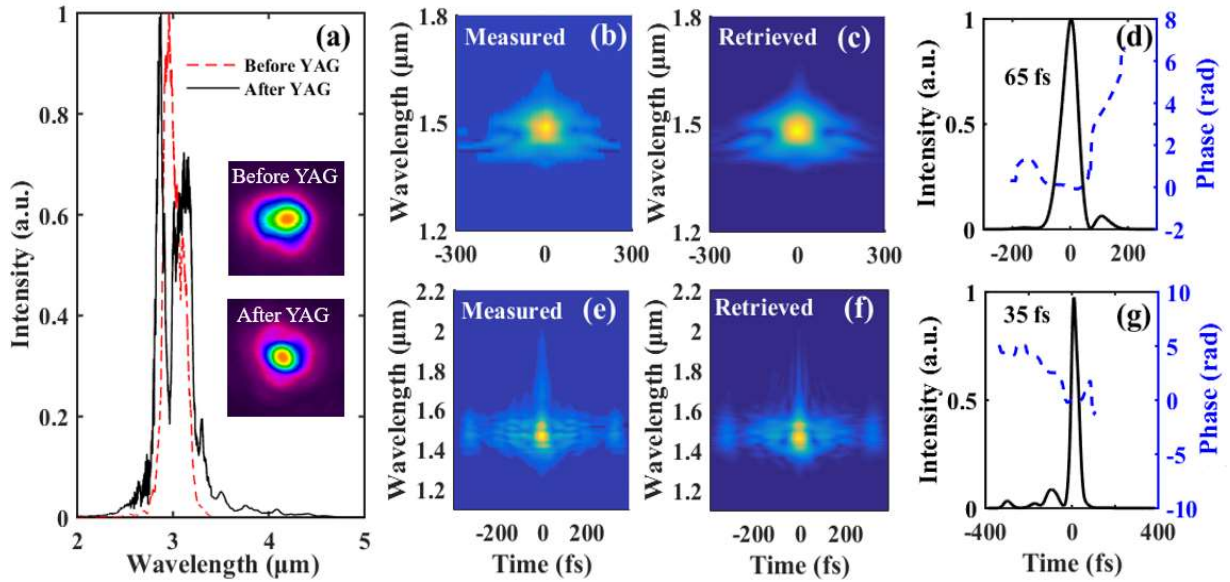
Figure 5.2 Characterization of the 3 μm driving pulses. (a) The spectra before and after the nonlinear pulse compression. Inset: the beam profiles before and after the nonlinear compression. (b)-(d) show the measured FROG trace, the retrieved FROG trace and the pulse shape, respectively, for the 3 μm pulses before nonlinear compression. (e)-(g) show the measured FROG trace, the retrieved FROG trace and the pulse shape, respectively, for the 3 μm pulses after nonlinear compression.

The dependence of the IPDFG output and conversion efficiency on the pump intensity is shown in Figure 5.3. It is found that the roll-over of the IPDFG output occurs when the pump intensity is increased to ~295 GW/cm^2, and the measured maximum IPDFG output pulse energy behind the 7.3 μm LPF is 5 μJ (50 mW in average power). This corresponds to a 5.3% conversion efficiency from the 3 μm driving pulses to IPDFG output, which, to the best of our knowledge, represents

the highest IPDFG efficiency to date. Taking into account the losses from the LPF (10%), the parabolic mirror (6%) and the surface reflections of the uncoated GaSe crystal, the internal conversion efficiency is up to 8.3%. This proves the advantage of the 3-μm-driven IPDFG in enhancing the conversion efficiency due to lower quantum defect compared to IPDFG sources driven at 0.8 [148], 1 [125], 2 [68, 129] or 2.5 μm [131]. In addition, it is worth mentioning that the 5 μJ output pulse energy is much higher than that of the reported advanced IPDFG sources at high repetition rates [68, 129, 131], which makes our source suitable for some particular applications, such as HHG or SCG in solids. The inset of Figure 5.3 shows that the IPDFG output has a Gaussian beam profile at 5 μJ output energy, which allows good focus for the strong-field applications. Using the same optimization approaches, 0.5 mm and 1 mm-thick crystals are also used for the IPDFG, with IPDFG outputs of ~30 nJ and ~900 nJ for 0.5-mm and 1-mm thick crystals. It is found that the IPDFG output is much lower than 2-mm thick crystal. This is because that the gain of IPDFG grows exponentially with the crystal thickness, a thicker crystal obviously increases the IPDFG output.
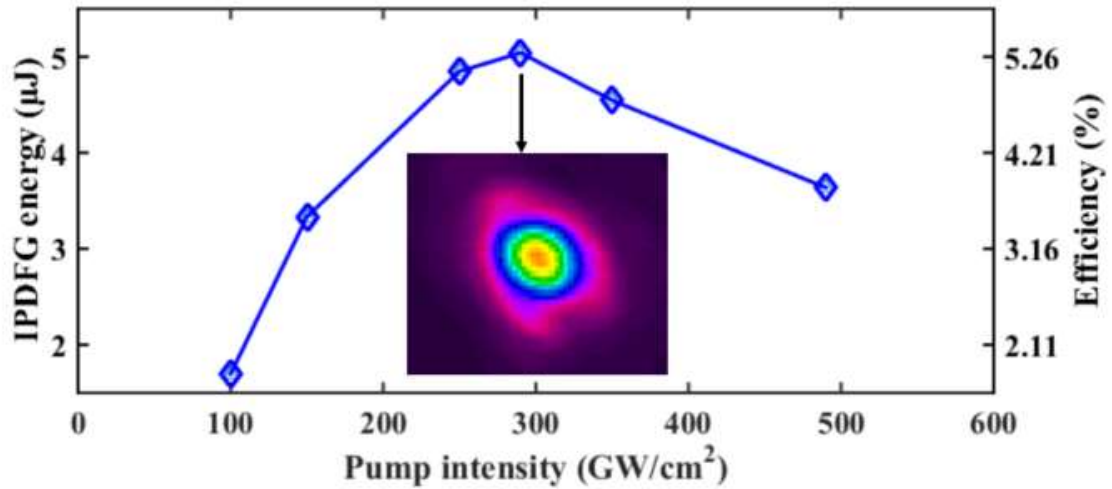
Figure 5.3 The IPDFG output energy and conversion efficiency measured behind a 7.3 μm LPF at different pump intensities. The inset shows the measured beam profile for 5 μJ IPDFG output.

The IPDFG spectrum at the highest output energy is shown in Figure 5.4(a), which spans from 6 to 13.2 μm. Some large dips are found in the IPDFG spectrum, which are mainly caused by the spectral shapes of the short-wavelength pump and the long-wavelength signal in the driving pulses. For example, the CO_2 absorption line at 4.3 μm in the signal spectrum is transferred to the IPDFG

spectrum in the IPDFG process, leading to a spectral dip at 10.7 μm with 3.07 μm serving as pump, as presented in Figure 5.4(a).
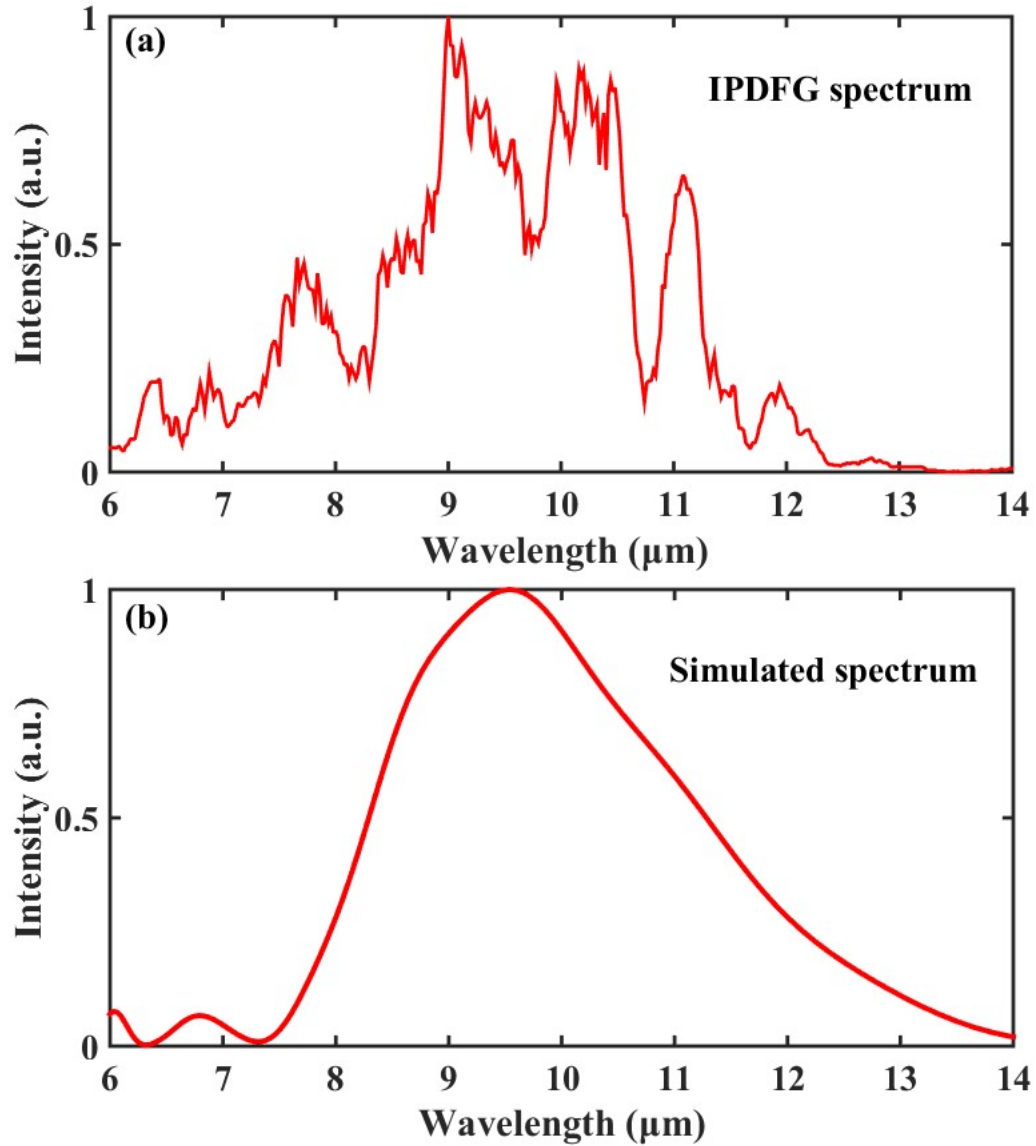
Figure 5.4 (a) The measured IPDFG spectrum at 5 μJ output energy. (b) The simulated IPDFG spectrum.

We also measured the amplified signal of >3.6 μm using the 3.6 μm LPF, which is shown in Figure 5.5(a). It is found that the amplified signal covers up to 6 μm in spectrum, however, the long-wavelength tail from the 3 μm driving pulses can only reach 4.5 μm, as shown in Figure 5.2(a). Thus, some new spectral components at 4.5-6 μm are generated, serving as signal in the IPDFG process. The origin is attributed to the SPM caused spectral broadening as discussed in

Chapter 4 and the cascaded processes [130]. Figure 5.5(b) shows the measured signal spectrum after the GaSe crystal by rotating the azimuthal angle (φ) of GaSe to 90°, in order to suppress the amplification. One finds the signal without amplification is spectrally broadened due to the high nonlinear refractive index of GaSe ($450 \times 10^{-16} cm^2/W$ [134]). The spectral components of 4.5-6 μm are emerged, which provides an explanation for what is found in the amplified signal. In this case, the energy behind 3.6 μm LPF is 4 times higher than that without GaSe, giving another evidence that SPM makes contribution.

In addition, the intrinsic cascade processes can also be responsible for the origin of the 4.5-6 μm spectral components. One example of the cascaded process is that with the same PM angle, the 7.5 μm idler is firstly generated via IPDFG between the 2.5 μm and 3.75 μm components in the driving pulses. Subsequently, the generated 7.5 μm idler serves as a new 'signal', and is amplified by the 3 μm pump to obtain the 5 μm spectral component in the amplified signal. Similarly, other 4.5-6 μm signal spectral components could be produced by similar cascaded processes. Therefore, it is suggested that the IPDFG process is assisted by both the SPM and the cascaded effect.
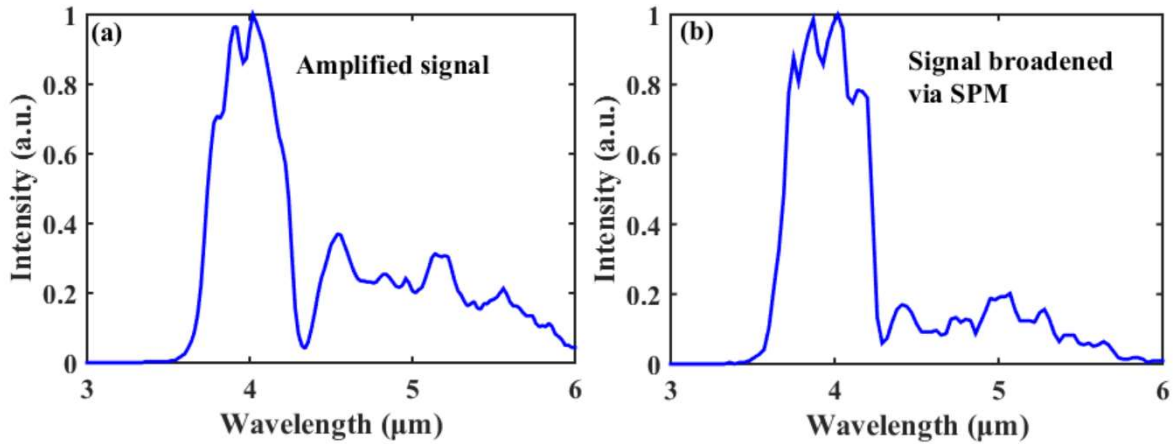
Figure 5.5 (a) The amplified signal spectrum measured behind the 3.6 μm LPF. (b) The broadened signal spectrum via SPM, measured behind the 3.6 μm LPF by rotating the azimuthal angle (φ) of GaSe to 90°, to turn off the amplification.

A simulation is also done using a (2 + 1) dimensional nonlinear pulse propagation code [150]. Different from some simulation codes which solve three coupled-wave differential equations using the split-step Fourier methods, the (2 + 1) dimensional simulation code solves only two coupled-

wave differential equations with two orthogonal linear polarizations (o-polarized and e-polarized) using the Euler method. The latter is more suitable for the broadband parametric processes, especially when pump, signal, idler overlap in spectrum such as IPDFG. What is more, this code contains all possible second-order nonlinear processes for all involved ultrafast pulses and the cascade effects are thus included automatically. For our experiment, SPM and self-focusing effects make contributions due to the high nonlinear refractive index and long crystal thickness of GaSe, therefore they are included in the simulation. 82 µJ, 35 fs, 3 µm FT Gaussian pulses with a collimated geometry are used as the driver of GaSe and they are distributed for 80 µJ on e-axis as pump and 2 µJ on o-axis as signal. The phase-matching angle is set to $13.2°$ for Type-II. Figure 5.4(b) shows the simulated IPDFG output for > 6 µm wavelength at an output energy of 5.3 µJ. The simulated spectrum is quantitively matched with the measured one with a slightly broader spectrum spanning from 6 to 14 µm. The dips are not found in the simulated spectrum. This is because the driving spectrum is assumed as a smooth Gaussian shape, the dips contributed by absorption dips of the driving spectrum vanishes in the simulated spectrum.

The energy stability of the mid-IR sources is an important parameter for the molecular spectroscopy and strong-field applications. The measured energy fluctuation of the IPDFG output is 1.1% rms for 1-hour measurement duration, as shown in Figure 5.6(a). The good energy stability of the IPDFG mainly benefits from the stable driving pulses with less than 0.7% rms fluctuation. Moreover, the IPDFG pulse width is characterized using the home-built IAC in which a 0.5 mm thick GaSe is used as the SHG crystal for its good SHG phase-matching bandwidth at ~10 µm. The dispersion of 2-mm-thick ZnSe serving as a beam splitter in the IAC is compensated using a Ge plate. The measured IAC trace of the IPDFG output after the 7.3 µm LPF is shown in Figure 5.6(b). It is worth noting that the 7.3 µm LPF cuts some spectral components from 6 to 7.3 µm, and the temporal profile measurement with the full IPDFG spectrum could be achieved by using a LPF with the cut-off wavelength of 6 µm. Figure 5.6(b) reveals a 68 fs pulse width corresponding to 2.1 cycles centered at 9.7 µm, and 1.2 times the TL pulse width. It agrees well with the calculated IAC trace, which is obtained by adding the -1300 fs^2 second-order dispersion into the TL pulse based on the measured spectrum behind the 7.3 µm LPF. The residual dispersion is mainly from the 2-mm-thick GaSe and the 7.3 µm LPF with a 1-mm-thick Ge substrate. The field strength of 5

µJ, 68 fs IPDFG pulses could reach 0.27 V/Å at a beam diameter of 70 µm, disclosing new opportunities to investigate nonlinear phenomena like SCG or strong-filed physics in solids.
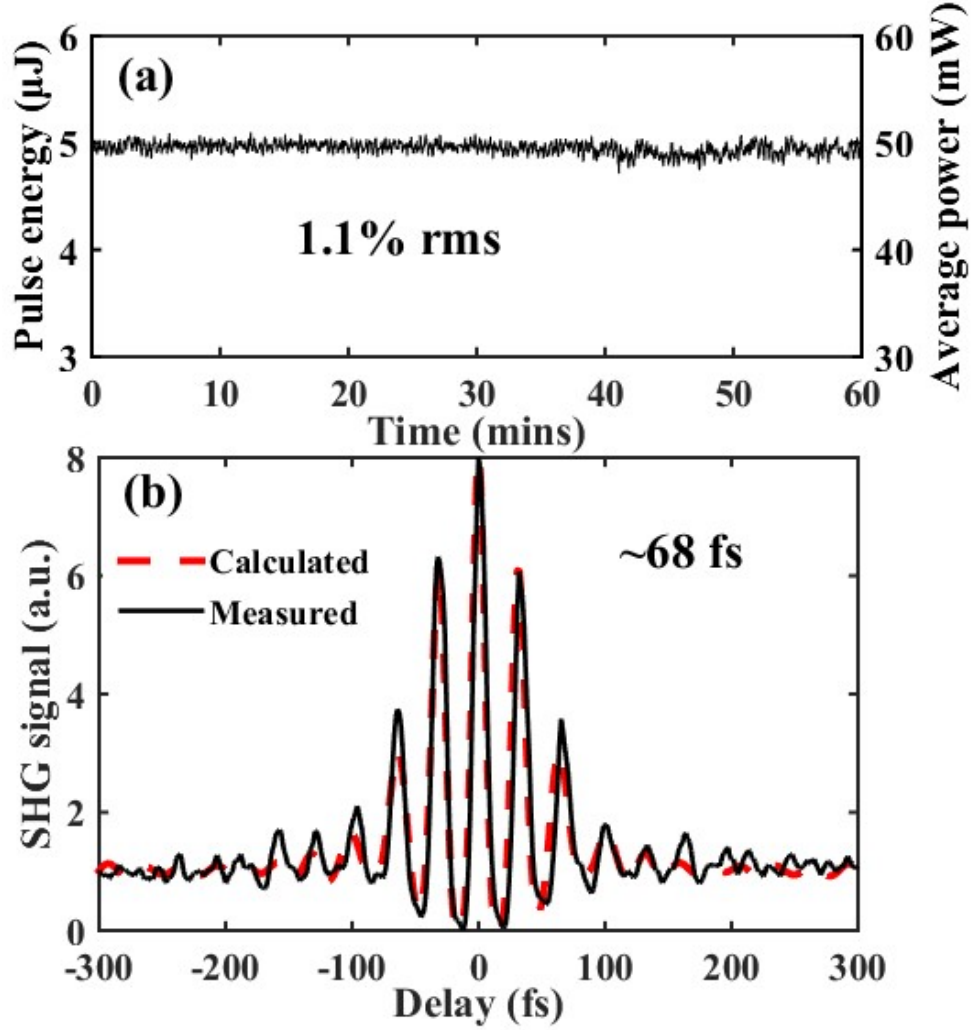
Figure 5.6 (a) The measured energy stability of IPDFG output behind the 7.3 µm LPF. (b) The measured and calculated IAC traces behind the 7.3 µm LPF. The calculated IAC is obtained by adding the -1300 fs^2 dispersion which is mainly from the 2-mm-thick GaSe and the 7.3 µm LPF with a 1-mm-thick Ge substrate into the TL pulse based on the measured spectrum.

5.3 Mid-IR SCG via filamentation driven by IPDFG pulses

SCG in bulk materials via filamentation is a simple and compact technique to broaden a narrow-band spectrum of femtosecond or picosecond pulses to a broadband spectrum covering multiple octaves simultaneously with a good coherence and a moderate brightness. Unlike the second-order

nonlinear processes, SCG is insensitive to the crystal angle and thus reduces the reliability on the environments. SCG in the mid-IR spectral range is highly desired for the multiple-molecule spectroscopy. In the multiple-molecule spectroscopy, to simultaneously analyze those molecules, several lasers are often required due to limited spectral width of one single laser. This adds the measurement time. The SC mid-IR sources covering the overall wavelength range of interest are expected to overcome this limitation. In addition, SCG in bulks also provide a few-cycle or even one-cycle pulses by the design of the pump wavelength and nonlinear materials, benefiting the time-resolved spectroscopy.

Intensive advances have been made for the broadband, coherent mid-IR SCG via filamentation in bulk materials in recent years. In 2012, a 3.3-octave SC from 450 nm to the mid-IR was demonstrated for the first time in a bulk material [151]. In which, 3.1 μm, 85 fs pulses were used to drive the filamentation in YAG. The simulation shows the pulse width of the SC pulses was of near-single cycle, with a compression factor of 10. In 2015, a systematic investigation of the filamentation in CaF_2, BaF_2 and ZnS using 2.1μm, 27 fs pulses was reported [152]. The broadest SC spectrum was generated from the ZnS with a spectral span from 500 nm to beyond 4.5 μm, corresponding to 3.1 octaves. CaF_2 and BaF_2 gave relative narrow spectral span with the long-wavelength extension of 3.3 μm and 3.8 μm. Despite the relatively narrow SCG in CaF_2 and BaF_2, the pulses were self-compressed to 27 fs and 19 fs, respectively, due to the pump wavelength located in the negative second-order dispersion region of both crystals. In 2017, fused silica, YAG and LiF were systematically investigated for filamentation-assisted SCG using 2.3 μm, 100 fs pulses [153]. Multi-octave SC was generated with the spectrum from 310 nm to 3.75 μm in fused silica, from 350 nm to 3.8 μm in YAG and from 290 nm to 4.3 μm. In 2019, using NaCl and KBr as the nonlinear materials, 0.7 to 5.4 μm and 0.8 to 5.4 μm SC spectra were produced with the 3.6 μm, 70 fs pulses [154]. Despite NaCl and KBr have very broad transmission windows (0.17-18 μm for NaCl and 0.2 -30.6 μm for KBr) and the pump wavelength is the vicinity of the zero dispersion points of both crystals, no longer wavelength spectral components were observed. This was explained as the formation of persistent color centers which significantly limited the transmission energy and narrowed the SC spectra. KRS-5 and KRS-6 with a ultrabroad transmittance up to 42 μm and 27 μm were also verified for the broadband single-filamentation generation, with the similar spectral coverage from 1.5 to more than 5.5 μm using 3.1 and 3.6 μm,

60 fs pulses, respectively [155]. The access to the long-wave parts of the mid-IR spectrum have been achieved using pump pulses at a longer wavelength. In ZnSe, a multi-filamentation-assisted SC covering 0.5 -11 µm was reported using pump pulses centered at 5 µm [156]. 3- 18 µm SC was generated using 7.9 µm, 150 fs pulses, with a pulse self-compression down to 45 fs in GaAs [157]. Besides the aforementioned crystals, fluoride, tellurite, lanthanum and chalcogenide glasses also produced broad mid-IR coverage with up to 10 µm [158-161]. In this section, we report an ultra-broad SCG in KRS-5 and ZnSe with the spectra from 2 to 16 µm and 3 to 14 µm at a pulse energy of 2.4 µJ and 2.5 µJ, respectively, driven by the IPDFG pulses produced in last section.

Table 5.1 The parameters of some commonly used crystals with the broader transmission in the mid-IR. λ_0 and n_2 represent the zero dispersion point and the nonlinear refractive index, respectively.

Materials	Bandgap (eV) [97]	Transmittance (µm)[97]	λ_0 (µm)	n_2 ($\times 10^{-16}$ cm^2/W)
NaCl	9.0	0.17-18	2.76	4.35 [154]
KBr	7.6	0.2-30.6	3.83	7.95 [154]
ZnSe	4.	0.5-20	4.8	85 [163]
GaAs	1.4	0.9-20	6.8	500 [97]
KRS-5	2.5	0.85-42	6.6	105 [155]
KRS-6	3.25	0.42-27	-	54 [155]
KI	10	0.25-39	4.53	29 [162]

A recent simulation predicted the femtosecond pulses with a wavelength deeply in the mid-IR are helpful to produce multi-octave SC with remarkable red shifts via filamentation in the deep negative second-order dispersion region of crystals [162]. Therefore, the criteria for the selection

of nonlinear crystals is based on the broad transmission in the mid-IR, high nonlinear refractive index, zero dispersion point deeply below the pump wavelength. The oxide crystals such as fused silica and YAG and fluoride crystals such as CaF_2 and BaF_2 are excluded due to their transmission limit. Table 5.1 lists the parameters of some commonly used crystals with the broader transmission in the mid-IR. For those crystals, NaCl and KBr have been demonstrated for the formation of color centers limiting the spectral broadening in filamentation. Therefore, they are not suggested. However, ZnSe, GaAs, KRS-5, KRS-6 and KI satisfy the criteria. Two of them, i. e. ZnSe and KRS-5, are chosen in our experiment for the broadband SCG.

The Figure 5.7 shows the schematics of the SCG setup. The 5 μJ, 68 fs IPDFG pulses centered at 9.7 μm are focused into the uncoated 8 mm thick KRS-5 or 9 mm thick ZnSe crystals using a parabolic mirror with an effective focal length of 38 mm. In order to avoid damage and suppress the multi-filamentation, the crystals are placed after the focus point of the parabolic mirror, and the pump intensity on the crystals are carefully adjusted using a linear stage. To ensure the single-filamentation generation, a beam profiler is used to monitor the beam shape of the generated SC pulses when optimization is made. The generated SC pulses are collimated by another parabolic mirror with an effective focal length of 50 mm, then they are characterized using a series of setups. The calculated critical peak powers for self-focusing of KRS-5 and ZnSe are 5.6 MW and 10.1 MW, respectively. Taking into account the losses from the parabolic mirror (6%) and the surface reflection (16.5% and 17%) of KRS-5 and ZnSe, the peak powers inside KRS-5 and ZnSe are both ~57 MW. They are ~10 times and 5.6 times higher than the corresponding critical peak powers.
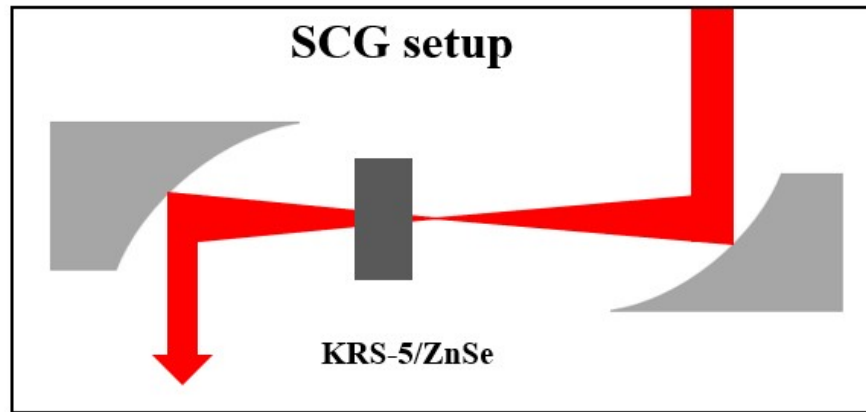
Figure 5.7 The setup of SCG.

When stable single-filamentation is generated from KRS-5, the beam profile and the spectrum of SCG are measured, shown in the Figure 5.8 and its inset. The beam has a Gaussian distribution in the center of the beam and some weak outer rings surrounding the center due to the distortion caused by the unperfect aligned parabolic mirror. The SC spectrum covers from 2 to 16 μm at -30 dB intensity, corresponding to 3 octaves. The sharp dips at 4.3 μm and 15 μm are caused by CO_2 absorption in air. This SC covers more spectral components deeply in the mid-IR than the SC generated in KRS-5 driven at 3.1 and 3.6μm, in which a 1.5 -5.5 μm SC is generated. In the filamentation, SPM broadens the spectrum of pump pulses symmetrically in blue and red parts, see the equation (3.1). However, we cannot find the symmetry in the SC spectrum. More blue shifts are found, this can be attributed to the self-steepening effect. In KRS-5, the instantaneous refractive index, $n = n_0 + n_2I(t)$, increases with the field intensity. Therefore, the peak of the driving pluses has a lower velocity than the trailing edge of the driving pulses. After the propagation of the pulses in KRS-5, the trailing part catches up with the peak, leading to a steep edge in the trailing part of pulses. From the equation, we can see the new formed spectral components in the trailing part becomes more blue-shifted due to the self-steepening. This explains the more blue-shifted spectrum in the SCG. The measured pulse energy of SC is 2.4 μJ (24 mW in average power). ~52% energy is lost from the input pulses to the output pulses. Amongst, ~38% loss is caused by the parabolic mirrors and surface reflections of KRS-5. The other ~14% is due to the ionization during filamentation. With the ultrabroad spectrum which covers most of the molecular fingerprint region and a 24 mW average power, this SC is especially suitable for the multi-molecule spectroscopy.
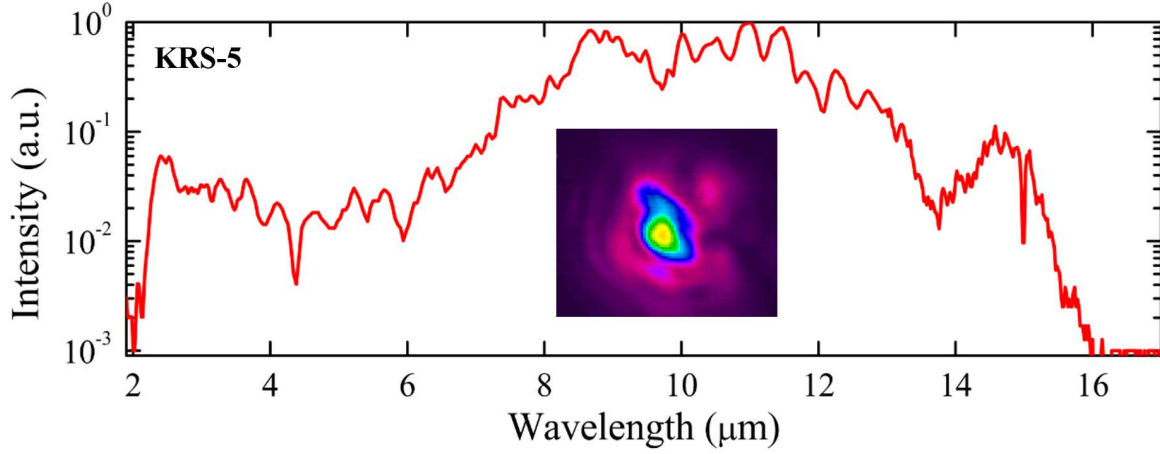
Figure 5.8 The SC spectrum assisted by a single filament from the KRS-5 crystal driven by the IPDFG pulses. The inset shows the corresponding SC beam profile.
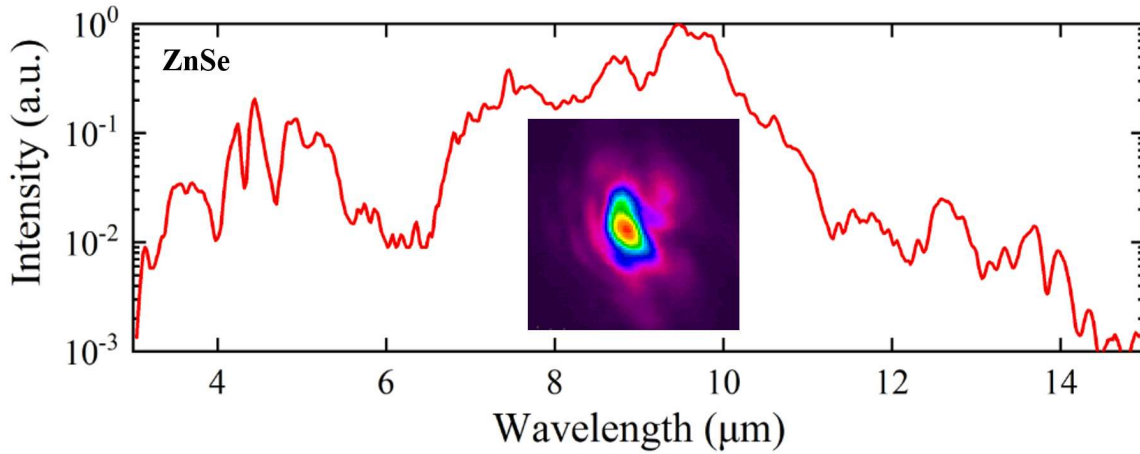
Figure 5.9 The SC spectrum assisted by a single filament from the ZnSe crystal driven by the IPDFG pulses. The inset shows the corresponding SC beam profile.

In ZnSe, when the stable single-filamentation is generated, the spectrum and the beam profile of SC are shown in the Figure 5.9 and its inset. Similar beam profile is observed with that in KRS-5 and the spectrum has a 2.3-octave span from 3 to 14.5 μm at -30 dB intensity. Compared with the SC spectrum in KRS-5, the bandwidth in ZnSe is slightly narrow due to the less flatness of the second-order dispersion at the pump wavelength (see the Figure 5.10). Different from the KRS-5, the polycrystalline ZnSe is non-centrosymmetric with a high second-order nonlinear coefficient (d_{eff}~20pm/V [101]) and random quasi phase-matching. Therefore, beside the SPM caused spectral broadening in the short-wavelength range, the SHG contributes as well. A peak at ~5μm,

which is the SHG of fundamental, is found in the SC spectrum of ZnSe, which does not appear in that of KRS-5 due to the vanished SH nonlinearity. The measured SC pulse energy is 2.7μJ (27 mW in average power), with an ionization loss of ~15% similar to that in that in KRS-5.
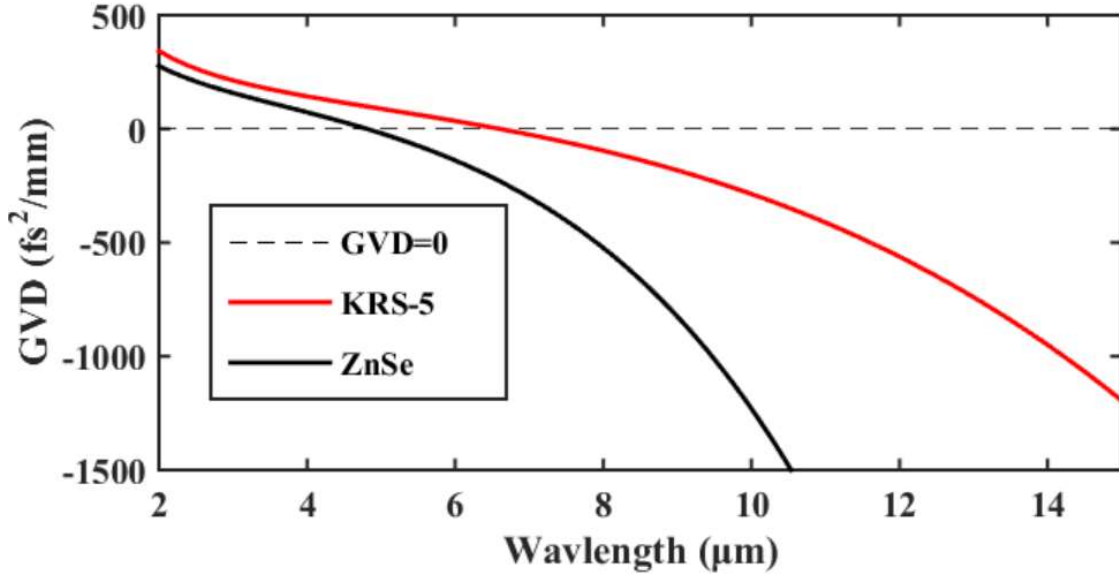
Figure 5.10 The second-order dispersion curves of KRS-5 and ZnSe between 2 and 15 μm.

Another aspect worth mentioning is that the SPM and KRS-5/ZnSe bring positive and negative chirps into the pulses, respectively. The pulse-self-compression is companied with the broadening of the spectra in both crystals. The FT pulse widths supported by the SC spectra of KRS-5 and ZnSe are 8 fs and 13 fs. Thus, sub-cycle pulses are expected. Combined with beyond 2 μJ pulse energy, the peak electric field could reach > 10 GV/m or 0.27 V/Å. Such sub-cycle pulses open a way for the electron microscopy with ultimate temporal and spatial resolution besides the spectroscopy.

5.4 Conclusions

Using 3 μm, 10 kHz, 35 fs nonlinearly compressed pulses from our OPCPA system as the IPDFG driver, we boost the IPDFG conversion efficiency to 5.3% in this Chapter. Compared with the IPDFG conversion efficiency using pulses before nonlinear pulse compression in Chapter 4, the efficiency is boosted by at least 3 times. This, to the best of our knowledge, represents the highest IPDFG efficiency to date. The 5 μJ, 50 mW, 68 fs pulses with a spectrum spanning from 6 to 13.2

μm are delivered, which could lead to a field strength of 0.27 V/Å at a beam diameter of 70 μm. Some applications such as SCG and HHG in solids could be pursued by the demonstrated high-energy IPDFG, compared to current state-of-the-art IPDFG sources at high repetition rates. Moreover, we give an application example for our IPDFG source in SCG. Pumped by the IPDFG pulses, a 2.4 μJ, 24 mW SC with a 3-octave spectrum from 2 to 16 μm in KRS-5 and a 2.7 μJ, 27 mW SC with a 2.3-octave spectrum from 3 to 14.5 μm are produced. Two SC spectra both support sub-cycle pulse widths.

Chapter 6 Ultrabroadband mid-IR OPA

In above Chapters, we have studied the generation of two-cycle mid-IR pulses with a broadband spectrum from 6 to 15 µm and a uJ-level pulse energy, using an IPDFG method. To pursue a broader parametric source, in this chapter, we develop a multi-microjoule, ultra-broadband mid-IR OPA source based on a GaSe nonlinear crystal and a driven source at ~2 µm. Benefiting from the better phase-matching bandwidth of GaSe at 2 µm pump wavelength, we obtain idler pulses with a flat spectrum spanning from 4.5 to 13.3 µm at -3 dB and 4.2 to 16 µm in the full spectral range, at a central wavelength of 8.8 µm. The proposed scheme supports a sub-cycle TL pulse width of ~19fs. A (2+1)-dimensional numerical simulation is employed to reproduce the obtained idler spectrum. To our best knowledge, this is the broadest spectrum ever obtained by OPA systems in this spectral region. The idler pulse energy is ~3.4 µJ with a conversion efficiency of ~2% from the ~2 µm pump to the idler pulses. We believe the generated multi-microjoule, few-cycle, ultra-broadband, long-wavelength mid-IR pulses would be impactful for both mid-IR molecular spectroscopy and strong-field physics in solids. The results of this chapter have been published in [164].

6.1 Phase matching of GaSe at 2 µm

We have summarized some nonlinear crystals with the transmission in long-wavelength mid-IR in Section 4.1 of Chapter 4. By the comparison of specifications between AGSe and GaSe, GaSe is chosen as the crystal for the 3 -µm-driven IPDFG. Here, we further analyze whether the GaSe is still more suitable than AGSe at the 2 µm pump wavelength. At the 2 µm pump wavelength, the dependences of phase-matching wavelengths on the phase-matching angles for Type-I and Type-II in AGSe and GaSe are shown in Figure 6.1. With the comparison analysis similar to that at 3 µm pump wavelength, we find that GaSe still has a better phase-matching than AGSe whether for Type-I or for Type-II. Thus, GaSe is chosen. In the implemented OPA experiment, a 1-mm-thick GaSe is used. Figure 6.2 shows the phase-matching function $|sinc(\Delta kL/2)|$ with respect to the phase-matching angle and the phase-matching wavelength for Type-I and Type-II, where a pump wavelength of 2.15 µm are used, which is the pump wavelength used in our experiment, for the calculation. For Type-I and Type-II, both group velocity matching points of signal and idler are found. However, For Type-I, within $\sim0.4°$ deviation of the phase-matching angle, centered at

$\sim$11.1°, the phase-matching bandwidth of the idler ranging from 4 to 16 μm could be realized. For Type-II, with $\sim$0.4° deviation of the phase-matching angle, centered at $\sim$12.3°, the phase-matching bandwidth only span from 9 to 15 μm. It is narrower than Type-I. Therefore, Type-I phase-matching is selected.
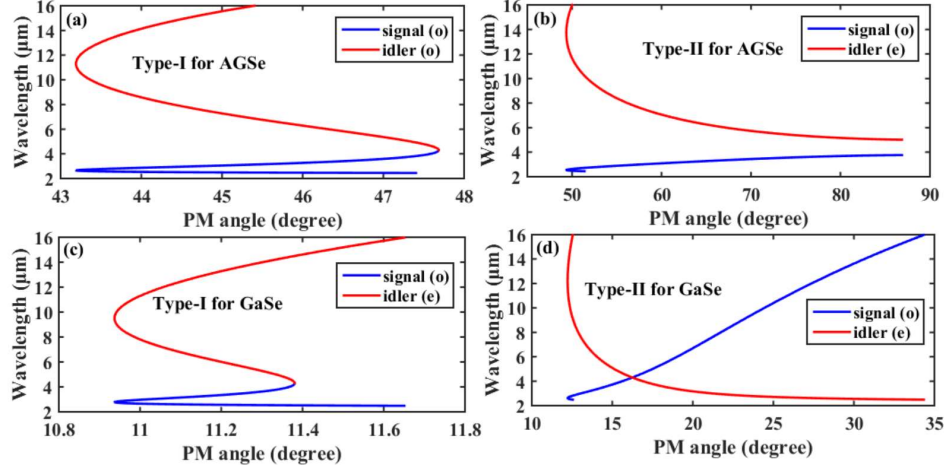
Figure 6.1 Phase-matching wavelength versus phase-matching angle in AGSe and GaSe, calculated using SNLO. (a) and (b) are for Type-I and Type-II in AGSe. (c) and (d) are for Type-I and Type-II in GaSe.
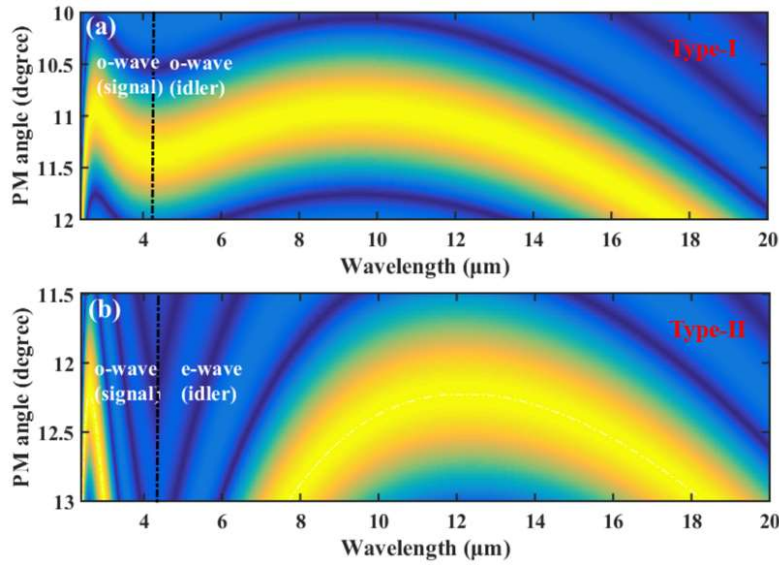
Figure 6.2 The PM function |sinc(ΔkL/2)| with respect to the PM angle and the PM wavelength, in a GaSe crystal with a length (L) of 1 mm, for the Type-I phase match, at a 2.15 μm pump wavelength.

74

6.2 The pump source and experimental setups

The pump source is a commercial multi-stage BBO-based OPA system (TOPAS from Light Conversion), which is driven by a 5 mJ, 26 fs, 800 nm Ti: Sapphire laser system at a 1 kHz repetition rate. It can deliver 1.2-2.6 μm pulses with few hundreds of μJ. We tune the TOPAS output at a ~2 μm wavelength. At this wavelength, the corresponding pulse energy is measured as 420 μJ using a thermal sensitive power meter. Subsequently, the spectral and temporal profiles of ~2 μm pulses from TOPAS are characterized using the spectrometer and the AC. The measured spectrum is shown in Figure 6.3(a). It has a full width at half maximum of ~220 nm, centered at 2.15 μm, which supports ~31 fs TL pulse width. The AC trace, shown in Figure 6.3(b), reveals the pulse width of ~51 fs, with the assumption of a Gaussian temporal profile, indicating that some residual dispersions are included in the pulses. Those dispersion are mainly from the TOPAS optics, including about -400 fs^2 dispersion from the beam splitter with a substrate of 3-mm-thick fused silica (reflecting 800 nm, and transmitting 2.15 μm).
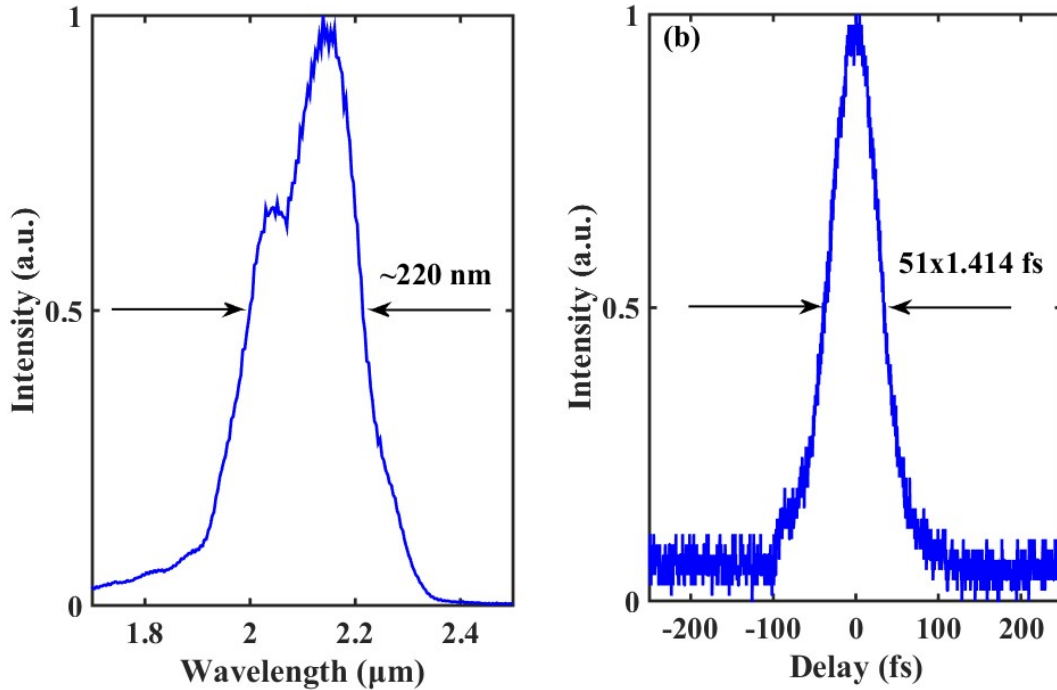
Figure 6.3 (a) The measured pump spectrum from the TOPAS source with a ~420 μJ output energy. (b) The autocorrelation trace of the pump pulses with the ~420 μJ output energy.

Figure 6.4 shows the layout of the OPA system starting from the driving source. The driving beam is split into two using a CaF_2 wedge placed at $22°$ with respect to the driving beam. The reflected one is used to drive SCG stage to generate the signal of OPA. The transmitted one possessing major energy is used to serve as the pump of OPA. In the SCG stage, the reflected p-polarized pulses with ~10 μJ pulse energy are rotated to s-polarization by a HWP, and then focused into a 6-mm thick BaF_2 by L_1 to generate SC pulses. Here, BaF_2 is used due to its better spectral broadening in the mid-IR wavelength [152]. Before reaching the GaSe crystal, the SC pulses are collimated by L_2 and resized to ~2.5 mm $1/e^2$ diameter by a telescope comprised of L_3 and L_4. The transmitted 2.15 μm pulses enters the pump line, which includes a delay line and a telescope (L_5 and L_6), to form a collimated pump beam with a comparable beam size as that of the signal beam.
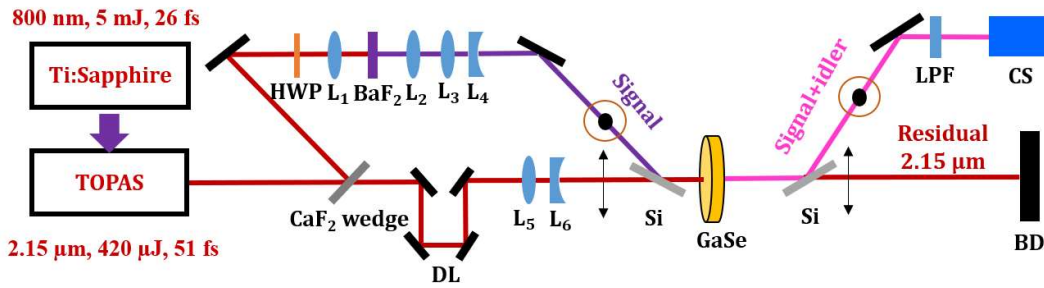
Figure 6.4 The schematic of the GaSe-based mid-IR OPA. The pump, the generated SC, and the amplified mid-IR pulses are shown in maroon, purple, and pink, respectively. (HWP-half wave plate, DL: delay line. LPF: long pass filter. BD: beam dump, CS: characterization setups. L_1-L_6 are CaF_2 lenses.

Due to the lack of dichroic mirrors (DMs) for pump and signal, a 300-μm thick Si plate placed at a Brewster angle of $73.8°$ with respect to the pump beam are used as the beam combiner. This plate produces ~71% reflection for the s-polarized signal beam and ~100% transmission for the p-polarized pump beam, as shown in Figure 6.5(a). The combined beams enter the GaSe crystal with a thickness of 1-mm thickness for the mid-IR pulse generation. As the GaSe crystal could be cleaved only along the (001) plane (z-cut, $θ = 0°$), an internal phase-matching angle of ~$11.1°$ corresponding to an external angle of ~$32°$ for Type-I is introduced. This causes ~16% loss for the p-polarized pump. It is noted that the pump beam is routed to the crystal using multiple silver mirrors with a ~96% reflection for each. Taking into account all the losses, the maximum

available pulse energy of the 2.15 μm pump is ~300 μJ, giving an estimated peak intensity of ~224 GW/cm^2. After the GaSe crystal, another Si plate placed at the same Brewster angle is used to split the residual pump, the amplified signal and the generated idler beams. Because the signal and idler beams have the same polarization states and they are both reflected by the Si plate with ~71% reflection coefficient, a LPF with a cut-off wavelength of 4.5 μm is used to separate the generated idler beam from the amplified signal beam further. At last, the mid-IR pulses are characterized by a thermal sensitive power meter with a resolution of 1 μW (S401C, Thorlabs) and a calibrated mid-IR monochromator with a liquid-nitrogen-cooled MCT detector. For the spectral measurement, an uncoated ZnSe lens with a near-flat transmission over 1-15 μm (Figure 6.5(b)) and a dielectric-coated mid-IR hollow-core fiber with a 500-μm core diameter (HF500MW, OptoKnowledge) are employed to couple the mid-IR pulses into the monochromator. The hollow-core fiber has a near-flat transmission in the range of 3.2-16 μm (the inset of Fig. 6.5(b)).
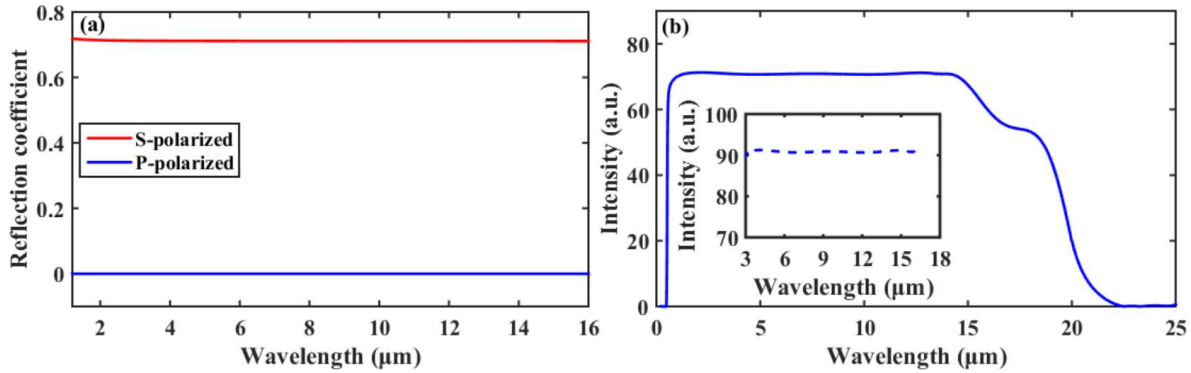
Figure 6.5 (a) The reflection coefficient of silicon plate placed at Brewster angle for s-polarized and p-polarized light in the range of 1.2 to 16 μm. It provides ~71% reflection for s-polarized signal and idler and ~100% transmission for p-polarized pump. It is very suitable for serving as the beam combiner and splitter of signal, idler and pump. (b) The referenced transmission curves (from Thorlabs) of the uncoated ZnSe lens and the inset shows the referenced transmission curves of the mid-IR hollow-core fiber at 3.2-16 μm.

6.3 Experimental results and discussion

For broadband SCG in BaF_2, the pump energy and the beam size are carefully optimized using an iris. Figure 6.6 shows the long-wavelength side of the SC spectrum (measured through a InF_3 fiber and a 2.4 μm LPF) which serves as the signal of the mid-IR OPA. It extends up to ~4.3 μm. The dip at ~2.7 μm is related to the water absorption in air and the OH absorption in the InF_3 fiber.

With the knowledge of the long-wavelength edge of the signal, the calculated spectral edge on the short-wavelength side of the generated idler is <4.3 μm, which means the signal and idler overlap in the frequency domain. Thus, the LPF with a 4.5 μm cut-off wavelength is employed to separate the generated idler from the amplified signal.
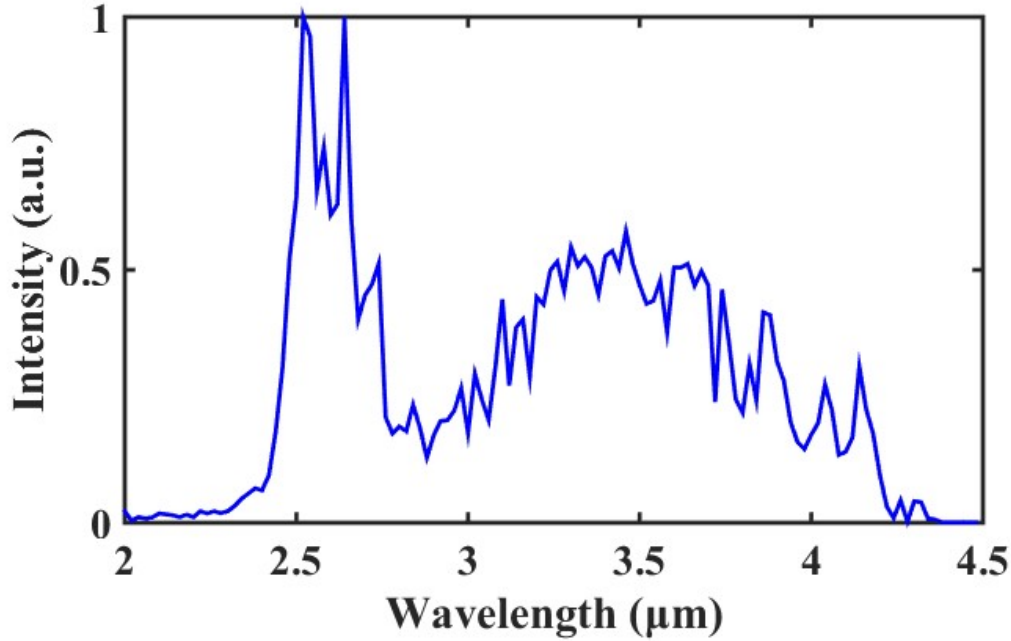
Figure 6.6 The SC spectrum generated from 6-mm-thick BaF_2, which serves as the signal of the mid-IR OPA, measured using 2.4 μm LPF and InF_3 fiber with 300-μm core diameter.

By carefully optimizing the crystal angle, temporal and spatial overlaps between the pump and the signal. An ultra-broadband idler spectrum is obtained. Its spectrum spans from 4.2 to 16 μm, with the -3 dB bandwidth ranging from 4.5 to 13.3 μm, shown in Figure 6.7(a). The spectrum is broader than the spectrum via IPDFG driven at 3 μm, as predicted by the phase-matching function in Figure 6.2(a). It is also much broader than the reported parametric sources based on other nonlinear crystals such as CSP [66], AGS [142, 143], AGSe [128, 147] and ZGP [72, 73]. It should be noted that the 4.5 μm LPF is responsible for the steep edge at ~4.6 μm. The distance from the OPA output to the detector of the monochromator is ~3 m, thus some fine structures caused by the atmospheric absorption appear in the spectrum. Similar absorption structures have been reported in the broadband mid-IR systems [165, 166]. In addition, the SC components in the range of 2.5-3 μm are located in the water absorption window. These absorption structures are transferred to the 7-

15 μm idler spectrum during the parametric amplification, which also contributes to the fine structures of the idler spectrum. A vacuum or nobel gas purging chamber could be used to remove these spectral structures [129]. The signal spectrum in Figure 6.7(b) shows a non-zero intensity, indicating the signal and idler spectrum overlap in frequency domain.
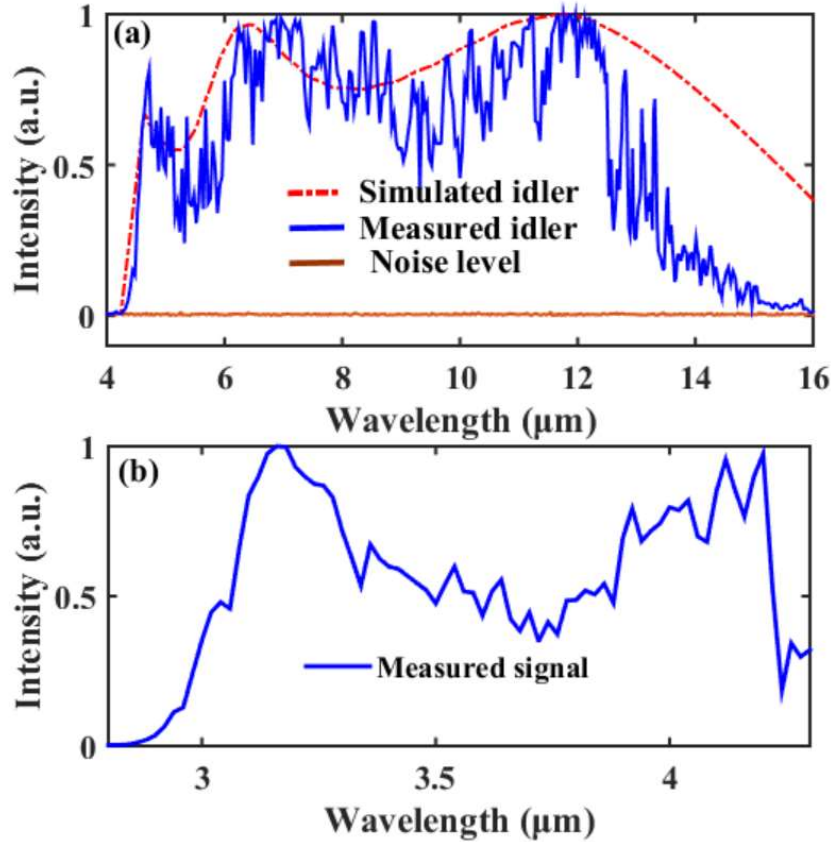
Figure 6.7 (a) The measured (solid blue, 20 nm resolution) and simulated (dashed red) spectra of the idler pulses. (b) The spectrum of amplified signal pulses. Note that the measured spectra are calibrated by taking into account the response curves of the grating, MCT, LPF and the hollow-core fiber. The simulated idler spectrum includes the edge response of the LPF. The short-wavelength side of the signal spectrum is cut by the transmission of the hollow-core fiber.

The OPA process is further investigated using a (2+1)-dimensional numerical simulation code introduced in Chapter 5. Taking into account the high pump intensity and the large nonlinear refractive index of GaSe ($n_2 = 450 \times 10^{-1}$ cm^2/W) [134], the SPM and self-focusing are included in the calculations, which are found crucial for reproducing the measured spectrum. A 2.15 μm, 300 μJ, 50 fs chirped Gaussian pump pulse with a spectrum spanning from 1.8 to 2.3 μm,

and a 2.84 μm, 3 nJ, 50 fs chirped signal with a spectral shape similar to the measured SC covering 2.3 to 4.3 μm are employed in the simulation to mimic the experimental conditions. The PM angle is set to 11.15°. The simulated idler spectrum is shown in Figure 6.7(a) which qualitatively match with the measured idler. The mismatch for idler spectrum at > 13 μm is due to the crystal absorption [167].

In order to further verify the accuracy of the measured idler spectrum, we integrate the measured spectrum and calculate the energy distribution in different spectral bands, i.e. 4.2-7.3 μm, 7.3-11.3 μm, and 11.3-16 μm, based on the measured idler pulse energy. We compare the integrated pulse energies with the measured, as shown in Figure 6.8(a). The good agreement between the integrated and measured pulse energy gives a direct evidence for the accuracy of the spectrum measurement. Based on the idler spectrum, the calculated TL pulse width is ~19 fs (Figure 6.8(b)), which corresponds to 0.65-cycle pulse width, centered at 8.8 μm. The actual pulse width could be broadened to few cycles due to the dispersion from the 1 mm thick 4.5 μm LPF (Ge substrate) and the intrinsic dispersion from the OPA. It is worth noting that as the signal and the pump are from the same TOPAS pump system, the CEP fluctuation in the idler pulse is self-canceled through the DFG nature of the OPA [88]. Recently, stable CEP of the idler pulse from a passively CEP stable mid-IR OPA has been experimentally confirmed [66]. Thus, we, to the large extent, believe that the CEP for this system is stable. Its CEP stability could be degraded by some factors such as the intensity-to-phase noise of the pump, and the temporal jitters between the pump and the signal [88].
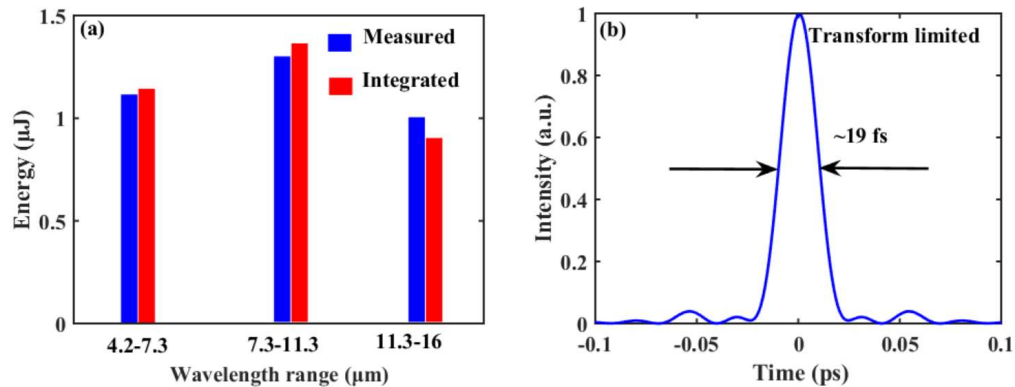
Figure 6.8 (a) The measured and integrated energy distribution in different bands of the idler wavelength. (b) The calculated TL pulse width based on the measured idler spectrum.

The pulse energy of the generated idler is measured as ~3.4 μJ behind a 4.5 μm LPF, with ~300 μJ pump energy. Considering the 85% transmission of the LPF and ~71% reflection from the silicon beam splitter for the idler pulses, ~2% conversion efficiency from the pump to the idler is achieved. For this OPA system, the measured OPA output by blocking the signal is ~0.12 μJ, and the energy fluctuation of the generated idler pulses is 2.8% rms for a measurement duration of 30 minutes. In addition, the idler pulse energies with different LPFs as a function of the pump energy are measured, shown in Figure 6.9. No saturation occurs at the maximum pump energy, which implies further energy scaling up is possible with higher pump energy. The idler beam profile behind the 4.5 μm LPF are also measured, exhibiting a good Gaussian profile shown in the inset of Figure 6.9.
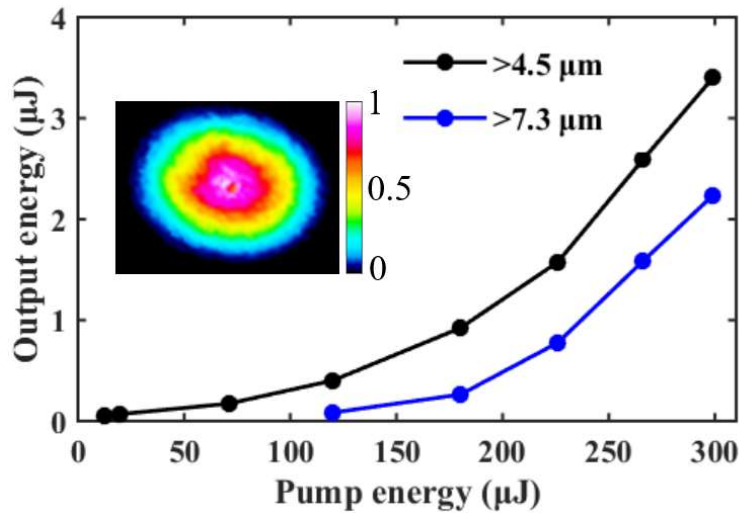
Figure 6.9 The dependence of the idler pulse energy on the pump energy behind the 4.5 and 7.3 μm LPFs. The inset is the beam profile of the idler pulse behind the 4.5 μm LPF at the output energy of ~3.4 μJ.

6.4 Conclusions

In conclusions, we demonstrate a GaSe-based OPA system driven by a 2 μm driving source and seeded by a SC spectrum. 3.4 μJ ultra-broadband mid-IR pulses with a spectrum spanning from 4.5 to 13.3 μm at –3 dB and from 4.2 to 16 μm in the full spectral range and a conversion efficiency of 2% from the 2 μm pulses to idler pulses are generated. To the best of our knowledge, this is the broadest spectrum ever obtained by OPA systems in this wavelength region. With the rapid

progress of ~2 μm Ho:YLF or Ho:YAG CPA systems, the energy scaling up of the ultra-broadband mid-IR pulses is expected through the development of the GaSe-based OPCPA systems.

Chapter 7 Summary and future work

7.1 Summary

In this thesis, we have studied that high-power, high-energy, broadband, few-cycle mid-IR pulse generation with a wavelength of >3 μm and a kHz repetition rate using OPCPA, IPDFG and OPA methods. Some significant efforts have also been made in nonlinear pulse compression, HHG and SCG using the developed high-power, high-energy, broadband, few-cycle mid-IR sources. We summarize our works in the following.

We design and present a CEP-stable 3 μm OPCPA system based on PPLN and PPSLT crystals, pumped by a 120 W, 12 mJ, 1 ps, 1030 nm Innoslab Yb:YAG laser at a 10 kHz repetition rate. 3 μm pulses with a 3 W average power, a 300 μJ pulse energy, and a 61 fs pulse width are delivered. To the best of our knowledge, this is the first time that PPLST crystals are used in a 3 μm OPCPA system. In order to obtain the shorter pulses, a bulk YAG crystal is employed to further nonlinearly compress the 3 μm pulses to 21 fs corresponding to two-cycle pulse width, with an 83% compression efficiency. Driven by the high-energy, high-power, 3 μm nonlinearly compressed pulses, HHG with up to the 15th order is generated in a ZnO crystal. Compared with HHG driven by 3 μm pulses before nonlinear pulse compression, one order of magnitude enhancement of the harmonic intensity is demonstrated, which reveals the significance of the intensity enhancement of the driving source.

To further extend the spectrum to the long-wavelength mid-IR region, we use the SPM effect in GaSe to generate an internal signal of IPDFG and report a broadband, > 6 μm, SPM-assisted mid-IR IPDFG directly driven by 3 μm pulses from the OPCPA system we developed, without the use of the extra nonlinear spectral broadening stage. The IPDFG pulses have a 7-15 μm spectral span, 0.91 μJ pulse energy, and 9.1 mW output power. The contribution of the driving pulse spectral broadening via SPM in the process of IPDFG is confirmed experimentally. The generated IPDFG pulses are compressed to 1.8-cycle (60 fs) pulse width by adding extra bulk materials. The good compressibility of the IPDFG pulses verifies the IPDFG pulses have the good spectral coherence.

By nonlinear pulse compression of 3 μm OPCPA pulses in YAG, the spectrum of 3 μm pulses is broadened to 4.5 μm. An external signal of IPDFG is produced. Using such pulses, we boost the

efficiency of IPDFG to a record value of up to 5.3%. 5 μJ, 50 mW, 68 fs corresponding to 2.1 cycles centered at 9.7 μm IPDFG pulses with a spectrum spanning from 6 to 13.2 μm are obtained from a GaSe crystal. With a focal spot of 70 μm, the field strength of the IPDFG pulses can exceed 0.27 V/Å, enabling the applications in the nonlinear optics in solid materials. As a demonstration, pumped by the IPDFG output, a 2.4 μJ, 24 mW SC with a 3-octave bandwidth covering 2 to 16 μm and a 2.7 μJ, 27 mW SC with a 2.3-octave bandwidth covering 3 to 14.5 μm are generated in a KRS-5 crystal and a ZnSe crystal, respectively. Both SC spectra support sub-cycle pulse widths. Thus, sub-cycle pulses are expected. Such sub-cycle pulses open a way for the electron microscopy with ultimate temporal and spatial resolution besides the spectroscopy.

In above works, we report the generation of two-cycle mid-IR pulses with a broadband spectrum from 6 to 15 μm and a uJ-level pulse energy, using an IPDFG method. Further, we explore the mid-IR pulse generation with a broader spectrum supporting sub-cycle pulse width using an OPA method. We report a GaSe-based OPA system driven at 2 μm and seeded by SC pulses. Benefitting from the good phase-matching bandwidth of GaSe at 2 μm, the idler spectrum covers 4.2-16 μm with a 3 dB bandwidth from 4.5 to 13.3 μm, which, to the best of our knowledge, is broadest in reported OPA sources. Combined with ~3.4 μJ pulse energy, the OPA source has a potential in molecular spectroscopy and some strong-field experiments in solids.

7.2 Future work

In future, some upgraded works will be done, such as further boosting the energy of the 3 μm OPCPA system to > 1 mJ using a more powerful 1 μm driving source. Based on the 3 μm pulses with higher energy, the specs of broadband IPDFG sources are improved accordingly. In addition, we have explored HHG in a solid using 3 μm pulses from the OPCPA system and SCG in bulk crystals using the 9.7 μm pulses from the IPDFG source. In the future, more applications will be explored using the current sources or the upgraded sources. For example, we can develop the table-top water window soft X-ray source via HHG in gases using the 255 μJ, 21 fs, 10 kHz, 3 μm mid-IR pulses we have developed. Recently, 250 μJ, 16.5 fs, 100 kHz, 2.2 μm pulses were reported for soft X-ray generation with a photon energy of up to 0.6 keV in He gas [79]. Our mid-IR source provides the similar peak intensity, but a longer driving wavelength. Therefore, it has a potential to generate the soft X-ray with a photon energy of > 0.6 keV. By improving the pulse energy of 3

μm pulses to > 1mJ, we can even pursue > 1 keV soft-ray and attosecond pulses. The developed IPDFG source with a spectrum from 6 to 13.2 μm and a 5 μJ pulse energy or the SCG source with a spectrum from 2 to 16 μm and a 2.4 μJ pulse energy will be applied in the frequency-resolved spectroscopy, time-resolved spectroscopy, ultrafast electron diffraction and so on. Especially, the IPDFG pulses have the intrinsic CEP stability. Combined with 10-fs-scale sampling pulses which could be produced by the ~1ps, 1030 nm pulses via filamentation, the IPDFG pulses can benefit many time-resolved studies [15, 168].

Publication lists

Journal papers

1. **K. Liu,** H. Li, S. Qu, H. Liang, Q. J. Wang and Y. Zhang, "20 W, 2 mJ, sub-ps, 258 nm all-solid-state deep-ultraviolet laser with up to 3 GW peak power," Optics Express 28(12), 18360-18367 (2020).

2. S. Chen, Y. Chen, **K. Liu,** R. Sidharthan, H. Li, C. J. Chang, Q. J. Wang, D. Tang and S. Yoo, "All-fiber short-wavelength tunable mode-locked fiber laser using normal dispersion thulium-doped fiber," Optics Express 28(12), 17570-17580 (2020).

3. S. Qu, G. C. Nagar, W. Li, **K. Liu**, X. Zou, S. H. Luen, D. Dempsey, K.-H. Hong, Q. J. Wang and Y. Zhang, "Long-wavelength-infrared laser filamentation in solids in the near-single-cycle regime," Optics Letters **45**(8), 2175-2178 (2020).

4. **K. Liu**, H. Liang, S. Qu, W. Li, X. Zou, Y. Zhang and Q. J. Wang, "High-energy mid-infrared intrapulse difference-frequency generation with 5.3% conversion efficiency driven at 3 μm," Optics Express **27**(26), 37706-37713 (2019).

5. Y. Chen, S. Chen, R. Sidharthan, C. J. Cheng, **K. Liu**, S. Rao, O. Bang, Q. Wang, D. Tang and S. Yoo, "High Energy Ultrafast Laser at 2 μm Using Dispersion Engineered Thulium-Doped Fiber," IEEE Photonics Journal **11**(6), 1-12 (2019).

6. **K. Liu**, H. Liang, W. Li, X. Zou, S. Qu, T. Lang, Y. Zhang and Q. J. Wang, "Microjoule Sub-Two-Cycle Mid-Infrared Intrapulse-DFG Driven by 3-μm OPCPA," IEEE Photonics Technology Letters **31**(21), 1741-1744 (2019).

7. X. Zou, W. Li, H. Liang, **K. Liu**, S. Qu, Q. J. Wang and Y. Zhang, "300 μJ, 3 W, few-cycle, 3 μm OPCPA based on periodically poled stoichiometric lithium tantalate crystals," Optics Letters **44**(11), 2791-2794 (2019).

8. S. Qu, H. Liang, **K. Liu**, X. Zou, W. Li, Q. J. Wang and Y. Zhang, "9 μm few-cycle optical parametric chirped-pulse amplifier based on LiGaS 2," Optics Letters **44**(10), 2422-2425 (2019).

9. X. Zou, H. Liang, S. Qu, **K. Liu**, C. Liu, Q. J. Wang and Y. Zhang, "High-energy single-cycle pulse generation in a parametric amplifier with the optimized angular dispersion," Applied Physics B **125**(3), 36 (2019).

10. **K. Liu**, H. Liang, L. Wang, S. Qu, T. Lang, H. Li, Q. J. Wang and Y. Zhang, "Multimicrojoule GaSe-based midinfrared optical parametric amplifier with an ultrabroad idler spectrum covering 4.2–16 μm," Optics Letters **44**(4), 1003-1006 (2019).

11. B. Sun, J. Luo, Z. Yan, **K. Liu**, J. Ji, Y. Zhang, Q. J. Wang and X. Yu, "1867–2010 nm tunable femtosecond thulium-doped all-fiber laser," Optics Express **25**(8), 8997-9002 (2017).

12. M. Mohammadzadeh, S. R. Gonzalez-Avila, **K. Liu**, Q. J. Wang and C.-D. Ohl, "Synthetic jet generation by high-frequency cavitation," Journal of Fluid Mechanics **823**((2017).

Conference papers

13. **K. Liu**, H. Liang, W. Li, X. Zou, S. Qu, T. Lang, Q. J. Wang, and Y. Zhang, "Microjoule sub-three-cycle long-wavelength intrapulse difference frequency generation driven at 3 μm," in Laser Congress 2019 (ASSL, LAC, LS&C), OSA Technical Digest (Optical Society of America, 2019), paper JTh3A.29.

14. S. Qu, X. Zou, **K. Liu**, W. Li, S. H. Luen, Q. J. Wang, Y. Zhang, and H. Liang, "Micro-joule, 10 kHz, sub-two-cycle, long wavelength mid-infrared laser source based on the 9 μm OPCPA," in Laser Congress 2019 (ASSL, LAC, LS&C), OSA Technical Digest (Optical Society of America, 2019), paper AM2A.6.

15. X. Zou, W. Li, H. Liang, S. Qu, **K. Liu**, Q. J. Wang, and Y. Zhang, "Sub-milijoule, 3 μm optical parametric chirped-pulse amplifier at 10 kHz repetition rate," in Conference on Lasers and Electro-Optics, OSA Technical Digest (Optical Society of America, 2019), paper FTh1B.5.

16. S. Qu, H. Liang, X. Zou, **K. Liu**, W. Li, Q. Wang, and Y. Zhang, "High-energy 9 μm LiGaS2-based Optical Parametric Chirped-Pulse Amplifier," in Conference on Lasers and Electro-Optics, OSA Technical Digest (Optical Society of America, 2019), paper JW2A.40.

17. **K. Liu**, H. Liang, L. Wang, S. Qu, H. Li, Q. J. Wang, and Y. Zhang, "Multi-μJ 8.8 μm, Mid-infrared Laser with a Flat Spectrum Supporting Sub-cycle Pulses from a GaSe-based Optical Parametric Amplifier," in Laser Congress 2018 (ASSL), OSA Technical Digest (Optical Society of America, 2018), paper AW4A.4.

18. X. Zou, S. Qu, **K. Liu**, Q. Wang, H. Liang, and Y. Zhang, "Three-fold efficiency improvement via temporal and spatial pulse shaping in 3μm OPCPA," in 2017 Conference on Lasers and Electro-Optics Pacific Rim, (Optical Society of America, 2017), paper s2252.

References

1. W. Herschel, "Experiments on the Refrangibility of the Invisible Rays of the Sun," Philosophical Transactions of the Royal Society of London (90), 284-292 (1800).

2. G. R. Hunt and J. W. Salisbury, "Lunar surface features: mid-infrared spectral observations," Science **146**(3644), 641-642 (1964).

3. J. R. P. Angel, A. Cheng and N. Woolf, "A space telescope for infrared spectroscopy of Earth-like planets," Nature **322**(6077), 341-343 (1986).

4. D. Popa and F. Udrea, "Towards integrated mid-infrared gas sensors," Sensors **19**(9), 2076 (2019).

5. T. Schmid, "Photoacoustic spectroscopy for process analysis," Analytical and Bioanalytical Chemistry **384**(5), 1071-1086 (2006).

6. C. S. Goldenstein, R. M. Spearrin, J. B. Jeffries and R. K. Hanson, "Infrared laser-absorption sensing for combustion gases," Progress in Energy and Combustion Science **60**(132-176 (2017).

7. U. Willer, M. Saraji, A. Khorsandi, P. Geiser and W. Schade, "Near-and mid-infrared laser monitoring of industrial processes, environment and security applications," Optics and Lasers in Engineering **44**(7), 699-710 (2006).

8. M. Metsälä, "Optical techniques for breath analysis: from single to multi-species detection," Journal of Breath Research **12**(2), 027104 (2018).

9. A. Schieweck, E. Uhde, T. Salthammer, L. C. Salthammer, L. Morawska, M. Mazaheri and P. Kumar, "Smart homes and the control of indoor air quality," Renewable and Sustainable Energy Reviews **94**(705-718 (2018).

10. A. Ortiz Perez, B. Bierer, L. Scholz, J. Wöllenstein and S. Palzer, "A wireless gas sensor network to monitor indoor environmental quality in schools," Sensors **18**(12), 4345 (2018).

11. Griffiths, P. R. & de Haseth, J. A. Fourier Transform Infrared Spectrometry 2nd edn (Wiley, Hoboken, NJ, 2007).

12. A. Schliesser, N. Picqué and T. W. Hänsch, "Mid-infrared frequency combs," Nature Photonics **6**(7), 440-449 (2012).

13. F. Keilmann, C. Gohle and R. Holzwarth, "Time-domain mid-infrared frequency-comb spectrometer," Optics Letters **29**(13), 1542-1544 (2004).

14. P. Maslowski, K. F. Lee, A. C. Johansson, A. Khodabakhsh, G. Kowzan, L. Rutkowski, A. A. Mills, C. Mohr, J. Jiang and M. E. Fermann, "Surpassing the path-limited resolution of Fourier-transform spectrometry with frequency combs," Physical Review A **93**(2), 021802 (2016).

15. I. Pupeza, M. Huber, M. Trubetskov, W. Schweinberger, S. A. Hussain, C. Hofer, K. Fritsch, M. Poetzlberger, L. Vamos and E. Fill, "Field-resolved infrared spectroscopy of biological systems," Nature **577**(7788), 52-59 (2020).

16. T. Popmintchev, M.-C. Chen, D. Popmintchev, P. Arpin, S. Brown, S. Ališauskas, G. Andriukaitis, T. Balčiunas, O. D. Mücke and A. Pugzlys, "Bright coherent ultrahigh harmonics in the keV x-ray regime from mid-infrared femtosecond lasers," Science **336**(6086), 1287-1291 (2012).

17. M. Wu, S. Ghimire, D. A. Reis, K. J. Schafer and M. B. Gaarde, "High-harmonic generation from Bloch electrons in solids," Physical Review A **91**(4), 043839 (2015).

18. T. T. Luu, M. Garg, S. Y. Kruchinin, A. Moulet, M. T. Hassan and E. Goulielmakis, "Extreme ultraviolet high-harmonic spectroscopy of solids," Nature **521**(7553), 498-502 (2015).

19. I. V. Schweigert and S. Mukamel, "Coherent ultrafast core-hole correlation spectroscopy: X-ray analogues of multidimensional NMR," Physical Review Letters **99**(16), 163001 (2007).

20. E. Seres, J. Seres and C. Spielmann, "X-ray absorption spectroscopy in the keV range with laser generated high harmonic radiation," Applied Physics Letters **89**(18), 181919 (2006).

21. W. Li, A. A. Jaroń-Becker, C. W. Hogle, V. Sharma, X. Zhou, A. Becker, H. C. Kapteyn and M. M. Murnane, "Visualizing electron rearrangement in space and time during the transition from a molecule to atoms," Proceedings of the National Academy of Sciences **107**(47), 20219-20222 (2010).

22. G. Doumy, J. Wheeler, C. Roedig, R. Chirla, P. Agostini and L. DiMauro, "Attosecond synchronization of high-order harmonics from midinfrared drivers," Physical Review Letters **102**(9), 093002 (2009).

23. J. Li, X. Ren, Y. Yin, K. Zhao, A. Chew, Y. Cheng, E. Cunningham, Y. Wang, S. Hu and Y. Wu, "53-attosecond X-ray pulses reach the carbon K-edge," Nature Communications **8**(1), 1-5 (2017).

24. P. á. Corkum and F. Krausz, "Attosecond science," Nature Physics **3**(6), 381-387 (2007).

25. J. Weisshaupt, V. Juvé, M. Holtz, S. Ku, M. Woerner, T. Elsaesser, S. Ališauskas, A. Pugžlys and A. Baltuška, "High-brightness table-top hard X-ray source driven by sub-100-femtosecond mid-infrared pulses," Nature Photonics **8**(12), 927-930 (2014).

26. R. Toth, J. Kieffer, S. Fourmaux, T. Ozaki and A. Krol, "In-line phase-contrast imaging with a laser-based hard x-ray source," Review of Scientific Instruments **76**(8), 083701 (2005).

27. D. Boschetto, G. Mourou, A. Rousse, A. Mordovanakis, B. Hou, J. Nees, D. Kumah and R. Clarke, "Spatial coherence properties of a compact and ultrafast laser-produced plasma keV x-ray source," Applied Physics Letters **90**(1), 011106 (2007).

28. C. Bressler and M. Chergui, "Ultrafast X-ray absorption spectroscopy," Chemical Reviews **104**(4), 1781-1812 (2004).

29. M. Bargheer, N. Zhavoronkov, M. Woerner and T. Elsaesser, "Recent progress in ultrafast X-ray diffraction," Chemphyschem: A European Journal of Chemical Physics and Physical Chemistry **7**(4), 783-792 (2006).

30. E. A. Nanni, W. R. Huang, K.-H. Hong, K. Ravi, A. Fallahi, G. Moriena, R. D. Miller and F. X. Kärtner, "Terahertz-driven linear electron acceleration," Nature Communications **6**(1), 1-8 (2015).

31. D. Woodbury, L. Feder, V. Shumakova, C. Gollner, R. Schwartz, B. Miao, F. Salehi, A. Korolov, A. Pugžlys and A. Baltuška, "Laser wakefield acceleration with mid-IR laser pulses," Optics Letters **43**(5), 1131-1134 (2018).

32. C. I. Blaga, J. Xu, A. D. DiChiara, E. Sistrunk, K. Zhang, P. Agostini, T. A. Miller, L. F. DiMauro and C. Lin, "Imaging ultrafast molecular dynamics with laser-induced electron diffraction," Nature **483**(7388), 194-197 (2012).

33. O. Schubert, M. Hohenleutner, F. Langer, B. Urbanek, C. Lange, U. Huttner, D. Golde, T. Meier, M. Kira and S. W. Koch, "Sub-cycle control of terahertz high-harmonic generation by dynamical Bloch oscillations," Nature Photonics **8**(2), 119-123 (2014).

34. R. Huber, F. Tauser, A. Brodschelm, M. Bichler, G. Abstreiter and A. Leitenstorfer, "How many-particle interactions develop after ultrafast excitation of an electron–hole plasma," Nature **414**(6861), 286-289 (2001).

35. M. Kozák, J. McNeur, K. J. Leedle, H. Deng, N. Schönenberger, A. Ruehl, I. Hartl, J. Harris, R. Byer and P. Hommelhoff, "Optical gating and streaking of free electrons with sub-optical cycle precision," Nature Communications **8**(1), 1-7 (2017).

36. K. E. Priebe, C. Rathje, S. V. Yalunin, T. Hohage, A. Feist, S. Schäfer and C. Ropers, "Attosecond electron pulse trains and quantum state reconstruction in ultrafast transmission electron microscopy," Nature Photonics **11**(12), 793-797 (2017).

37. M. Kozák, N. Schönenberger and P. Hommelhoff, "Ponderomotive generation and detection of attosecond free-electron pulse trains," Physical Review Letters **120**(10), 103203 (2018).

38. D. R. Austin, K. R. Kafka, Y. H. Lai, Z. Wang, K. Zhang, H. Li, C. I. Blaga, A. Y. Yi, L. F. DiMauro and E. A. Chowdhury, "High spatial frequency laser induced periodic surface structure formation in germanium by mid-IR femtosecond pulses," Journal of Applied Physics **120**(14), 143103 (2016).

39. D. C. Fernandez, R. Bhargava, S. M. Hewitt and I. W. Levin, "Infrared spectroscopic imaging for histopathologic recognition," Nature Biotechnology **23**(4), 469-474 (2005).

40. S. Junaid, S. C. Kumar, M. Mathez, M. Hermes, N. Stone, N. Shepherd, M. Ebrahim-Zadeh, P. Tidemand-Lichtenberg and C. Pedersen, "Video-rate, mid-infrared hyperspectral upconversion imaging," Optica **6**(6), 702-708 (2019).

41. N. M. Israelsen, C. R. Petersen, A. Barh, D. Jain, M. Jensen, G. Hannesschläger, P. Tidemand-Lichtenberg, C. Pedersen, A. Podoleanu and O. Bang, "Real-time high-resolution mid-infrared optical coherence tomography," Light: Science & Applications **8**(1), 1-13 (2019).

42. E. Ippen, C. Shank and A. Dienes, "Passive mode locking of the cw dye laser," Applied Physics Letters **21**(8), 348-350 (1972).

43. Y. Chu, X. Liang, L. Yu, Y. Xu, L. Xu, L. Ma, X. Lu, Y. Liu, Y. Leng and R. Li, "High-contrast 2.0 Petawatt Ti: sapphire laser system," Optics Express **21**(24), 29231-29239 (2013).

44. W. Li, Z. Gan, L. Yu, C. Wang, Y. Liu, Z. Guo, L. Xu, M. Xu, Y. Hang and Y. Xu, "339 J high-energy Ti: sapphire chirped-pulse amplifier for 10 PW laser facility," Optics Letters **43**(22), 5681-5684 (2018).

45. C. Teisset, M. Schultze, R. Bessing, M. Haefner, S. Prinz, D. Sutter, and T. Metzger, "300 W picosecond thin-disk regenerative amplifier at 10 kHz repetition rate," in Advanced Solid-State Lasers Congress Postdeadline, OSA Postdeadline Paper Digest (online) (Optical Society of America, 2013), paper JTh5A.1.

46. M. Schultze, C. Teisset, S. Prinz, D. Sutter, K. Michel and T. Metzger, "Highly-efficient, optically synchronized thin disk amplifier for pumping OPCPA at high repetition rates between 100–300 kHz," Solid State Lasers XXIII: Technology and Devices (2014).

47. T. Nubbemeyer, M. Kaumanns, M. Ueffing, M. Gorjan, A. Alismail, H. Fattahi, J. Brons, O. Pronin, H. G. Barros and Z. Major, "1 kW, 200 mJ picosecond thin-disk laser system," Optics Letters **42**(7), 1381-1384 (2017).

48. M. Müller, A. Klenke, A. Steinkopff, H. Stark, A. Tünnermann and J. Limpert, "3.5 kW coherently combined ultrafast fiber laser," Optics Letters **43**(24), 6037-6040 (2018).

49. T. Nagy, S. Hädrich, P. Simon, A. Blumenstein, N. Walther, R. Klas, J. Buldt, H. Stark, S. Breitkopf and P. Jójárt, "Generation of three-cycle multi-millijoule laser pulses at 318 W average power," Optica **6**(11), 1423-1424 (2019).

50. P. Balla, A. B. Wahid, I. Sytcevich, C. Guo, A.-L. Viotti, L. Silletti, A. Cartella, S. Alisauskas, H. Tavakol and U. Grosse-Wortmann, "Postcompression of picosecond pulses into the few-cycle regime," Optics Letters **45**(9), 2572-2575 (2020).

51. J. Zhang, K. F. Mak and O. Pronin, "Kerr-lens mode-locked 2-μm thin-disk lasers," IEEE Journal of Selected Topics in Quantum Electronics **24**(5), 1-11 (2018).

52. J. Zhang, F. Schulze, K. F. Mak, V. Pervak, D. Bauer, D. Sutter and O. Pronin, "High-power, high-efficiency Tm: YAG and Ho: YAG thin-disk lasers," Laser & Photonics Reviews **12**(3), 1700273 (2018).

53. M. Hemmer, D. Sánchez, M. Jelínek, V. Smirnov, H. Jelinkova, V. Kubeček and J. Biegert, "2-μm wavelength, high-energy Ho: YLF chirped-pulse amplifier for mid-infrared OPCPA," Optics Letters **40**(4), 451-454 (2015).

54. U. Elu, T. Steinle, D. Sánchez, L. Maidment, K. Zawilski, P. Schunemann, U. Zeitner, C. Simon-Boisson and J. Biegert, "Table-top high-energy 7 μm OPCPA and 260 mJ Ho: YLF pump laser," Optics Letters **44**(13), 3194-3197 (2019).

55. N. Nagl, S. Gröbmeyer, V. Pervak, F. Krausz, O. Pronin and K. F. Mak, "Directly diode-pumped, Kerr-lens mode-locked, few-cycle Cr: ZnSe oscillator," Optics Express **27**(17), 24445-24454 (2019).

56. Y. Wu, F. Zhou, E. W. Larsen, F. Zhuang, Y. Yin and Z. Chang, "Generation of few-cycle multi-millijoule 2.5 μm pulses from a single-stage Cr 2+: ZnSe amplifier," Scientific Reports **10**(1), 1-7 (2020).

57. E. Migal, A. Pushkin, B. Bravy, V. Gordienko, N. Minaev, A. Sirotkin and F. Potemkin, "3.5-mJ 150-fs Fe: ZnSe hybrid mid-IR femtosecond laser at 4.4 μm for driving extreme nonlinear optics," Optics Letters **44**(10), 2550-2553 (2019).

58. A. Pushkin, E. Migal, S. Tokita, Y. V. Korostelin and F. Potemkin, "Femtosecond graphene mode-locked Fe: ZnSe laser at 4.4 μm," Optics Letters **45**(3), 738-741 (2020).

59. P. Corkum, "High-power, subpicosecond 10-μm pulse generation," Optics Letters **8**(10), 514-516 (1983).

60. P. Corkum, "Amplification of picosecond 10 μm pulses in multiatmosphere CO_2 lasers," IEEE Journal of Quantum Electronics **21**(3), 216-232 (1985).

61. G. Steinmeyer and J. S. Skibina, "Entering the mid-infrared," Nature Photonics **8**(11), 814-815 (2014).

62. Y. Yao, A. J. Hoffman and C. F. Gmachl, "Mid-infrared quantum cascade lasers," Nature Photonics **6**(7), 432-439 (2012).

63. D. Oepts, A. Van der Meer and P. Van Amersfoort, "The free-electron-laser user facility FELIX," Infrared Physics & Technology **36**(1), 297-308 (1995).

64. T. Kawasaki, T. Yaji, T. Ohta and K. Tsukiyama, "Application of mid-infrared free-electron laser tuned to amide bands for dissociation of aggregate structure of protein," Journal of Synchrotron Radiation **23**(1), 152-157 (2016).

65. V. Smolski, S. Vasilyev, I. Moskalev, M. Mirov, A. Muraviev, S. Mirov, K. Vodopyanov, and V. Gapontsev, "Sub-Watt Femtosecond Laser Source with the Spectrum Spanning 3–8 μm," Advanced Solid State Lasers (Optical Society of America, 2017), paper AM4A.6.

66. H. Liang, P. Krogen, Z. Wang, H. Park, T. Kroh, K. Zawilski, P. Schunemann, J. Moses, L. F. DiMauro and F. X. Kärtner, "High-energy mid-infrared sub-cycle pulse synthesis from a parametric amplifier," Nature Communications **8**(1), 1-9 (2017).

67. F. Junginger, A. Sell, O. Schubert, B. Mayer, D. Brida, M. Marangoni, G. Cerullo, A. Leitenstorfer and R. Huber, "Single-cycle multiterahertz transients with peak fields above 10 MV/cm," Optics Letters **35**(15), 2645-2647 (2010).

68. T. Butler, D. Gerz, C. Hofer, J. Xu, C. Gaida, T. Heuermann, M. Gebhardt, L. Vamos, W. Schweinberger and J. Gessner, "Watt-scale 50-MHz source of single-cycle waveform-stable pulses in the molecular fingerprint region," Optics Letters **44**(7), 1730-1733 (2019).

69. J. Zhang, K. F. Mak, N. Nagl, M. Seidel, D. Bauer, D. Sutter, V. Pervak, F. Krausz and O. Pronin, "Multi-mW, few-cycle mid-infrared continuum spanning from 500 to 2250 cm^{-1}," Light: Science & Applications **7**(2), 17180-17180 (2018).

70. K.-H. Hong, C.-J. Lai, J. P. Siqueira, P. Krogen, J. Moses, C.-L. Chang, G. J. Stein, L. E. Zapata and F. X. Kärtner, "Multi-mJ, kHz, 2.1 μm optical parametric chirped-pulse amplifier and high-flux soft x-ray high-harmonic generation," Optics Letters **39**(11), 3145-3148 (2014).

71. A. Mitrofanov, A. Voronin, D. Sidorov-Biryukov, S. Mitryukovsky, A. Fedotov, E. Serebryannikov, D. Meshchankin, V. Shumakova, S. Ališauskas and A. Pugžlys, "Subterawatt few-cycle mid-infrared pulses from a single filament," Optica **3**(3), 299-302 (2016).

72. M. Bock, L. von Grafenstein, U. Griebner and T. Elsaesser, "Generation of millijoule few-cycle pulses at 5 μm by indirect spectral shaping of the idler in an optical parametric chirped pulse amplifier," JOSA B **35**(12), C18-C24 (2018).

73. U. Elu, T. Steinle, D. Sánchez, L. Maidment, K. Zawilski, P. Schunemann, U. Zeitner, C. Simon-Boisson and J. Biegert, "Table-top high-energy 7 μm OPCPA and 260 mJ Ho: YLF pump laser," Optics Letters **44**(13), 3194-3197 (2019).

74. N. Bigler, J. Pupeikis, S. Hrisafov, L. Gallmann, C. R. Phillips and U. Keller, "High-power OPCPA generating 1.7 cycle pulses at 2.5 μm," Optics Express **26**(20), 26750-26757 (2018).

75. N. Thiré, R. Maksimenka, B. Kiss, C. Ferchaud, G. Gitzinger, T. Pinoteau, H. Jousselin, S. Jarosch, P. Bizouard and V. Di Pietro, "Highly stable, 15 W, few-cycle, 65 mrad CEP-noise mid-IR OPCPA for statistical physics," Optics Express **26**(21), 26907-26915 (2018).

76. M. Neuhaus, H. Fuest, M. Seeger, J. Schötz, M. Trubetskov, P. Russbueldt, H. Hoffmann, E. Riedle, Z. Major and V. Pervak, "10 W CEP-stable few-cycle source at 2 μm with 100 kHz repetition rate," Optics Express **26**(13), 16074-16085 (2018).

77. U. Elu, M. Baudisch, H. Pires, F. Tani, M. H. Frosz, F. Köttig, A. Ermolov, P. S. J. Russell and J. Biegert, "High average power and single-cycle pulses from a mid-IR optical parametric chirped pulse amplifier," Optica **4**(9), 1024-1029 (2017).

78. M. Mero, Z. Heiner, V. Petrov, H. Rottke, F. Branchi, G. M. Thomas and M. J. Vrakking, "43 W, 1.55 µm and 12.5 W, 3.1 µm dual-beam, sub-10 cycle, 100 kHz optical parametric chirped pulse amplifier," Optics Letters **43**(21), 5246-5249 (2018).

79. J. Pupeikis, P.-A. Chevreuil, N. Bigler, L. Gallmann, C. R. Phillips and U. Keller, "Water window soft x-ray source enabled by a 25 W few-cycle 2.2 µm OPCPA at 100 kHz," Optica **7**(2), 168-171 (2020).

80. Y. Nomura, H. Shirai, K. Ishii, N. Tsurumachi, A. A. Voronin, A. M. Zheltikov and T. Fuji, "Phase-stable sub-cycle mid-infrared conical emission from filamentation in gases," Optics Express **20**(22), 24741-24747 (2012).

81. C. R. Petersen, U. Møller, I. Kubat, B. Zhou, S. Dupont, J. Ramsay, T. Benson, S. Sujecki, N. Abdel-Moneim and Z. Tang, "Mid-infrared supercontinuum covering the 1.4–13.3 µm molecular fingerprint region using ultra-high NA chalcogenide step-index fibre," Nature Photonics **8**(11), 830-834 (2014).

82. T. Cheng, K. Nagasaka, T. H. Tuan, X. Xue, M. Matsumoto, H. Tezuka, T. Suzuki and Y. Ohishi, "Mid-infrared supercontinuum generation spanning 2.0 to 15.1 µm in a chalcogenide step-index fiber," Optics Letters **41**(9), 2117-2120 (2016).

83. V. V. Yakovlev, B. Kohler and K. R. Wilson, "Broadly tunable 30-fs pulses produced by optical parametric amplification," Optics Letters **19**(23), 2000-2002 (1994).

84. Boyd, Robert W. Nonlinear optics. Academic press, 2019.

85. C. Manzoni and G. Cerullo, "Design criteria for ultrafast optical parametric amplifiers," Journal of Optics **18**(10), 103501 (2016).

86. A. Siddiqui, G. Cirmi, D. Brida, F. Kärtner and G. Cerullo, "Generation of< 7 fs pulses at 800 nm from a blue-pumped optical parametric amplifier at degeneracy," Optics Letters **34**(22), 3592-3594 (2009).

87. A. Dubietis, G. Jonušauskas and A. Piskarskas, "Powerful femtosecond pulse generation by chirped and stretched pulse parametric amplification in BBO crystal," Optics Communications **88**(4-6), 437-440 (1992).

88. A. Baltuška, T. Fuji and T. Kobayashi, "Controlling the carrier-envelope phase of ultrashort light pulses with optical parametric amplifiers," Physical Review Letters **88**(13), 133901 (2002).

89. G. Cerullo, A. Baltuška, O. D. Muecke and C. Vozzi, "Few-optical-cycle light pulses with passive carrier-envelope phase stabilization," Laser & Photonics Reviews **5**(3), 323-351 (2011).

90. H. Fattahi, H. G. Barros, M. Gorjan, T. Nubbemeyer, B. Alsaif, C. Y. Teisset, M. Schultze, S. Prinz, M. Haefner and M. Ueffing, "Third-generation femtosecond technology," Optica **1**(1), 45-63 (2014).

91. X. Zou, W. Li, H. Liang, K. Liu, S. Qu, Q. J. Wang and Y. Zhang, "300 µJ, 3 W, few-cycle, 3 µm OPCPA based on periodically poled stoichiometric lithium tantalate crystals," Optics Letters **44**(11), 2791-2794 (2019).

92. B. Mayer, C. Phillips, L. Gallmann, M. Fejer and U. Keller, "Sub-four-cycle laser pulses directly from a high-repetition-rate optical parametric chirped-pulse amplifier at 3.4 µm," Optics Letters **38**(21), 4265-4268 (2013).

93. M. Mero, F. Noack, F. Bach, V. Petrov and M. J. Vrakking, "High-average-power, 50-fs parametric amplifier front-end at 1.55 µm," Optics Express **23**(26), 33157-33163 (2015).

94. M. Hemmer, A. Thai, M. Baudisch, H. Ishizuki, T. Taira and J. Biegert, "18-µJ energy, 160-kHz repetition rate, 250-MW peak power mid-IR OPCPA," Chinese Optics Letters **11**(1), 013202 (2013).

95. B. M. Luther, K. M. Tracy, M. Gerrity, S. Brown and A. T. Krummel, "2D IR spectroscopy at 100 kHz utilizing a Mid-IR OPCPA laser source," Optics Express **24**(4), 4117-4127 (2016).

96. R. Antipenkov, A. Varanavičius, A. Zaukevičius and A. Piskarskas, "Femtosecond Yb: KGW MOPA driven broadband NOPA as a frontend for TW few-cycle pulse systems," Optics Express **19**(4), 3519-3524 (2011).

97. Weber, Marvin J. Handbook of optical materials. CRC press, 2018.

98. L. Gallais and M. Commandré, "Laser-induced damage thresholds of bulk and coating optical materials at 1030 nm, 500 fs," Applied Optics **53**(4), A186-A196 (2014).

99. A. Couairon and A. Mysyrowicz, "Femtosecond filamentation in transparent media," Physics Reports **441**(2-4), 47-189 (2007).

100. R. R. Alfano, "The supercontinuum laser source," Springer (2016).

101. SNLO software: see the website http://www.as-photonics.com/snlo.

102. M. Baudisch, M. Hemmer, H. Pires and J. Biegert, "Performance of MgO: PPLN, KTA, and $KNbO_3$ for mid-wave infrared broadband parametric amplification at high average power," Optics Letters **39**(20), 5802-5805 (2014).

103. G. Andriukaitis, T. Balčiūnas, S. Ališauskas, A. Pugžlys, A. Baltuška, T. Popmintchev, M.-C. Chen, M. M. Murnane and H. C. Kapteyn, "90 GW peak power few-cycle mid-infrared pulses from an optical parametric amplifier," Optics Letters **36**(15), 2755-2757 (2011).

104. Y. Fu, B. Xue, K. Midorikawa and E. J. Takahashi, "TW-scale mid-infrared pulses near 3.3 μ m directly generated by dual-chirped optical parametric amplification," Applied Physics Letters **112**(24), 241105 (2018).

105. O. Chalus, A. Thai, P. Bates and J. Biegert, "Six-cycle mid-infrared source with 3.8 μJ at 100 kHz," Optics Letters **35**(19), 3204-3206 (2010).

106. N. Thiré, R. Maksimenka, B. Kiss, C. Ferchaud, P. Bizouard, E. Cormier, K. Osvay and N. Forget, "4-W, 100-kHz, few-cycle mid-infrared source with sub-100-mrad carrier-envelope phase noise," Optics Express **25**(2), 1505-1514 (2017).

107. T. Fuji, N. Ishii, C. Y. Teisset, X. Gu, T. Metzger, A. Baltuska, N. Forget, D. Kaplan, A. Galvanauskas and F. Krausz, "Parametric amplification of few-cycle carrier-envelope phase-stable pulses at 2.1 μm," Optics Letters **31**(8), 1103-1105 (2006).

108. J. Moses, S.-W. Huang, K.-H. Hong, O. Mücke, E. L. Falcão-Filho, A. Benedick, F. Ilday, A. Dergachev, J. Bolger and B. Eggleton, "Highly stable ultrabroadband mid-IR optical parametric chirped-pulse amplifier optimized for superfluorescence suppression," Optics Letters **34**(11), 1639-1641 (2009).

109. D. Brida, C. Manzoni, G. Cirmi, M. Marangoni, S. De Silvestri and G. Cerullo, "Generation of broadband mid-infrared pulses from an optical parametric amplifier," Optics Express **15**(23), 15035-15040 (2007).

110. T. Nagy, M. Kretschmar, M. J. Vrakking and A. Rouzée, "Generation of above-terawatt 1.5-cycle visible pulses at 1 kHz by post-compression in a hollow fiber," Optics Letters **45**(12), 3313-3316 (2020).

111. G. Fan, T. Balčiūnas, T. Kanai, T. Flöry, G. Andriukaitis, B. E. Schmidt, F. Légaré and A. Baltuška, "Hollow-core-waveguide compression of multi-millijoule CEP-stable 3.2 μm pulses," Optica **3**(12), 1308-1311 (2016).

112. M. Seo, K. Tsendsuren, S. Mitra, M. Kling and D. Kim, "High-contrast, intense single-cycle pulses from an all thin-solid-plate setup," Optics Letters **45**(2), 367-370 (2020).

113. V. Shumakova, P. Malevich, S. Ališauskas, A. Voronin, A. Zheltikov, D. Faccio, D. Kartashov, A. Baltuška and A. Pugžlys, "Multi-millijoule few-cycle mid-infrared pulses through nonlinear self-compression in bulk," Nature Communications **7**(1), 1-6 (2016).

114. S. Ghimire and D. A. Reis, "High-harmonic generation from solids," Nature Physics **15**(1), 10-16 (2019).

115. D. Golde, T. Meier and S. W. Koch, "High harmonics generated in semiconductor nanostructures by the coupled dynamics of optical inter-and intra-band excitations," Physical Review B **77**(7), 075330 (2008).

116. S. Ghimire, A. D. DiChiara, E. Sistrunk, U. B. Szafruga, P. Agostini, L. F. DiMauro and D. A. Reis, "Redshift in the optical absorption of ZnO single crystals in the presence of an intense midinfrared laser field," Physical Review Letters **107**(16), 167407 (2011).

117. H. Liu, Y. Li, Y. S. You, S. Ghimire, T. F. Heinz and D. A. Reis, "High-harmonic generation from an atomically thin semiconductor," Nature Physics **13**(3), 262-265 (2017).

118. Y. S. You, Y. Yin, Y. Wu, A. Chew, X. Ren, F. Zhuang, S. Gholam-Mirzaei, M. Chini, Z. Chang and S. Ghimire, "High-harmonic generation in amorphous solids," Nature Communications **8**(1), 1-5 (2017).

119. G. Vampa, T. Hammond, M. Taucer, X. Ding, X. Ropagnol, T. Ozaki, S. Delprat, M. Chaker, N. Thiré and B. Schmidt, "Strong-field optoelectronics in solids," Nature Photonics **12**(8), 465-468 (2018).

120. S. Ghimire, A. D. DiChiara, E. Sistrunk, P. Agostini, L. F. DiMauro and D. A. Reis, "Observation of high-order harmonic generation in a bulk crystal," Nature Physics **7**(2), 138-141 (2011).

121. Y. S. You, M. Wu, Y. Yin, A. Chew, X. Ren, S. Gholam-Mirzaei, D. A. Browne, M. Chini, Z. Chang and K. J. Schafer, "Laser waveform control of extreme ultraviolet high harmonics from solids," Optics Letters **42**(9), 1816-1819 (2017).

122. H. Kim, S. Han, Y. W. Kim, S. Kim and S.-W. Kim, "Generation of coherent extreme-ultraviolet radiation from bulk sapphire crystal," ACS Photonics **4**(7), 1627-1632 (2017).

123. G. Vampa, T. Hammond, N. Thiré, B. Schmidt, F. Légaré, C. McDonald, T. Brabec, D. Klug and P. Corkum, "All-optical reconstruction of crystal band structure," Physical Review Letters **115**(19), 193603 (2015).

124. R. Silva, I. V. Blinov, A. N. Rubtsov, O. Smirnova and M. Ivanov, "High-harmonic spectroscopy of ultrafast many-body dynamics in strongly correlated systems," Nature Photonics **12**(5), 266-270 (2018).

125. I. Pupeza, D. Sánchez, J. Zhang, N. Lilienfein, M. Seidel, N. Karpowicz, T. Paasch-Colberg, I. Znakovskaya, M. Pescher and W. Schweinberger, "High-power sub-two-cycle mid-infrared pulses at 100 MHz repetition rate," Nature Photonics **9**(11), 721-724 (2015).

126. B.-H. Chen, T. Nagy and P. Baum, "Efficient middle-infrared generation in LiGaS$_2$ by simultaneous spectral broadening and difference-frequency generation," Optics Letters **43**(8), 1742-1745 (2018).

127. H. Timmers, A. Kowligy, A. Lind, F. C. Cruz, N. Nader, M. Silfies, G. Ycas, T. K. Allison, P. G. Schunemann and S. B. Papp, "Molecular fingerprinting with bright, broadband infrared frequency combs," Optica **5**(6), 727-732 (2018).

128. O. Novák, P. R. Krogen, T. Kroh, T. Mocek, F. X. Kärtner and K.-H. Hong, "Femtosecond 8.5 µm source based on intrapulse difference-frequency generation of 2.1 µm pulses," Optics Letters **43**(6), 1335-1338 (2018).

129. C. Gaida, M. Gebhardt, T. Heuermann, F. Stutzki, C. Jauregui, J. Antonio-Lopez, A. Schülzgen, R. Amezcua-Correa, A. Tünnermann and I. Pupeza, "Watt-scale super-octave mid-infrared intrapulse difference frequency generation," Light: Science & Applications **7**(1), 1-8 (2018).

130. Q. Wang, J. Zhang, A. Kessel, N. Nagl, V. Pervak, O. Pronin and K. F. Mak, "Broadband mid-infrared coverage (2–17 µm) with few-cycle pulses via cascaded parametric processes," Optics Letters **44**(10), 2566-2569 (2019).

131. S. Vasilyev, I. S. Moskalev, V. O. Smolski, J. M. Peppers, M. Mirov, A. V. Muraviev, K. Zawilski, P. G. Schunemann, S. B. Mirov and K. L. Vodopyanov, "Super-octave longwave mid-infrared coherent transients produced by optical rectification of few-cycle 2.5-µm pulses," Optica **6**(1), 111-114 (2019).

132. K. Liu, H. Liang, W. Li, X. Zou, S. Qu, T. Lang, Y. Zhang and Q. J. Wang, "Microjoule Sub-Two-Cycle Mid-Infrared Intrapulse-DFG Driven by 3-µ m OPCPA," IEEE Photonics Technology Letters **31**(21), 1741-1744 (2019).

133. Sutherland, Richard L. Handbook of nonlinear optics. CRC press, 2003.

134. K. L. Vodopyanov, "Optical THz-wave generation with periodically-inverted GaAs," Laser & Photonics Reviews **2**(1-2), 11-25 (2008).

135. W. Li, Y. Li, Y. Xu, J. Lu, P. Wang, J. Du and Y. Leng, "Measurements of nonlinear refraction in the mid-infrared materials ZnGeP$_2$ and AgGaS$_2$," Applied Physics B **123**(3), 82 (2017).

136. S. Marzenell, R. Beigang and R. Wallenstein, "Synchronously pumped femtosecond optical parametric oscillator based on AgGaSe$_2$ tunable from 2 µm to 8 µm," Applied Physics B **69**(5-6), 423-428 (1999).

137. M. Mero, L. Wang, W. Chen, N. Ye, G. Zhang, V. Petrov, and Z. Heiner, "Laser-induced damage of nonlinear crystals in ultrafast, high-repetition-rate, mid-infrared optical parametric amplifiers pumped at 1 µm," In Pacific Rim Laser Damage 2019: Optical Materials for High-Power Lasers (Vol. 11063, p. 1106307). International Society for Optics and Photonics.

138. Zhang, Jing-Yuan. Optical parametric generation and amplification. Routledge, 2019.

139. A. Hildenbrand, C. Kieleck, A. Tyazhev, G. Marchev, G. Stöppler, M. Eichhorn, P. Schunemann and V. Petrov, "Laser damage studies of $CdSiP_2$ and $ZnGeP_2$ nonlinear crystals with nanosecond pulses at 1064 and 2090 nm," In Nonlinear Frequency Generation and Conversion: Materials, Devices, and Applications XIII (Vol. 8964, p. 896417). International Society for Optics and Photonics.

140. Y. Li, F. Liu, Y. Li, L. Chai, Q. Xing, M. Hu and C. Wang, "Experimental study on GaP surface damage threshold induced by a high repetition rate femtosecond laser," Applied Optics **50**(13), 1958-1962 (2011).

141. https://www.ascut-bridge.de/products/nir-ir-non-linear-crystals

142. G. M. Archipovaite, P. Malevich, E. Cormier, T. Lihao, A. Baltuska, and T. Balciunas, "Efficient few-cycle mid-IR pulse generation in the 5-11 µm window driven by an Yb amplifier," Advanced Solid State Lasers (Optical Society of America, 2017), paper AM4A-4.

143. A. Lanin, A. Voronin, E. Stepanov, A. Fedotov and A. Zheltikov, "Multioctave, 3–18 µm sub-two-cycle supercontinua from self-compressing, self-focusing soliton transients in a solid," Optics Letters **40**(6), 974-977 (2015).

144. M. Seidel, X. Xiao, S. A. Hussain, G. Arisholm, A. Hartung, K. T. Zawilski, P. G. Schunemann, F. Habel, M. Trubetskov and V. Pervak, "Multi-watt, multi-octave, mid-infrared femtosecond source," Science advances **4**(4), eaaq1526 (2018).

145. B.-H. Chen, E. Wittmann, Y. Morimoto, P. Baum and E. Riedle, "Octave-spanning single-cycle middle-infrared generation through optical parametric amplification in $LiGaS_2$," Optics Express **27**(15), 21306-21318 (2019).

146. S. Qu, H. Liang, K. Liu, X. Zou, W. Li, Q. J. Wang and Y. Zhang, "9 µm few-cycle optical parametric chirped-pulse amplifier based on $LiGaS_2$," Optics Letters **44**(10), 2422-2425 (2019).

147. M. Beutler, I. Rimke, E. Büttner, P. Farinello, A. Agnesi, V. Badikov, D. Badikov and V. Petrov, "Difference-frequency generation of ultrashort pulses in the mid-IR using Yb-fiber pump systems and $AgGaSe_2$," Optics Express **23**(3), 2730-2736 (2015).

148. T. Morimoto, N. Sono, T. Miyamoto, N. Kida and H. Okamoto, "Generation of a carrier-envelope-phase-stable femtosecond pulse at 10 µm by direct down-conversion from a Ti: sapphire laser pulse," Applied Physics Express **10**(12), 122701 (2017).

149. K. Liu, H. Liang, S. Qu, W. Li, X. Zou, Y. Zhang and Q. J. Wang, "High-energy mid-infrared intrapulse difference-frequency generation with 5.3% conversion efficiency driven at 3 µm," Optics Express **27**(26), 37706-37713 (2019).

150. T. Lang, A. Harth, J. Matyschok, T. Binhammer, M. Schultze and U. Morgner, "Impact of temporal, spatial and cascaded effects on the pulse formation in ultra-broadband parametric amplifiers," Optics Express **21**(1), 949-959 (2013).

151. F. Silva, D. Austin, A. Thai, M. Baudisch, M. Hemmer, D. Faccio, A. Couairon and J. Biegert, "Multi-octave supercontinuum generation from mid-infrared filamentation in a bulk crystal," Nature Communications **3**(1), 1-5 (2012).

152. H. Liang, P. Krogen, R. Grynko, O. Novak, C.-L. Chang, G. J. Stein, D. Weerawarne, B. Shim, F. X. Kärtner and K.-H. Hong, "Three-octave-spanning supercontinuum generation and sub-two-cycle self-compression of mid-infrared filaments in dielectrics," Optics letters **40**(6), 1069-1072 (2015).

153. N. Garejev, G. Tamošauskas and A. Dubietis, "Comparative study of multioctave supercontinuum generation in fused silica, YAG, and LiF in the range of anomalous group velocity dispersion," JOSA B **34**(1), 88-94 (2017).

154. A. Marcinkevičiūtė, V. Jukna, R. Šuminas, N. Garejev, G. Tamošauskas and A. Dubietis, "Supercontinuum generation in the absence and in the presence of color centers in NaCl and KBr," Results in Physics **14**(102396 (2019).

155. A. Marcinkevičiūtė, G. Tamošauskas and A. Dubietis, "Supercontinuum generation in mixed thallous halides KRS-5 and KRS-6," Optical Materials **78**(339-344 (2018).

156. O. Mouawad, P. Béjot, F. Billard, P. Mathey, B. Kibler, F. Désévédavy, G. Gadret, J.-C. Jules, O. Faucher and F. Smektala, "Filament-induced visible-to-mid-IR supercontinuum in a ZnSe crystal: Towards multi-octave supercontinuum absorption spectroscopy," Optical Materials **60**(355-358 (2016).

157. A. Lanin, A. Voronin, E. Stepanov, A. Fedotov and A. Zheltikov, "Multioctave, 3–18 μm sub-two-cycle supercontinua from self-compressing, self-focusing soliton transients in a solid," Optics Letters **40**(6), 974-977 (2015).

158. M. Liao, W. Gao, T. Cheng, X. Xue, Z. Duan, D. Deng, H. Kawashima, T. Suzuki and Y. Ohishi, "Five-octave-spanning supercontinuum generation in fluoride glass," Applied Physics Express **6**(3), 032503 (2013).

159. M. Liao, W. Gao, T. Cheng, Z. Duan, X. Xue, H. Kawashima, T. Suzuki and Y. Ohishi, "Ultrabroad supercontinuum generation through filamentation in tellurite glass," Laser Physics Letters **10**(3), 036002 (2013).

160. P. Béjot, F. Billard, C. Peureux, T. Diard, J. Picot-Clémente, C. Strutynski, P. Mathey, O. Mouawad, O. Faucher and K. Nagasaka, "Filamentation-induced spectral broadening and pulse shortening of infrared pulses in Tellurite glass," Optics Communications **380**(245-249 (2016).

161. O. Mouawad, P. Béjot, F. Billard, P. Mathey, B. Kibler, F. Désévédavy, G. Gadret, J.-C. Jules, O. Faucher and F. Smektala, "Mid-infrared filamentation-induced supercontinuum in As–S and an As-free Ge–S counterpart chalcogenide glasses," Applied Physics B **121**(4), 433-438 (2015).

162. S. Frolov, V. Trunov, V. Leshchenko and E. Pestryakov, "Multi-octave supercontinuum generation with IR radiation filamentation in transparent solid-state media," Applied Physics B **122**(5), 124 (2016).

163. T. D. Krauss and F. W. Wise, "Femtosecond measurement of nonlinear absorption and refraction in CdS, ZnSe, and ZnS," Applied physics letters **65**(14), 1739-1741 (1994).

164. K. Liu, H. Liang, L. Wang, S. Qu, T. Lang, H. Li, Q. J. Wang and Y. Zhang, "Multimicrojoule GaSe-based midinfrared optical parametric amplifier with an ultrabroad idler spectrum covering 4.2–16 μm," Optics Letters **44**(4), 1003-1006 (2019).

165. D. Sanchez, M. Hemmer, M. Baudisch, S. Cousin, K. Zawilski, P. Schunemann, O. Chalus, C. Simon-Boisson and J. Biegert, "7 μm, ultrafast, sub-millijoule-level mid-infrared optical parametric chirped pulse amplifier pumped at 2 μm," Optica **3**(2), 147-150 (2016).

166. D. Sánchez, M. Hemmer, M. Baudisch, K. Zawilski, P. Schunemann, H. Hoogland, R. Holzwarth and J. Biegert, "Broadband mid-IR frequency comb with CdSiP 2 and AgGaS 2 from an Er, Tm: Ho fiber laser," Optics Letters **39**(24), 6883-6886 (2014).

167. Z.-S. Feng, Z.-H. Kang, F.-G. Wu, J.-Y. Gao, Y. Jiang, H.-Z. Zhang, Y. M. Andreev, G. V. Lanskii, V. V. Atuchin and T. A. Gavrilova, "SHG in doped GaSe: In crystals," Optics Express **16**(13), 9978-9985 (2008).

168. R. Huber, A. Brodschelm, F. Tauser and A. Leitenstorfer, "Generation and field-resolved detection of femtosecond electromagnetic pulses tunable up to 41 THz," Applied Physics Letters **76**(22), 3191-3193 (2000).